Review

Not peer-reviewed version

Observational Constraints on Dynamical Dark Energy Models

Olga Avsajanishvili [*] , Gennady Y. Chitov , Tina Kahniashvili , Sayan Mandal , Lado Samushia

Posted Date: 27 October 2023

doi: 10.20944/preprints202310.1818.v1

Keywords: Dark energy; observational data; dynamical dark energy models

Article

Observational Constraints on Dynamical Dark Energy Models

Olga Avsajanishvili [1,2], Gennady Y. Chitov [3,4], Tina Kahniashvili [5,2,1], Sayan Mandal [5,2], and Lado Samushia [6,1,2]*

1 E.Kharadze Georgian National Astrophysical Observatory, 47/57 Kostava St.,Tbilisi 0179, Georgia; olga.avsajaniashvili@iliauni.edu.ge
2 School of Natural Sciences and Medicine, Ilia State University, 3/5 Cholokashvili Ave., Tbilisi 0162, Georgia
3 Bogoliubov Laboratory of Theoretical Physics, Joint Institute for Nuclear Research, Dubna 141980, Russia; gennady.chitov@usherbrooke.ca
4 Département de physique, Université de Sherbrooke, Sherbrooke, Québec, J1K 2R1, Canada
5 McWilliams Center for Cosmology and Department of Physics, Carnegie Mellon University, 5000 Forbes Ave, Pittsburgh, PA 15213, USA; tinatin@andrew.cmu.edu
6 Department of Physics, Kansas State University, 116 Cardwell Hall, Manhattan, KS 66506, USA; lado.samushia.office@gmail.com
* Correspondence: olga.avsajaniashvili@iliauni.edu.ge

Abstract: ϕCDM models provide an alternative to the standard ΛCDM paradigm, while being physically better motivated. These models lead to a time-dependent speed of sound for dark energy that is difficult to replicate by wCDM parametrizations. We review the most up-to-date status of observational evidence for the ϕCDM models in this paper. We start with an overview of the motivation behind these classes of models, the basic mathematical formalism, and the different classes of models. We then present a compilation of recent results of applying different observational probes to constraining ϕCDM model parameters. Over the last twenty years, the precision of observational data has increased immensely, leading to ever tighter constraints. A combination of the recent measurements favors the spatially flat ΛCDM model, but a large class of ϕCDM models is still not ruled out.

Keywords: dark energy; observational data; dynamical dark energy models

1. Introduction

The accelerated expansion of our universe was first discovered in 1998 on the basis of measurements of the type Ia supernovae (SNe Ia) apparent magnitudes [1–3]. This fact was later confirmed by other cosmological observations, in particular, by measurements of the temperature anisotropy and the polarization in the cosmic microwave background (CMB) radiation [4–13], by studies of the large-scale structure (LSS) of the universe [14–19], by measurements of baryon acoustic oscillations (BAO) peak length scale [20–26], and by measurements of Hubble parameter [27–35].

One possible explanation for this empirical fact is that the energy density of the universe is dominated by *dark energy* or *dark fluid*, an energy component with an effective negative pressure (see Refs. [36–43] for reviews). The presence of *dark matter* in the universe, first discovered through the anomalously high rotation velocity of the outer regions of galaxies [44], is another major mystery of modern cosmology. Different models for dark matter have been proposed including *cold dark matter* (CDM), consisting of heavy particles with mass $m_{\rm CDM} \geq 100$ KeV, *warm dark matter* (WDM), composing of particles with a mass of $m_{\rm WDM} \approx 3 - 30$ KeV, and *hot dark matter* (HTM) consisting of ultrarelativistic particles [45]. Assuming general relativity is the correct description of gravity on cosmological scales, about 95% of the energy in the universe has to be in the "dark" form, i.e., in the form of dark energy and dark matter, to explain available observations. According to the last Planck data release (PR4), our universe consists of 4.86% of ordinary matter, 25.95% of dark matter, and 70.39% of dark energy [46].

Preprints (www.preprints.org) | NOT PEER-REVIEWED | Posted: 27 October 2023 doi:10.20944/preprints202310.1818.v1

The true nature and origin of dark energy and dark matter are still unresolved issues of modern cosmology. The simplest description of dark energy is the vacuum energy or the cosmological constant Λ (see Refs. [36,39,47] for reviews). The cosmological model based on such a description of dark energy in the spatially flat universe is called the Lambda Cold Dark Matter (ΛCDM) model, which established itself as the *standard* or *concordance* model of the universe in the last two decades (see Ref. [36] for a pioneering work and Refs. [48] for recent review and discussion). In this model, dark matter is presented in the form of non-relativistic *cold* weakly interacting particles which either never been in the equilibrium with the primordial plasma or decoupled from it after becoming non-relativistic at an early stage. A good pedagogical overview of the ΛCDM model is available in many recent books [49–53], and reviews [54–59].

Despite explaining various observations of our universe to a remarkable degree of accuracy, the ΛCDM model has several unsolved problems and tensions [58,60–65], including *the fine-tuning or cosmological constant problem*, *the coincidence problem*, *the Hubble and S_8 tensions*, and *the problem of the shape of the universe*. A large number of cosmological models that go beyond the standard ΛCDM scenario with modified dynamics of the expansion of the universe at late times have been considered in order to resolve these tensions, for a review [66–75].

The value of the energy density of cosmological constant ρ_Λ following from the quantum field theory estimates, is [61] $\rho_\Lambda \sim \hbar M_{\rm pl}^4 \sim 10^{72}$ Gev^4 $\sim 2 \cdot 10^{110}$ erg/cm^3, where $M_{\rm pl} \sim 10^{18}$ Gev is a Planck mass scale, $\hbar$ is a reduced Planck constant. While cosmological observations of the cosmological constant (like dark energy) show a very different result [61] $\rho_\Lambda^{\rm obs} \sim 10^{-48}$ Gev^4 $\sim 2 \cdot 10^{-10}$ erg/cm^3. This discrepancy in 120 orders of magnitude between the predicted and observed values of the energy scale of the cosmological constant is called the cosmological constant problem or the fine turning problem [54,55,57].

The coincidence or why now problem is that, based on precise cosmological observations [76], the energy density in dark energy (68.7%) is comparable (within an order of magnitude) to that of nonrelativistic matter (31.3%) at the present time. This fact is an enigma, because in the ΛCDM model, the energy density of the cosmological constant does not depend on time, $\rho_\Lambda = $ const, while the energy density of matter varies over time as $\rho_{\rm DM} \sim a^{-3}(t)$ ($a(t)$ and t are the scale factor and cosmic time, respectively), so the ratio of these quantities is time-dependent, $\rho_{\rm DM}/\rho_\Lambda \propto a^{-3}(t)$.

The Hubble tension problem is that there is a discrepancy between the value of the Hubble parameter at present epoch $H_0 = 100h$ km c^{-1} Mpc^{-1}, with h is a dimensionless normalized Hubble constant, obtained by the local measurements and CMB temperature anisotropy data [13,77–82].

The S_8 tension problem is that there is a discrepancy at the 2σ to 3σ confidence level between the primary CMB temperature anisotropy measurements by the Planck satellite [13] in the strength of matter clustering compared to lower redshift measurements such as the weak gravitational lensing and galaxy clustering [66,68,83–85].

This tension is quantified using the weighted amplitude of matter fluctuation parameter $S_8 = \sigma_8(\Omega_{\rm m}/0.3)^{0.5}$, which modulates the amplitude of weak lensing measurements, here σ_8 is an amplitude of mass fluctuations on scales of $8h^{-1}$ Mpc; $\Omega_{\rm m} = \Omega_{\rm m0}a^{-3}/E^2(a)$ is a fractional matter density parameter; $E(a) = H(a)/H_0$ is a normalized Hubble parameter; $H(a) = \dot{a}/a$ is a Hubble parameter, $\dot{a}$ is a derivative of the scale factor a with respect to cosmic time.

The problem with the shape of the universe is that the CMB anisotropies power spectra measured by the Planck space telescope show a preference for a spatially-closed universe at more than 3σ confidence level [13,86]. This fact contradicts expectations from the inflation theory [64,66,87], and is interpreted by the cosmological community as a possible crisis of modern cosmology [87–89].

The main alternative to the ΛCDM model, during the period of time when the accelerated expansion of the universe is governed by the cosmological constant Λ, are dynamical dark energy scalar field ϕCDM models [90–98]. In these models, dark energy is described through the equation of state (EoS) parameter, $w_\phi(t)$, which depends on time: $w_\phi(t) \equiv p_\text{Œ}/\rho_\text{Œ}$, $p_\text{Œ}$ - a scalar field pressure, $\rho_\text{Œ}$ - a scalar field energy density; whereas in the ΛCDM model, the EoS parameter is a constant, $w_\Lambda = -1$.

Preprints (www.preprints.org) | NOT PEER-REVIEWED | Posted: 27 October 2023 doi:10.20944/preprints202310.1818.v1

At the same time, at the present epoch, the value of the time-dependent EoS parameter in scalar field models becomes approximately equal to minus one $w_\phi \approx -1$, thus dynamical dark energy mimics the cosmological constant and becomes almost indistinguishable from it.

Depending on the value of the EoS parameter at the present epoch, ϕCDM scalar field models are divided into: quintessence models, with $-1 < w_\phi(t) < -1/3$ [99–101], (see e.g., Refs. [36,43] [for a review) and phantom models, with $w_\phi(t) < -1$ Refs. [102–108]. Quintessence models are divided into two classes: tracker (freezing) models, in which the scalar field evolves slower than the Hubble expansion rate, and thawing models, in which the scalar field evolves faster than the Hubble expansion rate [100,105,109–111]. In quintessence tracker models, the energy density of the scalar field first tracks the radiation energy density and then the matter energy density, while it remains subdominant [112]. Only recently does the scalar field become dominant and begins to behave as a component with the negative pressure, which leads to the accelerated expansion of the universe [101,113,114]. For certain forms of potentials, the quintessence tracker models have an attractor solution that is insensitive to initial conditions [112].

In the standard ΛCDM cosmological scenario, one assumes the existence of two epochs of accelerated expansion in the universe. The first, i.e., inflation [115–123], which happens in the very early universe, and the second is the dark energy dominated epoch observed today, [50,51,124,125]. Inflation is a theory of the exponential expansion of space in the early universe, which is believed to have lasted approximately from 10^{-36} to 10^{-33}-10^{-32} seconds after the Big Bang, the exact times being dependent on the microphysics of the model describing inflation. The inflationary models explain the origin of tiny primordial density fluctuations in the universe, which must have been present at very early epochs, as the seeds for structure formation in the later evolution of the universe. The exponential expansion during inflation comes to an end when a phase transition transforms the vacuum energy into radiation and matter, after which the radiation dominated epoch begins. This phase transition is called *the reheating*, and its governing dynamics is still debated. A successful inflationary model requires a smooth transition to the decelerated epoch (in which inflation rules the universe as if it were dominated by non-relativistic matter) because otherwise, the homogeneity of the universe would be violated [126,127]. Inflation resolves several problems in cosmology, namely, the *horizon problem*, associated with the lack of causal relationship between different regions in the early universe before recombination epoch (it's an epoch of forming the electrically neutral hydrogen atoms, which began at $t_{\rm rec} \approx 350000$ years after the Big Bang), and the *flatness problem*, related to the fine-tuning of the spatial flatness of the universe in the early epoch so that the spatial flatness of the universe is preserved at present epoch.) The evolution of the universe from the inflationary epoch to the present dark energy epoch are investigated in quintessential inflation models too [128–133]. In these models, a single scalar field plays a role of both the inflaton field at the inflationary epoch, and of the quintessence scalar field at the present epoch, thereby the origin of dark energy at the present epoch is also explained within the same model.

The interaction between dark energy and dark matter, namely their transformation into each other, is considered in the interacting dark energy (IDE) models [134–138]. In these models, the coincidence problem of the standard ΛCDM model as well as the Hubble constant H_0 tension can be alleviated [67,70,73,139–141].

In this review, we considered the most significant studies devoted to the observational constraints on dynamical dark energy models over the past twenty years, in particular, scalar field ϕCDM models, quintessential inflation scalar field ϕCDM models, IDE models both in the spatially flat and non-flat hypersurfaces. It can be seen from this review that the complication, refinement of cosmological data, and the increase in the variety of methods for studying dynamical dark energy models lead to more accurate constraints on the values of cosmological parameters in these models. Despite the refinement of various observational data and the complication of methods for studying dark energy in the universe, current observational data still favor the standard spatially flat ΛCDM model, while not excluding dynamical dark energy models and spatially-closed hyperspaces [142–156]. At the same

Preprints (www.preprints.org) | NOT PEER-REVIEWED | Posted: 27 October 2023 doi:10.20944/preprints202310.1818.v1

time, recent studies showed that the currently available observational datasets favor the IDE model at more than 2σ confidence level [67,139,139,140,157,158].

This paper is organized as follows: the different cosmological dynamical dark energy models are described in Section 2, observational constraints on dynamical dark energy models by various observational data are considered in Section 3, conclusions and discussions are presented in Section 4. In this paper, we used the natural system of units: $c = \hbar = k_B = 1$.

2. Cosmological Dark Energy Models

2.1. ΛCDM Model

As highlighted in the Introduction, the Lambda Cold Dark Matter (ΛCDM) model is the *standard* or *concordance* model of a spatially flat universe. In this model, dark energy is represented by the cosmological constant Λ, which is assumed to be associated with the vacuum energy density of quantum fields, and its energy density is a constant

$$\rho_\Lambda = \frac{\Lambda M_{\rm pl}^2}{8\pi} = \rho_{\rm vac} = \text{const}, \tag{1}$$

here $\Lambda = 4.33 \cdot 10^{-66}$ eV^2. The pressure and the energy density in the ΛCDM model are related as

$$p_\Lambda = -\rho_\Lambda = \text{const}, \tag{2}$$

leading to the constant EoS parameter

$$w_\Lambda = -1. \tag{3}$$

The action describing the cosmological constant Λ is [43]

$$S = -\frac{M_{\rm pl}^2}{16\pi}\int d^4x\sqrt{-g}(R + 2\Lambda) + S_{\rm M}, \tag{4}$$

where $g \equiv \det(g_{\mu\nu})$ is the determinant of the metric tensor $g_{\mu\nu}$, R is the Ricci scalar, and $S_{\rm M}$ is the action describing matter. The spatially flat ΛCDM model is typically characterized by six *independent parameters* [159]: the physical baryon density parameter, $\Omega_{\rm b}h^2$; the dark matter physical density parameter, $\Omega_{\rm c}h^2$; the age of the universe, t_0; the scalar spectral index, $n_{\rm s}$; the amplitude of the curvature fluctuations, $\Delta_{\rm R}^2$; and the optical depth during the reionization period for $z \in (6, 20)$, τ. In addition to these parameters, the ΛCDM model is described by six extended *fixed parameters*: the total density parameter, $\Omega_{\rm tot}$; the EoS parameter, w_Λ; the total mass of three types of neutrinos, $\sum m_\nu$; the effective number of the relativistic degrees of freedom, $N_{\rm eff}$; the tensor/scalar ratio, r; the scalar spectral index running, a_s.

The extension of the spatially flat ΛCDM model to spatially non-flat hypersurfaces is the oCDM model. The first Friedmann equations describing the evolution of the universe for the spatially non-flat oCDM model and for the spatially flat ΛCDM model are defined, respectively, as

$$E(a) = (\Omega_{\rm r0}a^{-4} + \Omega_{\rm m0}a^{-3} + \Omega_{\rm k0}a^{-2} + \Omega_\Lambda)^{1/2}, \tag{5}$$

,

$$E(a) = (\Omega_{\rm r0}a^{-4} + \Omega_{\rm m0}a^{-3} + \Omega_\Lambda)^{1/2}, \tag{6}$$

here $\Omega_{\rm r0} = \rho_{\rm r0}/\rho_{\rm cr}$, $\Omega_{\rm m0} = \rho_{\rm m0}/\rho_{\rm cr}$, $\Omega_\Lambda = \rho_\Lambda/\rho_{\rm cr}$ are density parameters at present epoch for radiation, matter and vacuum, respectively, with $\rho_{\rm r0}$ and $\rho_{\rm m0}$ are energy densities for radiation and matter at present epoch, respectively. The value of the critical energy density at present epoch is equal to $\rho_{\rm cr} = 3M_{\rm pl}^2H_0^2/8\pi = 1.8791h^2 \cdot 10^{-29}$ g cm^{-3}; $\Omega_{\rm k0} = -{\rm k}/H_0^2$ is a spatial curvature density

Preprints (www.preprints.org) | NOT PEER-REVIEWED | Posted: 27 October 2023 doi:10.20944/preprints202310.1818.v1

parameter at present epoch, $\rho_{k0} = -3kM_{pl}^2/8\pi$ is a spatial curvature density, k is a curvature parameter, and $E(a) \equiv H(a)/H_0$ is a normalized Hubble parameter.

Observational constraints on cosmological parameters Ω_{m0} and Ω_Λ, obtained from different cosmological datasets for the ΛCDM model and for the oCDM model, are represented in Figure 1.

As we mentioned above, the ΛCDM model is the fiducial model against which all alternative models are compared regarding their fit to observational data. Its predictions agree with the observational data pertaining to the accelerated expansion of the universe, the statistical distribution of LSS, the CMB temperature and polarization anisotropies, and the abundance of light elements in the universe [76,160].

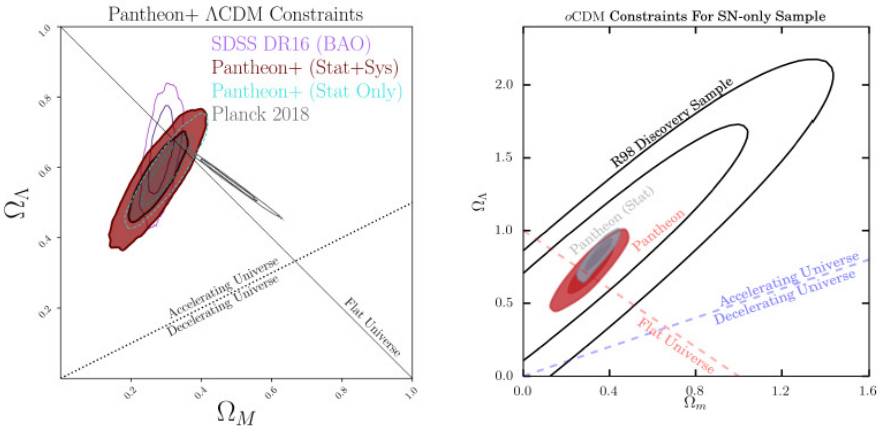

Figure 1. $1\sigma, 2\sigma$ confidence level contours constraints on Ω_m and Ω_Λ parameters (**Left** panel) In the standard spatially flat ΛCDM model from the SNe Ia Pantheon dataset, as well as from combined the from BAO peak length scale and Planck datasets. (The figure is adapted from [161]). (**Right** panel) In the spatially non-flat $o\Lambda$CDM model using discovery sample of Riess et al. [162] and the full Pantheon sample of Scolnic et al. [163]. Pantheon constraints with systematic uncertainties are presented in red, while only statistical uncertainties are denoted in grey. (The figure is adapted from [163]).

2.2. Dynamical Dark Energy Scalar Field ϕCDM Models

There are numerous physically motivated alternative models for the ΛCDM model [43,56,164–174]. One of the prominent alternatives to the ΛCDM model are dynamical scalar field ϕCDM models [36,91,92]. In these models, the role of dark energy is played by a slowly varying uniform self-interacting scalar field ϕ, minimally interacting with gravity. These ϕCDM models involving a dynamical scalar field do not suffer from the fine tuning problem of the ΛCDM model, and have a more natural explanation for the observed low-energy scale of dark energy. In addition, the EoS parameter time dependent in the ϕCDM model, as opposed to it being a constant $w = -1$ in the ΛCDM model. When the energy density of the scalar field begins to dominate over the energy density of both radiation and matter, the universe begins the stage of the accelerated expansion. At early times during the evolution of the universe, the behavior of the dynamical scalar field is different from that of the cosmological constant Λ, but is almost indistinguishable from that of the cosmological constant during later times.

Dynamical scalar field ϕCDM models are divided into two classes: the *quintessence models* [112] and *phantom models* [102,175]. These two classes of models differ from each other by the following attributes:

- **(i)** *The EoS parameter* – For quintessence fields, $-1 < w_\phi < -1/3$, while for phantom fields, $w_\phi < -1$.
- **(ii)** *The sign of the kinetic term* – For quintessence fields, the kinetic term in the Lagrangian has a positive sign, while it is negative for phantom fields.

Preprints (www.preprints.org) | NOT PEER-REVIEWED | Posted: 27 October 2023 doi:10.20944/preprints202310.1818.v1

(iii) *The dynamics of the scalar field* – The quintessence field rolls gradually to the minimum of its potential, while the phantom field rolls to the maximum of its potential.

(iv) *Temporal evolution of dark energy* – For quintessence fields, the dark energy density remains almost unchanging with time, while it increases for phantom fields.

(v) *Forecasting the future of the universe* – The quintessence models predict either an eternal expansion of the universe, or a repeated collapse, depending on the spatial curvature of the universe. On the other hand, the phantom models predict the destruction of any gravitationally-related structures in the universe. Depending on the asymptotic behavior of the Hubble parameter $H(t)$, the future scenarios of the universe are divided into: a *big rip* for which $H(t) \to \infty$ for a finite future time $t = \text{const}$; a *little rip* for which $H(t) \to \infty$ at an infinite future time $t \to \infty$, and a *pseudo rip* for which $H(t) \to \text{const}$ for an infinite future time $t \to \infty$.

The action describing a scalar field in the presence of matter is given by

$$S = \int d^4x \sqrt{-g}\Big(- \frac{M_{\rm pl}^2}{16\pi} R + \mathcal{L}_\phi \Big) + S_{\rm M}, \tag{7}$$

where $\mathcal{L}_\phi$ is the Lagrangian density of the scalar field, the form of which depends on the type of the chosen model, and as mentioned above, R is the Ricci scalar, and $S_{\rm M}$ is the action describing matter. We describe the form of $\mathcal{L}_\phi$ for the quintessence and the phantom fields below.

2.2.1. Quintessence Scalar Field

The dynamics of the quintessence scalar field is described by the Lagrangian density

$$\mathcal{L}_\phi = \frac{1}{2} g^{\mu\nu} \partial_\mu \phi \, \partial_\nu \phi - V(\phi), \tag{8}$$

where $V(\phi)$ is a scalar field potential. There are various quintessence potentials discussed in the literature, but there are currently no observational constraint to prefer one of these over the others. A list of some of the quintessence potentials are presented in Table 1.

Preprints (www.preprints.org) | NOT PEER-REVIEWED | Posted: 27 October 2023 doi:10.20944/preprints202310.1818.v1

Table 1. Scalar field quintessence potentials.

Name	Form	Reference
Ratra-Peebles	$V(\phi) \propto \phi^{-\alpha}$; ($\alpha = \text{const} > 0$)	Ratra & Peebles [91]
Exponential	$V(\phi) \propto \exp(-\lambda\phi/M_{\rm pl})$; ($\lambda = \text{const} > 0$)	Wetterich [92], Ratra & Peebles [90], Lucchin & Matarrese [122], Ferreira & Joyce [176]
Zlatev-Wang-Steinhardt	$V(\phi) \propto (\exp(M_{\rm pl}/\phi) - 1)$	Zlatev et al. [112]
Sugra	$V(\phi) \propto \phi^{-\chi} \exp(\gamma\phi^2/M_{\rm pl}^2)$; ($\chi, \gamma = \text{const} > 0$)	Brax & Martin [177]
Sahni-Wang	$V(\phi) \propto (\cosh(\varsigma\phi) - 1)^{g}$; ($\varsigma = \text{const} > 0$, $g = \text{const} < 1/2$)	Sahni & Wang [178]
Barreiro-Copeland-Nunes	$V(\phi) \propto (\exp(\nu\phi) + \exp(\upsilon\phi))$; ($\nu, \upsilon = \text{const} \geq 0$)	Barreiro et al. [179]
Albrecht-Skordis	$V(\phi) \propto ((\phi - B)^2 + A)\exp(-\mu\phi)$; ($A, B = \text{const} \geq 0$, $\mu = \text{const} > 0$)	Albrecht & Skordis [180]
Urẽna-López-Matos	$V(\phi) \propto \sinh^{m}(\xi M_{\rm pl}\phi)$; ($\xi = \text{const} > 0$, $m = \text{const} < 0$)	Urena-Lopez & Matos [181]
Inverse exponent potential	$V(\phi) \propto \exp(M_{\rm pl}/\phi)$	Caldwell & Linder [100]
Chang-Scherrer	$V(\phi) \propto (\exp(-\tau\phi) + 1)$; ($\tau = \text{const} > 0$)	Chang & Scherrer (2016) [182]

The EoS parameter for the quintessence scalar field is given by

$$w_\phi \equiv \frac{p_\phi}{\rho_\phi} = \frac{\dot{\phi}^2/2 - V(\phi)}{\dot{\phi}^2/2 + V(\phi)}, \tag{9}$$

where $p_\phi = \frac{1}{2}\dot{\phi}^2 - V(\phi)$ and $\rho_\phi = \frac{1}{2}\dot{\phi}^2 + V(\phi)$ are respectively the pressure and energy density of the quintessence field. Here, overdots denoting derivatives with respect to the cosmic time t. The equation of motion for the quintessence scalar field can be obtained by varying the action in Equation (7), along with the Lagrangian in Equation (8),

$$\ddot{\phi} + 3H\dot{\phi} + V'(\phi) = 0, \tag{10}$$

with the prime denoting a derivative with respect to the scalar field ϕ. The first Friedmann's equation for a ϕCDM model in a spatially non-flat spacetime has the form

$$E(a) = (\Omega_{\rm r0}a^{-4} + \Omega_{\rm m0}a^{-3} + \Omega_{\rm k0}a^{-2} + \Omega_{\mathfrak{Q}}(a))^{1/2}, \tag{11}$$

where $\Omega_{\mathfrak{Q}}(a)$ is the dark energy (scalar field) density parameter.

Depending on the shape of potentials, quintessence models are further subdivided into *thawing models* and *freezing (tracking) models* [43,100]

a) In the thawing models, the scalar field is too suppressed by the retarding effect of the Hubble expansion, represented by the term $3H\dot{\phi}$ in Equation (10), until recently. This results in a much slower evolution of the scalar field compared to the Hubble expansion, and the thawing scalar field manifests itself as the vacuum energy, with the EoS parameter $w_\phi \sim -1$. The Hubble

Preprints (www.preprints.org) | NOT PEER-REVIEWED | Posted: 27 October 2023 doi:10.20944/preprints202310.1818.v1

expansion rate $H(t)$ decreases with time, and after it falls below $\sqrt{V''(\phi)}$, the scalar field begins to roll to the minimum of its potential. The value of the EoS parameter for the scalar field thus increases over time and becomes $w_\phi > -1$.

b) In the freezing models, the scalar field is always suppressed (it is damped), i.e., $H(t) > \sqrt{V''(\phi)}$. Freezing scalar field models have so-called tracking solutions. According to tracking solutions, the quintessence component tracks the background EoS parameter (radiation in the radiation-dominated epoch and matter in the matter-dominated epoch) and eventually only recently grows to dominate the energy density in the universe. This leads to the accelerated expansion of the universe at late times, since the scalar field has a negative effective pressure. The tracker behavior allows the quintessence model to be insensitive to initial conditions. But this requires fine tuning of the potential energy, since $\sqrt{V''(\phi)} \sim H_0 \sim 10^{-33}$ eV.

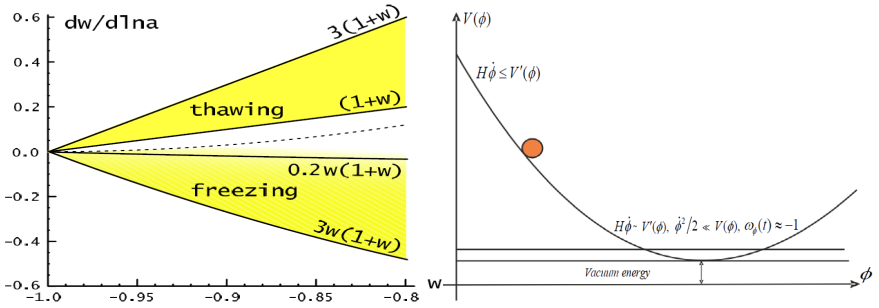

Figure 2. (**Left** panel) The location of thawing and freezing scalar fields in the $w_\phi - dw_\phi/d\ln a$ plane. (The figure is adapted from [100]). (**Right** panel) Regimes of the quick rolling down and slow rolling down of the freezing scalar field to the minimum of its potential.

In 1988, Ratra and Peebles introduced a tracker ϕCDM model comprising of a scalar field with an inverse power-law potential of the form $V(\phi) = \kappa/2M_{\rm pl}^2\phi^{-\alpha}$, for a model parameter $\alpha > 0$ [90,91]. For $\alpha = 0$, this ϕCDM Ratra-Peebles (RP) model reduces to the ΛCDM model. The positive parameter κ relates to the mass scale of the particles, M_ϕ, as $M_\phi \sim (\kappa M_{\rm pl}^2/2)^{\frac{1}{\alpha+4}}$. The RP ϕCDM model is a typical representative of the behavior of tracker quintessence scalar field ϕCDM models.

2.2.2. Phantom Scalar Field

The Lagrangian density describing a phantom scalar field has the form

$$\mathcal{L}_\phi = -\frac{1}{2}g^{\mu\nu}\partial_\mu\phi\partial_\nu\phi - V(\phi), \tag{12}$$

where the negative sign of the kinetic energy term is required to ensure the dark energy EoS parameter is less than -1, i.e., $w_\phi < -1$, and the energy density increases over time [107]. The incomplete list of phantom potentials is given in Table 2.

Preprints (www.preprints.org) | NOT PEER-REVIEWED | Posted: 27 October 2023 doi:10.20944/preprints202310.1818.v1

Table 2. Scalar field phantom potentials.

Name	Form	Reference
Fifth power	$V(\phi) \propto \phi^5$	Scherrer & Sen [104]
Inverse square power	$V(\phi) \propto \phi^{-2}$	Scherrer & Sen [104]
Exponent	$V(\phi) \propto \exp(\beta\phi)$; $(\beta = \text{const} > 0)$	Scherrer & Sen [104]
Quadratic	$V(\phi) \propto \phi^2$	Dutta & Scherrer [105]
Gaussian	$V(\phi) \propto (1 - \exp(\phi^2/\sigma^2))$; $(\sigma = \text{const})$	Dutta & Scherrer [105]
Pseudo-Nambu-Goldstone boson (pNGb)	$V(\phi) \propto (1 - \cos(\phi/\kappa))$; $(\kappa = \text{const} > 0)$	Frieman et al. [183]
Inverse hyperbolic cosine	$V(\phi) \propto \cosh^{-1}(\psi\phi)$; $(\psi = \text{const} > 0)$	Dutta & Scherrer [105]

Analogous to Equation (9), the EoS parameter for the phantom scalar field is given by

$$w_\phi \equiv \frac{p_\phi}{\rho_\phi} = \frac{-\dot{\phi}^2/2 - V(\phi)}{-\dot{\phi}^2/2 + V(\phi)}, \tag{13}$$

where $p_\phi = -\frac{1}{2}\dot{\phi}^2 - V(\phi)$ and $\rho_\phi = -\frac{1}{2}\dot{\phi}^2 + V(\phi)$ are respectively the pressure and energy density of the phantom field. The equation of motion for the phantom scalar field has the form

$$\ddot{\phi} + 3H\dot{\phi} - V'(\phi) = 0. \tag{14}$$

2.3. Parameterized Dark Energy Models

2.3.1. wCDM Parameterization

In dynamical dark energy models, one can use the wCDM parameterization where the EoS parameter can be expressed as $p = w(a)\rho$. Dark energy models are sometimes characterized only by the EoS parameter, and corresponding cosmological models are called wCDM models [184]. This parameterization has no physical motivation, but is commonly used as an ansatz in data analysis to quantify different and distinguish between dark energy models. The wCDM parameterization in particular makes it possible to differentiate, at present epoch, the ΛCDM model from other dark energy models.

The time-dependent EoS parameter in wCDM models is often characterized by the Chevallier-Polarsky-Linder (CPL) $w_0 - w_a$ parameterization [185,186]

$$w(a) = w_0 + w_a(1 - a), \tag{15}$$

where $w_0 = w(a_0)$ and $w_a = (dw/dz)|_{z=1} = -a^{-2}(dw/da)|_{a=1/2}$, with z being the cosmological redshift defined as $z = 1/a - 1$, and a_0 is the scale factor at present time, conventionally normalized as $a_0 = 1$. Although the CPL parameterization is simple and flexible enough to accurately describe EoS parameters in most dark energy models, it cannot describe arbitrary dark energy models with good accuracy (up to a few percent) over a wide redshift range [186]. The dynamical dark energy models where the EoS parameter is expressed through the CPL parameterization are called the w_0w_aCDM models.

The normalized Hubble parameter for w_0w_aCDM model for the spatially flat universe has the form

$$E(a) = \left[\Omega_{r0}a^{-4} + \Omega_{m0}a^{-3} + (1 - \Omega_{m0})a^{-3(1+w_0+w_a)}e^{-3w_a(1-a)}\right]^{1/2}. \tag{16}$$

Preprints (www.preprints.org) | NOT PEER-REVIEWED | Posted: 27 October 2023 doi:10.20944/preprints202310.1818.v1

1σ, 2σ confidence level contours constraints on cosmological parameters w_0 and w_a in the w_0w_aCDM model from different combinations of datasets: SNe Ia apparent magnitude (including measurenments of the Hubble Space Telescope (HST)), CMB temperature anisotropy, BAO peak length scale are presented in Figure 3 (**Left** panel).

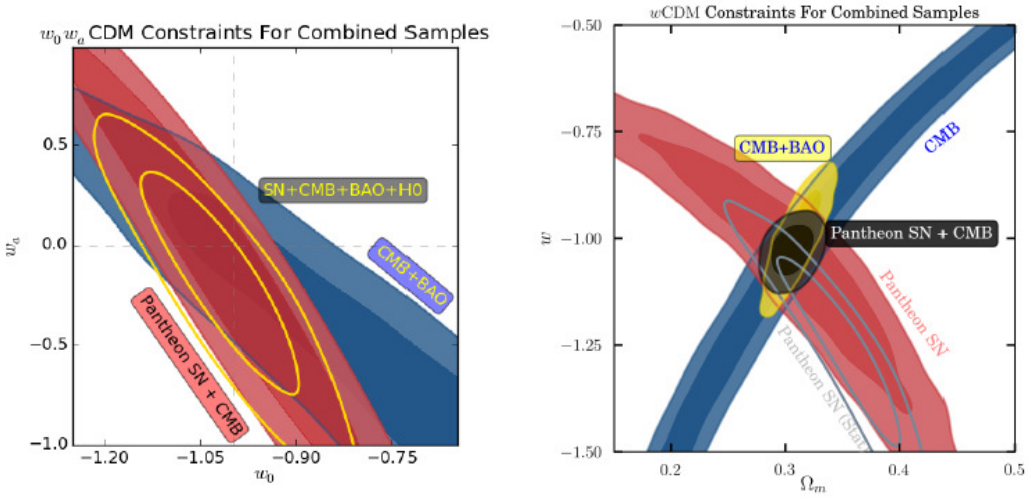

Figure 3. (**Left** panel) 1σ, 2σ confidence level contours constraints on cosmological parameters w_0 and w_a in the wCDM model from various datasets: SNe Ia apparent magnitude+CMB temperature anisotropy+BAO peak length scale+HST (yellow), BAO peak length scale+CMB temperature anisotropy (blue), SNe Ia apparent magnitude+CMB temperature anisotropy (red). (**Right** panel) 1σ, 2σ confidence level contours constraints on cosmological parameters $\Omega_{\rm m}$ and w in the wCDM model from various datasets: SNe Ia apparent magnitude+CMB temperature anisotropy (black), CMB temperature anisotropy (blue), SNe Ia apparent magnitude (red) (with systematic uncertainties), SNe Ia apparent magnitude (gray line) (with only statistical uncertainties). The figure is adapted from [163].

2.3.2. XCDM Models

Cosmological dark energy models with a constant value of the EoS parameter are called XCDM models. These models are defined both in the spatially flat and spatially non-flat hyperspaces. The normalized Hubble parameter expressed through the dark energy EoS parameter w_X has the form

$$E(a) = \left[\Omega_{\rm r0}a^{-4} + \Omega_{\rm m0}a^{-3} + \Omega_{\rm k0}a^{-2} + (1-\Omega_{\rm m0})a^{-3(1+w_X)}\right]^{1/2}. \quad (17)$$

The case $w_X = -1$ is equivalent to the standard spatially flat ΛCDM model with the same matter energy density parameter $\Omega_{\rm m0}$ and zero spatial curvature, $\Omega_{\rm k0} = 0$, at present epoch.

1σ, 2σ confidence level contours constraints on cosmological parameters w_X in the XCDM model from different combinations of datasets: SNe Ia apparent magnitude, CMB temperature anisotropy, BAO peak length scale are presented in Figure 3 (**Right** panel).

2.4. Quintessential Inflation Models

The action for quintessential inflation models has the general form

$$S = \int d^4x\sqrt{-g}\Big(-\frac{M_{\rm pl}^2}{16\pi}R + \frac{1}{2}g^{\mu\nu}\partial_\mu\phi\partial_\nu\phi - V(\phi)\Big) + S_{\rm M} + S_{\rm R} + S_{\rm I}(g_{\mu\nu},\phi,\psi,\chi,B_\mu), \quad (18)$$

where $S_{\rm R}$ is the action describing radiation, $S_{\rm I}$ is the action describing the interactions of the inflaton field with the fermion (ψ), scalar (χ), vector (B_μ) degrees of freedom in the Standard Model and beyond.

To maintain inflation over a long period of time, it is necessary that the acceleration caused by the inflaton field be sufficiently small compared to its velocity over the Hubble time. Under these

Preprints (www.preprints.org) | NOT PEER-REVIEWED | Posted: 27 October 2023 doi:10.20944/preprints202310.1818.v1

conditions, the first Friedmann's and Klein-Gordon's equations for the inflaton field in the spatially flat universe take the form [122,187,188]

$$\rho = \dot{\phi}^2/2 + V(\phi) \xrightarrow{\dot{\phi}^2/2 \ll V(\phi)} \rho = \frac{3M_{\rm Pl}^2}{8\pi} H^2 \simeq V(\phi), \qquad \ddot{\phi} + 3H\dot{\phi} + V'(\phi) = 0 \xrightarrow{|\ddot{\phi}| \ll 3H|\dot{\phi}|} -V'(\phi) \simeq 3H\dot{\phi}. \tag{19}$$

The slow-roll regime of the inflaton field is provided by potential of the inflaton field $V(\phi)$ with certain shapes: exponential [131], power-law [128,129], and plateau-like [132,133]. The slow-roll parameters, which determine the curvature and slope of the potential of the inflaton field, should remain small for some period of time to sustain the inflationary behavior

$$\epsilon = \frac{M_{\rm pl}^2}{2}\left(\frac{V'(\phi)}{V(\phi)}\right)^2 \ll 1, \quad \eta = M_{\rm pl}^2 \frac{V''(\phi)}{V(\phi)} \ll 1, \quad \xi = M_{\rm pl}^2 \frac{V'(\phi)V'''(\phi)}{V(\phi)^2} \ll 1. \tag{20}$$

The condition $\epsilon \ll 1$ is necessary for the accelerated expansion of the universe to take place, while the condition $\epsilon \simeq 1$ defines the end of inflation. In the case of $\epsilon \approx 0$, the expansion rate of the universe is approximately constant, i.e., the scale factor grows exponentially with time, $a \propto e^{Ht}$, resulting in an almost de Sitter expansion of the universe.

The scalar spectral index (n_s), tensor spectral index (n_t), scalar spectral index running (a_s), and tensor-to-scalar ratio (r) are defined, respectively, as [131]

$$n_s - 1 = -6\epsilon + 2\eta, \quad n_t = -2\epsilon, \quad a_s \equiv {\rm d}n_s/{\rm d}\ln k = 16\epsilon\eta - 24\epsilon^2 - 2\xi, \quad r = 16\epsilon. \tag{21}$$

During the inflationary epoch of the universe, scalar and tensor perturbations are created from quantum vacuum fluctuations and are spatially stretched to superhorizon scales, where they become classical, and the almost scale-invariant tilted primordial power spectrum is formed [189]. The tilted primordial scalar $\mathcal{P}_s(k)$ and tensor $\mathcal{P}_t(k)$ power spectra for spatially flat tilted quintessential inflation models are defined in terms of the wave number k as [122,187,188]

$$\mathcal{P}_s(k) = A_s\left(\frac{k}{k_0}\right)^{n_s-1}, \quad \mathcal{P}_t(k) = A_t\left(\frac{k}{k_0}\right)^{n_t}, \tag{22}$$

where A_s and A_t are the curvature perturbations amplitude and tensor amplitude at the pivot scale $k_0 = 0.05\,{\rm Mpc}^{-1}$ [51].

The untilted primordial power spectrum for untilted spatially non-flat quintessential inflation models is defined as [130,190]

$$P(q) \propto \frac{(q^2 - 4K)^2}{q(q^2 - K)}, \tag{23}$$

here $q = \sqrt{k^2 + K}$ is the wavenumber for scalar perturbations. In the spatially flat limit $K = 0$, $P(q)$ reduces to the $n_s = 1$ spectrum.

2.5. Interacting Dark Energy Models

As mentioned above, one of the major unresolved problems of modern cosmology is the so called coincidence problem in the ΛCDM model, in which the energy densities of dark energy and dark matter are of the same order of magnitude at the present epoch. One way to resolve this problem is to assume that these components somehow interact with each other. IDE models consider the transformation of dark energy and dark matter into each other, with their interaction between described by the following modified continuity equations for dark energy and matter, respectively

$$\dot{\rho}_{\rm m} + 3H\rho_{\rm m} = \delta_{\rm couple}, \tag{24}$$

$$\dot{\rho}_{\rm CE} + 3H(\rho_{\rm CE} + p_{\rm CE}) = -\delta_{\rm couple}, \tag{25}$$

Preprints (www.preprints.org) | NOT PEER-REVIEWED | Posted: 27 October 2023 doi:10.20944/preprints202310.1818.v1

where $\rho_{\rm m}$ is the matter energy density, $\rho_{\text{Œ}}$ and $p_{\text{Œ}}$ are respectively the energy density and pressure of the scalar field, and $\delta_{\rm couple}$ is the coupling coefficient between dark energy and matter. In IDE models, the following forms of the coupling coefficient $\delta_{\rm couple}$ are typically used [136,137]

$$\delta_{\rm couple} = nQ\rho_{\rm m}\dot{\phi}, \tag{26}$$

$$\delta_{\rm couple} = \beta H(\rho_{\rm m} + \rho_{\text{Œ}}), \tag{27}$$

where $n = \sqrt{8\pi/M_{\rm pl}^2}$, and β and Q are dimensionless constants. The IDE models are subdivided into two types, as described below [88,136,137].

2.5.1. Coupling of the First Type

The IDE models of the first type are characterized by the exponential potential for the scalar ϕ and the linear interaction determined by the coupling coefficient given by Equation (26), as discussed in [136]. The coupled quintessence scalar field equation is given as

$$\ddot{\phi} + 3H\dot{\phi} + V'(\phi) = -nQ\rho_{\rm m}\dot{\phi}, \tag{28}$$

where $V(\phi) = V_0 e^{-n\lambda\phi}$ is the scalar field potential and λ is a model parameter. The coupled continuity equation for dark energy is

$$\dot{\rho}_{\text{Œ}} + 3H(\rho_{\text{Œ}} + p_{\text{Œ}}) = -nQ\rho_{\rm m}\dot{\phi}. \tag{29}$$

The matter energy density evolves according to

$$\dot{\rho}_{\rm m} + 3H\rho_{\rm m} = nQ\rho_{\rm m}, \tag{30}$$

leading to

$$\rho_{\rm m} = \rho_{\rm m0} a^{-3} e^{nQ\phi}. \tag{31}$$

2.5.2. Coupling of the Second Type

For the second type of IDE models, the scalar potential, and hence the dynamics of the interaction between dark energy and matter, is constructed with the requirement that the coincidence parameter $r = \rho_{\rm m}/\rho_\phi$ takes an analytic expression and for $z \to 0$ becomes a constant, thereby alleviating the coincidences problem of the ΛCDM model [88,137].

The equation of motion for ϕ, Equation (25), can be written as

$$\dot{\phi}\left[\ddot{\phi} + 3H\dot{\phi} + V'(\phi)\right] = -\delta_{\rm couple}. \tag{32}$$

The coupling coefficient $\delta_{\rm couple}$ is constrained by the requirement that the solution to Eqs. (25) be compatible with a constant relationship between $\rho_{\rm m}$ and ρ_ϕ energy densities. It is convenient to introduce the quantities $\Pi_{\rm m}$ and Π_ϕ by

$$\delta_{\rm couple} = -3H\Pi_{\rm m} = 3H\Pi_\phi, \tag{33}$$

by introducing these quantities, the continuity equations for dark energy and matter Eqs. (25) will have a form

$$\dot{\rho}_{\rm m} + 3H(\rho_{\rm m} + \Pi_{\rm m}) = 0, \qquad \dot{\rho}_{\text{Œ}} + 3H(\rho_{\text{Œ}} + p_{\text{Œ}} + \Pi_\phi) = 0. \tag{34}$$

The quantities $\Pi_{\rm m}$ and Π_ϕ are interconnected as

$$\Pi_{\rm m} = -\Pi_\phi = \frac{\rho_{\rm m}\rho_\phi}{\rho}(\gamma_\phi - 1), \tag{35}$$

Preprints (www.preprints.org) | NOT PEER-REVIEWED | Posted: 27 October 2023 doi:10.20944/preprints202310.1818.v1

$$\gamma_\phi = \frac{p_{\text{CE}} + \rho_\phi}{\rho_\phi} = \frac{\dot{\phi}^2}{\rho_\phi} \tag{36}$$

where $\rho = \rho_{\text{m}} + \rho_\phi$.
Assuming γ_ϕ is a constant, the value of which $\gamma_\phi \in (0, 2)$, it can be found

$$\rho_{\text{m}} \propto \rho_\phi \propto \rho \propto a^{-\nu}, \quad \text{for } \nu = 3\frac{\gamma_\phi + r}{r+1}, \tag{37}$$

here r is a coincidence parameter, which takes an analytic expression for r, becomes a constant, thereby alleviating the coincidences problem. The solution of the second Friedmann's equation $3M_{\text{pl}}H^2 = 8\pi\rho$, for the result, obtained in Equation (37), has a form $a \propto t^{2/\nu}$. Thus, the Hubble parameter is defined as

$$H = \frac{2}{\nu t} = \frac{2(r+1)}{3(\gamma_\phi + r)}\frac{1}{t}. \tag{38}$$

The energy density parameter is defined as $\Omega_\phi = \frac{8\pi M_{\text{pl}}^2}{3H^2}\rho_\phi$, as well as $\Omega_\phi = \frac{1}{r+1}$. Equating these equations and inserting Equation (38), we will have

$$\rho_\phi = \frac{M_{\text{pl}}^2}{6\pi}\frac{1+r}{(\gamma_\phi + r)^2}\frac{1}{t^2}. \tag{39}$$

The combination with Equation (36) gives

$$\dot{\phi} = \sqrt{\frac{M_{\text{pl}}^2\gamma_\phi(1+r)}{6\pi}}\frac{1}{(\gamma_\phi + r)^2}\frac{1}{t}, \tag{40}$$

thus, the consequence of the condition $\rho_\phi \sim \rho_{\text{m}}$ is the logarithmic evolution of the scalar field ϕ with time.
Applying the equation for the energy density for the scalar field $\rho_\phi = \frac{1}{2}\dot{\phi}^2 + V(\phi)$ and Equation (36), it can be derived

$$\rho_\phi = \frac{2V(\phi)}{2 - \gamma_\phi} = \frac{\dot{\phi}^2}{\gamma_\phi}, \tag{41}$$

which together with Equations (39) and (40) leads to

$$V(\phi) = \frac{M_{\text{pl}}^2}{6\pi}\left(1 - \frac{\gamma_\phi}{2}\right)\frac{1+r}{(\gamma_\phi + r)^2}\frac{1}{t^2} \quad \Rightarrow \quad \frac{\partial V(\phi)}{\partial\phi} = -\lambda V(\phi), \tag{42}$$

where $\lambda = \sqrt{\frac{24\pi}{M_{\text{pl}}^2\gamma_\phi(1+r)}}$. Equation (42) implies that the potential has the exponential form

$$V(\phi) = V_0 e^{-\lambda(\phi - \phi_0)}. \tag{43}$$

A significant drawback of this model is the absence of a convincing explanation for the onset of the interaction of dark energy and matter at the epoch of transition from the decelerated to the accelerated expansion of the universe. The thermal quantum-field theory treatment of the quintessence dark energy coupled to the matter field shows that one can consistently recover different expansion regimes of the universe, including the late-time acceleration, however more work is needed to relate the matter field to a viable dark matter candidate [191,192].

Preprints (www.preprints.org) | NOT PEER-REVIEWED | Posted: 27 October 2023 doi:10.20944/preprints202310.1818.v1

3. Constraints From Observational Data

3.1. Type Ia Supernovae

The observed magnitudes of type Ia supernovas are one of the best data for constraining the distance redshift relationship through the determination of the luminosity distance. In the ϕCDM models, the distances tend to be smaller compared to the ΛCDM predictions at the same redshift. This provides an opportunity for differentiating these models from each other.

One of the first studies in this direction was performed in Podariu and Ratra [193]. They used three datasets of SNe Ia apparent magnitude versus redshift: (i) R98 data [162], both including and excluding the unclassified SN Ia 1997ck at $z = 0.97$ (with 50 and 49 SNe Ia apparent magnitude data, respectively), (ii) P99 data [2], and (iii) a third set with the corrected/effective stretch factor magnitudes for the 54 Fit C SNe Ia of P99 apparent magnitude data, and obtained constraints on the **ϕCDM model** with **RP potential** (**ϕCDM-RP model**) (see Figure 4).

Caresia et al. [194] obtained constraints on parameters of the **ϕCDM** with the **RP** and **Sugra potentials** [177,195], and also the **extended quintessence models** with the inverse power-law **RP potential** [196,197], from datasets of apparent magnitude versus redshift measurements of 176 SNe Ia [2,162,198], and data of the SuperNovae Acceleration Probe (SNAP) satellite [199][1]. Obtained constraints on model parameters are shown in Figures 5 and 6. No useful constraints on the model parameters were found for the Sugra potential, while 1σ constraints of $\alpha < 0.8$ and $\alpha < 0.6$, for both the extended and ordinary quintessence models using the RP potential, were obtained using the SNe Ia apparent magnitude and SNAP satellite data respectively.

---

[1] For the latter model, the first Friedmann's equation and Klein-Gordon scalar field equation for these models are defined, respectively as

$$H^2(a) = \frac{1}{3F}\left(a^2\rho_{\rm fluid} + \frac{1}{2}\dot{\phi}^2 + a^2V(\phi) - 3H(a)\dot{F}(\phi)\right), \tag{44}$$

$$\ddot{\phi} + 2H\dot{\phi} = \frac{a^2}{2}F'(\phi)R - a^2V'(a), \tag{45}$$

where the dot now denotes the derivative with respect to the conformal time, and the prime denotes a derivative with respect to the scalar field ϕ. The quantity $\rho_{\rm fluid}$ is the energy density associated with all components of the universe except for the quintessential scalar field, and the function $F(\phi)$ defines the non-minimal coupling between gravity and the scalar field ϕ, with the form [196]

$$F(\phi) = 1/8\pi G + \tilde{F}(\phi) - \tilde{F}(\phi_0), \tag{46}$$

where $\tilde{F}(\phi) = \xi\phi^2$, ξ is a dimensionless constant, ϕ_0 is a value of the scalar field at the present epoch.

Preprints (www.preprints.org) | NOT PEER-REVIEWED | Posted: 27 October 2023 doi:10.20944/preprints202310.1818.v1

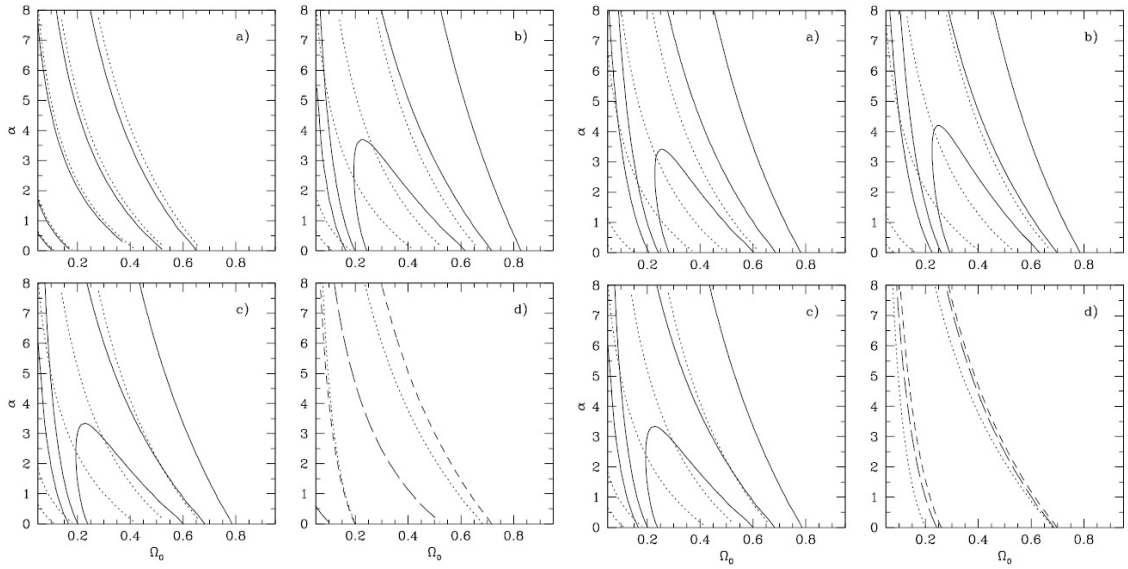

Figure 4. 1σ, 2σ and 3σ confidence level contours constraints on parameters of the scalar field ϕCDM model with the RP potential. (**Left** panel) (**a**) for all R98 SNe Ia apparent magnitude data, (**b**) for R98 SNe Ia apparent magnitude data excluding the $z = 0.97$ measurement, (**c**) for P99 Fit C SNe Ia apparent magnitude dataset, (**d**) for three datasets: all R98 SNe Ia apparent magnitude (long-dashed lines) data, R98 SNe Ia apparent magnitude data excluding the $z = 0.97$ measurement (short-dashed lines), and P99 Fit C SNe Ia apparent magnitude data (dotted lines). (**middle** panel) for P99 Fit C SNe Ia apparent magnitude data in conjunction with: (**a**) H_0 measurements, (**b**) t_0 measurements, (**c**) H_0 and t_0 measurements, (**d**) for P99 Fit C SNe Ia apparent magnitude data in conjunction with: the H_0 constraint (long-dashed lines), the t_0 constraint (short-dashed lines), and both t_0 and H_0 constraints (dotted lines). (**Right** panel) (**a**) for all the R98 SNe Ia apparent magnitude data, (**b**) for R98 SNe Ia apparent magnitude data excluding the $z = 0.97$ measurement, (**c**) for P99 Fit C SNe Ia apparent magnitude data, (**d**) for the H_0 and t_0 constraints used in conjunction with: all R98 SNe Ia (long-dashed lines) apparent magnitude data, R98 SNe Ia apparent magnitude data excluding the $z = 0.97$ measurement (short-dashed lines), and the P99 Fit C SNe Ia apparent magnitude data (dotted lines). The figure is adapted from [193].

Preprints (www.preprints.org) | NOT PEER-REVIEWED | Posted: 27 October 2023 doi:10.20944/preprints202310.1818.v1

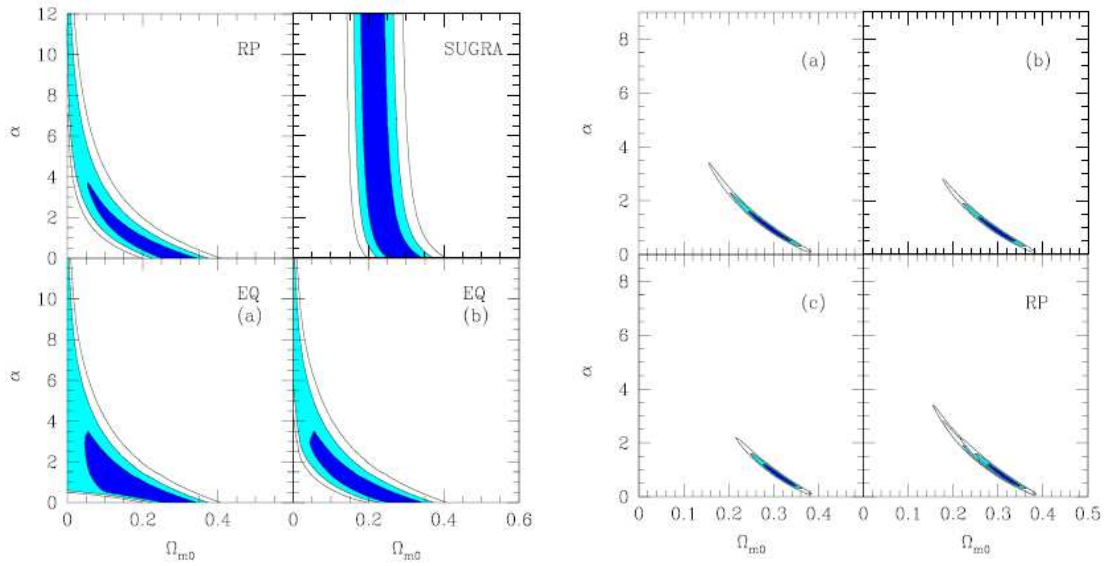

Figure 5. (**Left** panel) 1σ, 2σ and 3σ confidence level contours constraints on Ω_{m0} and α parameters by using a sample of 176 SNe Ia apparent magnitude data. (**Upper left** sub-panel) for the ordinary quintessence with the inverse power-law RP potential, (**upper right** sub-panel) for the ordinary quintessence with the Sugra potential, (lower left sub-panel) for the extended quintessence with the inverse power-law RP potential, (lower right sub-panel) for the extended quintessence with the inverse power-law RP potential when upper limits on the time variation of the gravitational constant are satisfied. (**Right** panel) 1σ, 2σ and 3σ confidence level contours constraints on Ω_{m0} and α parameters for the ordinary ϕCDM quintessence model with the inverse power-law RP potential by using SNAP sample data. (**Upper left** sub-panel) corresponds to constraints obtained by assuming the exact EoS parameter, panel (**upper right** sub-panel) corresponds to the linear approximation of the EoS parameter, (**lower left** sub-panel) corresponds to the constant approximation of the EoS parameter, (**lower right** sub-panel) corresponds to the superposition of above-mentioned three cases. The figure is adapted from [194].

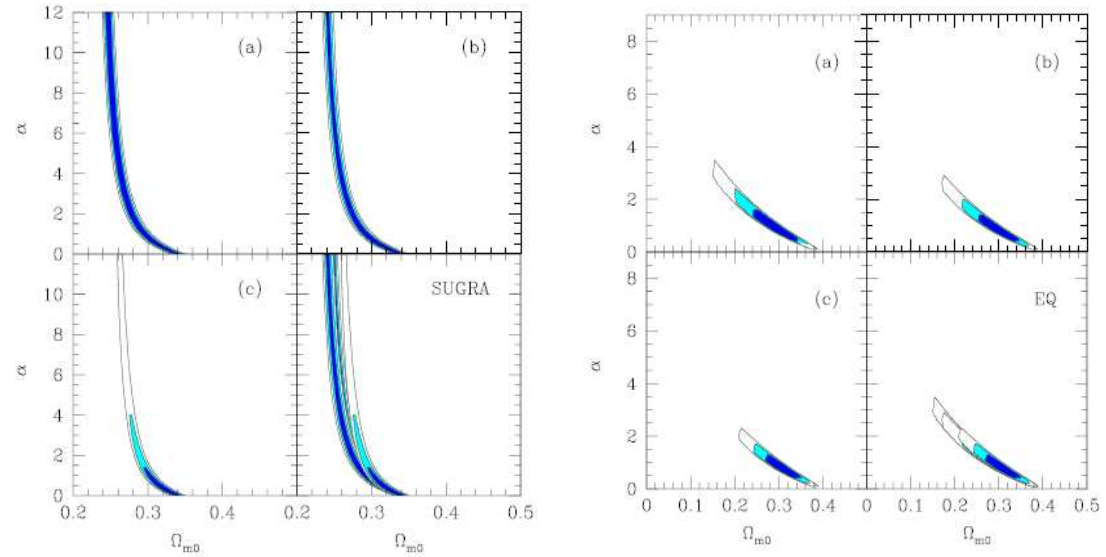

Figure 6. (**Left** panel) As Figure 5, but for the ordinary ϕCDM quintessence model with the Sugra potential. (**Right** panel) As Figure 5, but for the extended quintessence model with the inverse power-law RP potential. The results are obtained by imposing the upper bound on the time variation of the gravitational constant. The figure is adapted from [194].

Preprints (www.preprints.org) | NOT PEER-REVIEWED | Posted: 27 October 2023 doi:10.20944/preprints202310.1818.v1

Doran et al. [200] considered a DE model parameterized as [200]

$$\Omega_\phi(a) = \frac{e^{R(a)}}{1+e^{R(a)}}, \;\; w(a) = w_0 \ln a/(1-b\ln a)^2, \tag{47}$$

where $R(a) = \ln(\Omega_\phi(a)/(1-\Omega_\phi(a))$ corresponds to

$$R(a) = R_0 - \frac{2w_0 \ln a}{1-b\ln a}, \tag{48}$$

the constant b is defined by the EoS parameter at present epoch w_0, the dark energy density parameter at present epoch $\Omega_{\phi 0}$, and the parameter Ω_e characterizing the amount of dark energy at early times to which it asymptotes for very large redshifts, as

$$b = -3w_0\Big(\ln\frac{1-\Omega_e}{\Omega_e} + \ln\frac{1-\Omega_{\phi 0}}{\Omega_{\phi 0}}\Big). \tag{49}$$

Using a combination of datasets from SNe Ia [162], Wilkinson Microwave Anisotropy Probe (WMAP) [201], Cosmic Background Imager (CBI) [202], Very Small Array (VSA) [203], SDSS [204], and HST [205], the authors find $w_0 < -0.8$ and $\Omega_e < 0.03$ at the 1σ confidence level; the contours are shown in Figure 7. It should be noted that the SNe Ia apparent magnitude data are most sensitive to w_0, while CMB temperature anisotropies and LSS growth rate are the best constraints of Ω_e (see Figure 8).

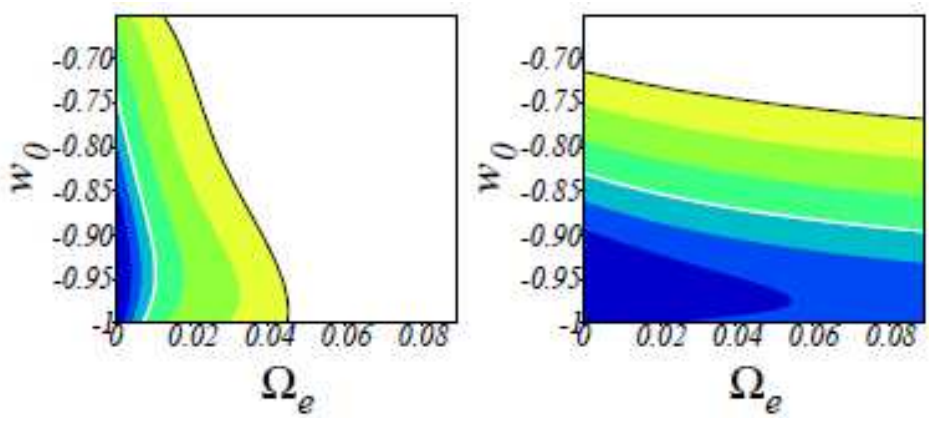

Figure 7. Constraints on parameters Ω_e and w_0. The left picture depicts the distribution from WMAP+CBI+VSA+SDSS+HST data, and the right picture is that of SNe Ia apparent magnitude versus redshift data alone. The regions of 1σ (2σ) confidence level are enclosed by a white (black) line. The figure is adapted from [200].

Preprints (www.preprints.org) | NOT PEER-REVIEWED | Posted: 27 October 2023 doi:10.20944/preprints202310.1818.v1

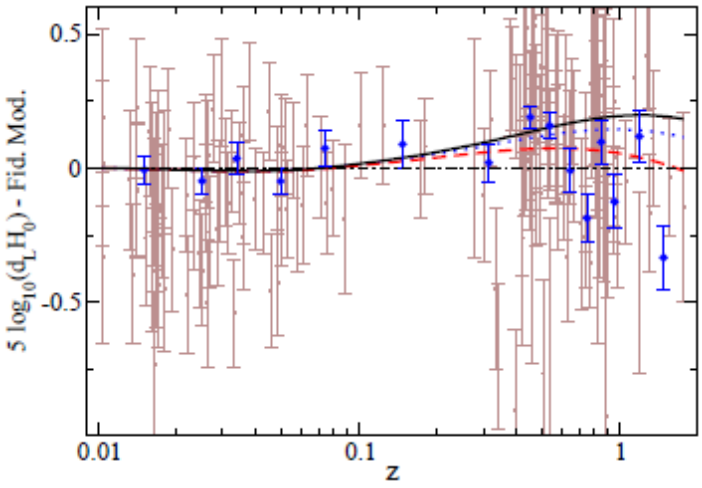

Figure 8. SNe Ia apparent magnitude versus redshift data [162] as data points with thin (brown) error bars. The authors plotted the logarithm of the luminosity distance minus a fiducial model for which $d_L H_0 = (1+z)\ln(1+z)$. The solid (black) line is for the spatially flat ΛCDM model, the dotted (blue) line is for $\Omega_e = 10^{-4}$, and the dashed (red) line is for $\Omega_e = 10^{-1}$. For all models $w_0 = -1$. The figure is adapted from [200].

Fuzfa & Alim [206] studied the **ϕCDM model** with the **RP** and **Sugra potentials** in a **spatially closed** universe. The estimated values of Ω_{m0} and $\Omega_{Œ0}$, using SNe Ia apparent magnitude data from the SNLS collaboration [207], are quite different than those for the standard spatially flat ΛCDM model (Figure 9). Such a result is expected due to the different cosmic acceleration and dark matter clustering predicted between quintessence models and the standard ΛCDM model, arising from differences in cosmological parameters, even at $z = 0$. The quintessence scalar field creates more structures outside the filaments, lighter halos with higher internal velocity dispersion, as seen from N-body simulations performed by the authors to study the influence of quintessence on the distribution of matter on large scales.

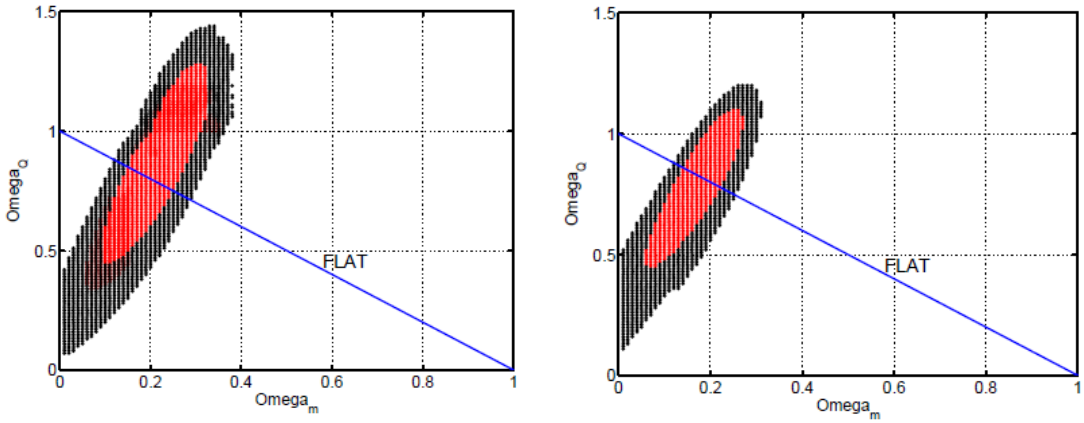

Figure 9. 1σ, 2σ confidence level contours constraints on constraints the matter density parameter at present epoch Ω_{m0} and the dark energy density (quintessence) parameter at present epoch Ω_{Q0} for scalar field ϕCDM models. (**Left** panel) With the inverse power-law PR potential. (**Right** panel) With Sugra potential $V(\phi) \propto \phi^{-\alpha} \exp(4\pi\phi^2)$. The figure is adapted from [206].

Pavlov et al. [208] found that for the **ϕCDM-RP** model in a spacetime with **nonzero spatial curvature**, the dynamical scalar field has an attractor solution in the curvature dominated epoch, while the energy density of the scalar field increases relative to that of the spatial curvature. In the left panel of Figure 10, we see that the values $\Omega_{m0} = 0.27$ and $\alpha = 3$ are consistent with these constraints for a

Preprints (www.preprints.org) | NOT PEER-REVIEWED | Posted: 27 October 2023 doi:10.20944/preprints202310.1818.v1

range of values Ω_{k0}, for a set of values of H_0t_0[2]. The right panel of Figure 10 shows a similar analysis for several values of the cosmological test parameter $\triangle(\Omega_{m0}, \Omega_{k0}, \alpha) = \delta(t_0)/(1+z_i)\delta(t_i)$, where $\delta(t_0)$ and $\delta(t_i)$ are the values of the matter density contrast at respectively at the present time t_0, and an arbitrary time t_i such that $a(t_i) \ll a(t_0)$, i.e., a time when the universe is well approximated by the Einstein-de Sitter model in the matter-dominated epoch.

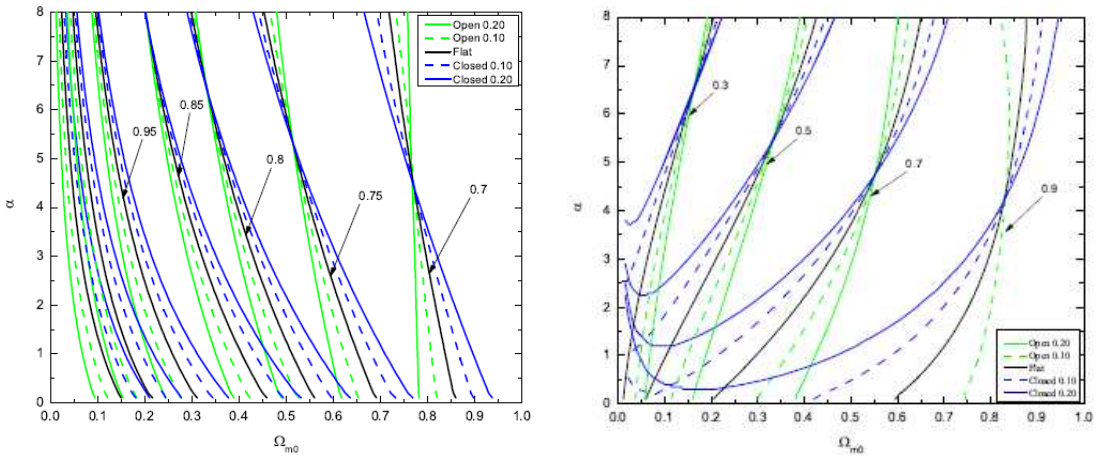

Figure 10. (**Left** panel) 2σ contours of the fixed time parameter H_0t_0 as a function of values of the matter density parameter at present epoch Ω_{m0} and space curvature density parameter at present epoch Ω_{k0}, as well as the model parameter α in the scalar field ϕCDM model with the RP potential. The results obtained for larger values of free parameters $(\Omega_{m0}, \Omega_{k0}, \alpha)$ and for $H_0t_0 = [0.7, 0.75, 0.8, 0.85, 0.95, 1.05, 1.15]$. (**Right** panel) 2σ contours of the factor by which the growth of matter perturbations falls lower than in the Einstein–de Sitter model. The cosmological test parameter values $\triangle(\Omega_{m0}, \Omega_{k0}, \alpha)$ obtained for the larger values of free parameters $(\Omega_{m0}, \Omega_{k0}, \alpha)$. The figure is adapted from [208]

Farooq et al. [209] constrained the **ϕCDM-RP** model in a spacetime with **non-zero spatial curvature**, as well as the **XCDM model**, using the Union2.1 compilation of 580 SNe Ia apparent magnitude measurements of Suzuki et al. [210], Hubble parameter observations [28,30,211,212], and the $0.1 \leq z \leq 0.75$ BAO peak length scale measurements [21,22,213] (see Figure 11). They constrain the spatial curvature density parameter today to be $|\Omega_{k0}| \leq 0.15$ at 1σ confidence level, and more precise data are required to tighten the bounds on the parameters.

[2] Here, t_0 is the current age of the universe, given by

$$t_0 = \int_0^{a_0} \frac{da}{a}. \tag{50}$$

Preprints (www.preprints.org) | NOT PEER-REVIEWED | Posted: 27 October 2023 doi:10.20944/preprints202310.1818.v1

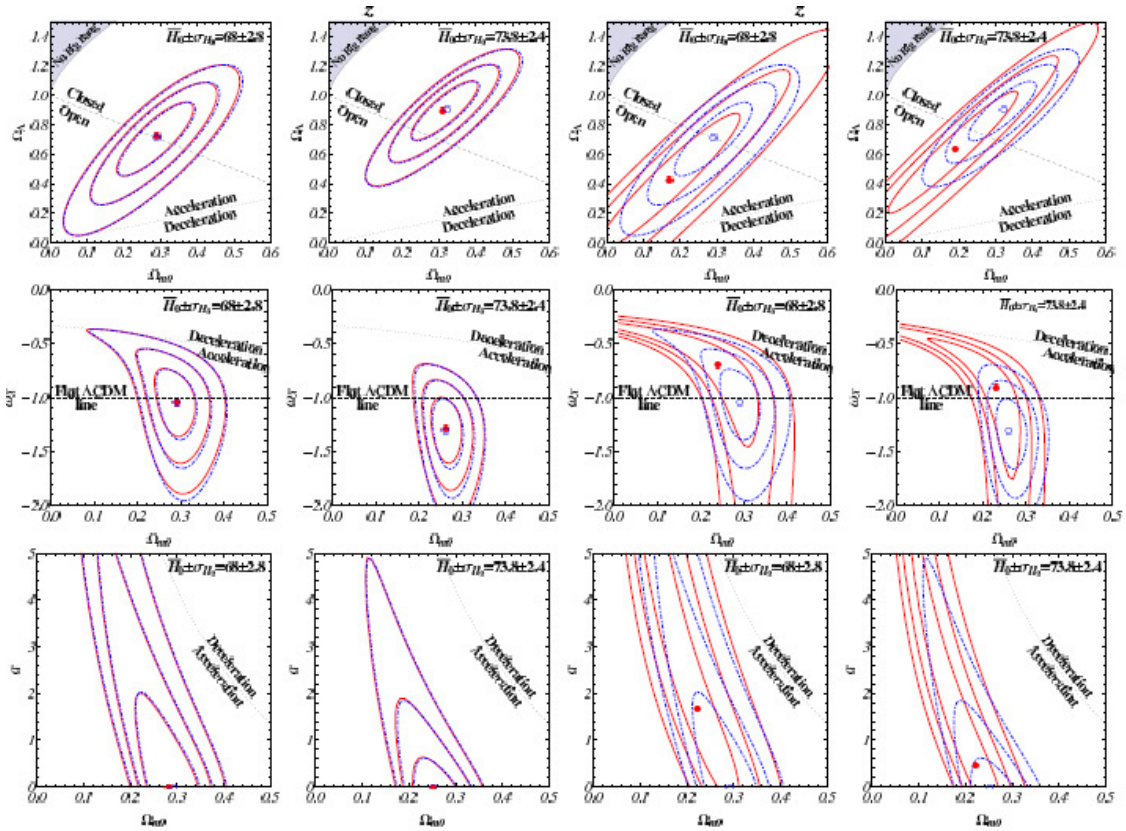

Figure 11. 1σ, 2σ and 3σ confidence level contours constraints on parameters of the spatially non-flat scalar field ϕCDM model with the RP potential from compilations of data: $H(z)$+SNe Ia apparent magnitude (**first** row), $H(z)$+BAO peak length scale (**second** row), and BAO peak length scale+SNe Ia apparent magnitude (**third** row). Filled circles denote best-fit points. The dot-dashed lines in the first column panels are 1σ, 2σ and 3σ confidence level contours obtained by Farooq et al. [214] for the spatially flat ϕCDM model (open circles denote best-fit points). Dotted lines separate the accelerating and decelerating models (at zero space curvature). The horizontal axis with $\alpha = 0$ corresponds to the standard spatially flat ΛCDM model. First, second, and third columns correspond to marginalizing over Ω_{k0}, α, and Ω_{m0}, respectively. The figure is adapted from [209].

Assuming that the Hubble constant H_0 tension of the ΛCDM model is actually a tension on the SNe Ia absolute magnitude M_B, Nunes & Di Valentino [139] assessed the M_B tension by comparing of **spatially flat ΛCDM model**, **wCDM** and **IDE models** using two datasets compilation SNe Ia Pantheon sample [163]+ BAO [22,24,25,215,216] + big bang nucleosynthesis (BBN) [217] and SNe Ia Pantheon sample + BAO [22,24,25,215,216] + BBN [217] + M_B [218] (see Figure 12). They found that the IDE model can alleviate both the M_B and H_0 tensions with a coupling different from zero at 2σ confidence level with a preference for a compilation of Pantheon + BAO + BBN + M_B datasets.

Preprints (www.preprints.org) | NOT PEER-REVIEWED | Posted: 27 October 2023 doi:10.20944/preprints202310.1818.v1

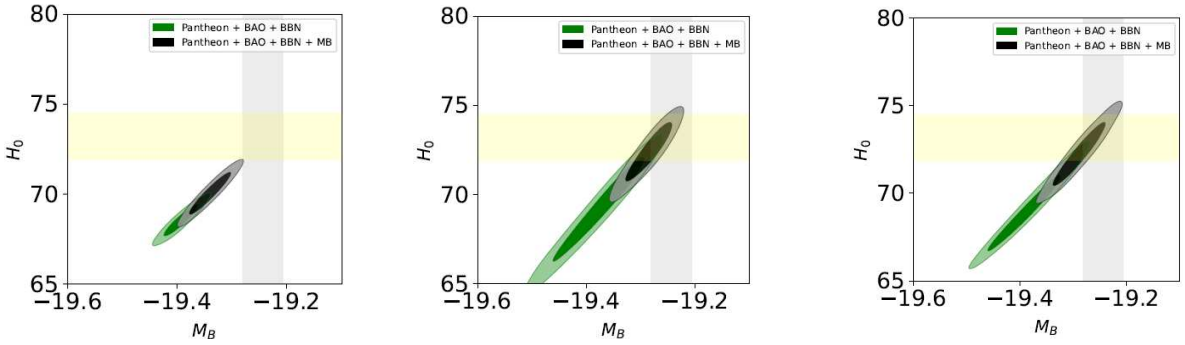

Figure 12. 1σ and 2σ confidence level contours constraints on M_B and H_0 values for ΛCDM (**left** panel), wCDM (**middle** panel) and IDE (**right** panel) models, obtained from compilations Pantheon + BAO + BBN and Pantheon + BAO + BBN + M_B datasets. The figure is adapted from [139].

3.2. Cosmic Microwave Background Radiation Data

The CMB provides a very accurate determination of the angular diameter distance at a redshift of $z \sim 1000$. This measurement is sensitive to the entire expansion of the universe over this wide range of redshifts. As pointed out before, ϕCDM models tend to predict smaller distances and can therefore be constrained with the CMB geometric measurements.

In one of the first such studies, Doran et al. [219] used CMB temperature anisotropy data from the BOOMERANG and MAXIMA experiments [220,221] to distinguish quintessential inflation models with different EoS parameters, described by a kinetic term $k(\phi)$ of the cosmon field[3]: (i) the **RP potential** with $k(\phi) = 1$, (ii) the **leaping kinetic term model** which has $V(\phi) = M_{\bar{\text{pl}}}^4 \exp(-\phi/M_{\bar{\text{pl}}})$, $M_{\bar{\text{pl}}} = \sqrt{8\pi} M_{\text{pl}}$ is the reduced Plank mass, $k(\phi) = k_{\text{min}} + \tanh[(\phi - \phi_1)/M_{\bar{\text{pl}}}] + 1$, $\phi_1 \approx 277$ eV and $k_{\text{min}} = [0.05, 0.1, 0.2, 0.26]$ [222], and (iii) the **exponential potential** with $V(\phi) = M_{\bar{pl}}^4 \exp(-\sqrt{2}\alpha\phi/M_{\bar{\text{pl}}})$, $\alpha = \sqrt{3/2\Omega_{\phi 0}}$, and $k(\phi) = 1$ [134]. The dark energy density parameters today and at last scattering epoch, $\Omega_{\phi 0}$ and Ω_{CEls}, and the averaged EoS parameter of the field ϕ are used to parameterize the separation of peaks in CMB temperature anisotropies, which can be used to measure the value of Ω_ϕ before the last scattering (see Figure 13).

---

[3] This model is described by a Lagrangian of the form $\mathcal{L}_\phi = \frac{1}{2}(\partial_\mu \phi)^2 k^2(\phi) + V(\phi)$.

Preprints (www.preprints.org) | NOT PEER-REVIEWED | Posted: 27 October 2023 doi:10.20944/preprints202310.1818.v1

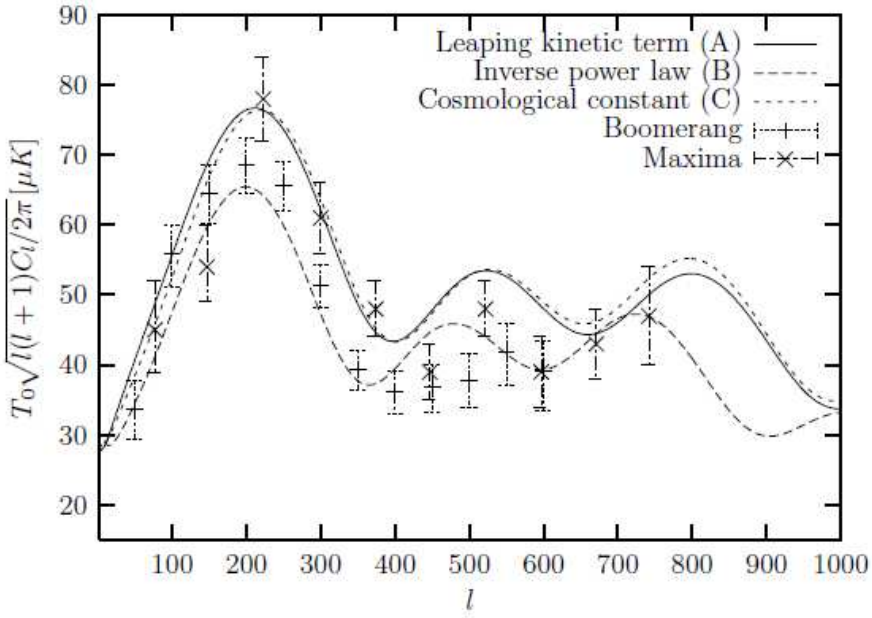

Figure 13. The CMB temperature anisotropy spectrum for different quintessence scalar field ϕCDM models: with the leaping kinetic term (model A), with the inverse power-law RP potential (model B) (here the dark energy density parameter at present epoch $\Omega_{\phi 0} = 0.6$), and for the ΛCDM model (model C). Data points from the BOOMERANG [220] and MAXIMA [221] experiments are shown for reference. The figure is adapted from Ref. [219].

Caldwell et al. [223] investigated how early quintessence dark energy, i.e., a non-negligible quintessence energy density during the recombination and structure formation epochs, affects the baryon-photon fluid and the clustering of dark matter, and thus the CMB temperature anisotropy and the matter power spectra. They showed that early quintessence is characterized by a suppressed ability to cluster at small length scales, as suggested by the compilation of data from WMAP [224,225], CBI [226,227], Arcminute Cosmology Bolometer Array Receiver (ACBAR) [228], the LSS growth rate dataset of Two degree Field (2dF) Galaxy Redshift Survey [229–231], and $L_{y-\alpha}$ forest [232,233]; these are shown in Figure 14. Furthermore, quintessential inflation models are compatible with these data for a constant spectral index of primordial density perturbations, as seen in the left panel of Figure 14.

Pettorino et al. [234] studied a class of **extended ϕCDM models**, where the scalar field is exponentially coupled to the Ricci scalar and is described by the **RP potential**. The projection of the ISW effect on the CMB temperature anisotropy[4] is found to be considerably larger in the exponential case with respect to a quadratic non-minimal coupling as seen in Figure 15. This reflects the fact that the effective gravitational constant depends exponentially on the dynamics of the scalar field.

---

[4] The observational constraints on a projection of the Integrated Sachs-Wolfe (ISW) effect on the CMB temperature anisotropy was obtained for a fixed value of the Jordan-Brans-Dicke (JBD) parameter at present epoch ω_{JBD0}, the latter being defined as

$$\omega_{\rm JBD} = F\left(\frac{dF}{d\phi}\right)^{-2} = \frac{8\pi}{\xi^2}\exp\left[-\frac{\xi(\phi-\phi_0)}{M_{\rm pl}}\right], \quad \omega_{\rm JBD0} = 8\pi/\xi^2, \tag{51}$$

where ξ is a dimensionless coupling, ϕ_0 is the present value for the scalar field, and $F = \frac{1}{16\pi G}\exp\left(\frac{\xi}{M_{\rm pl}}(\phi-\phi_0)\right)$ is a generalized function of the gravity term $R/16\pi G$.

Preprints (www.preprints.org) | NOT PEER-REVIEWED | Posted: 27 October 2023 doi:10.20944/preprints202310.1818.v1

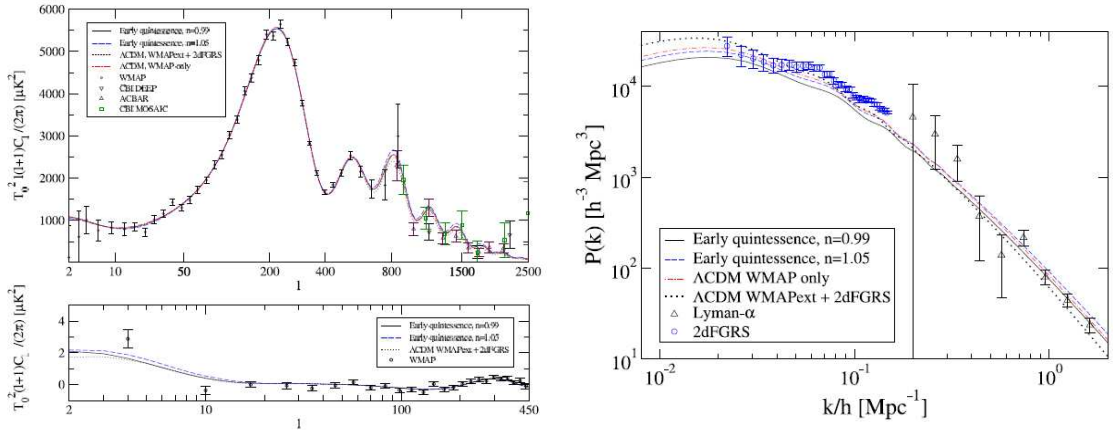

Figure 14. (**Left** panel) Polarization (TE) and Temperature (TT) as a function of the multipole l. Two quintessential inflation models with $n_s = 0.99$ and $n_s = 1.05$ are presented with WMAP data of [224,225]. WMAP-normalized spectra for the best-fit for the ΛCDM model (no $L_{y-\alpha}$ data) with the constant spectral index $n = 0.97$ [201], and the ΛCDM model with the running spectral index $n_s = 0.93$, $dn_s/d\ln k = -0.031$ are shown for comparison. For large l, CBI data and ACBAR data are used. (**Right** panel) The CDM power spectrum at present epoch as a function of k/h. The linear spectrum for two quintessential inflation models with spectral indices $n_s = 0.99$ and $n_s = 1.05$ are plotted. The best-fit for the ΛCDM model with running spectral index $n_s = 0.93$, $dns/d\ln k = -0.031$ [201]), normalized to WMAP data (no $L_{y-\alpha}$ data) are shown. 2dFGRS measurements and $L_{y-\alpha}$ data are converted to $z = 0$. The figure is adapted from [223].

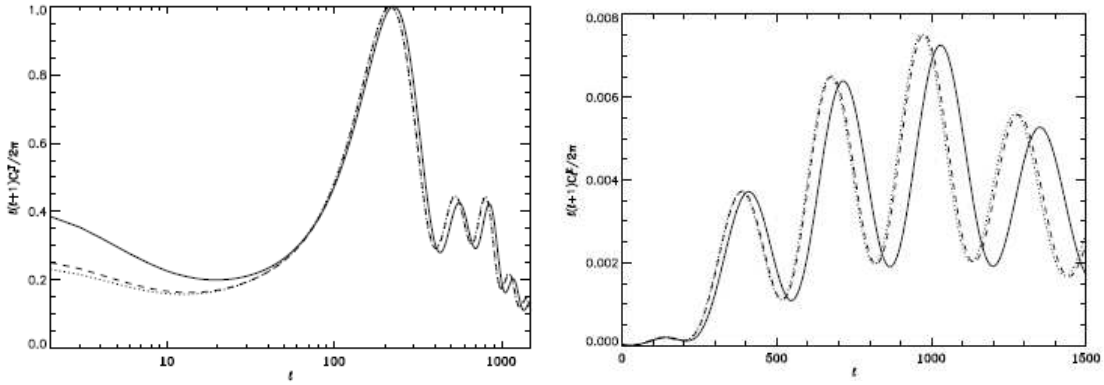

Figure 15. The spectra are in arbitrary units, normalized to unity at the first acoustic peak. (**Left** panel) CMB angular total intensity power spectra for the scalar field ϕCDM model with the inverse power-law RP potential (dotted), quadratic (dashed) and exponential coupling extended quintessence (solid) with $\omega_{\rm JBD0} = 50$. (**Right** panel) CMB angular polarisation power spectra for the ϕCDM model (dotted), quadratic (dashed) and exponential coupling extended quintessence (solid) with $\omega_{\rm JBD0}$. The figure is adapted from [234].

Mukherjee et al. [235] conducted a likelihood analysis of the Cosmic Background Explorer - Differential Microwave Radiometers (COBE-DMR) sky maps to normalize the **ϕCDM-RP model in**

Preprints (www.preprints.org) | NOT PEER-REVIEWED | Posted: 27 October 2023 doi:10.20944/preprints202310.1818.v1

flat space[5]. As seen from Figure 16, this model remains an observationally viable alternative to the standard spatially flat ΛCDM model.

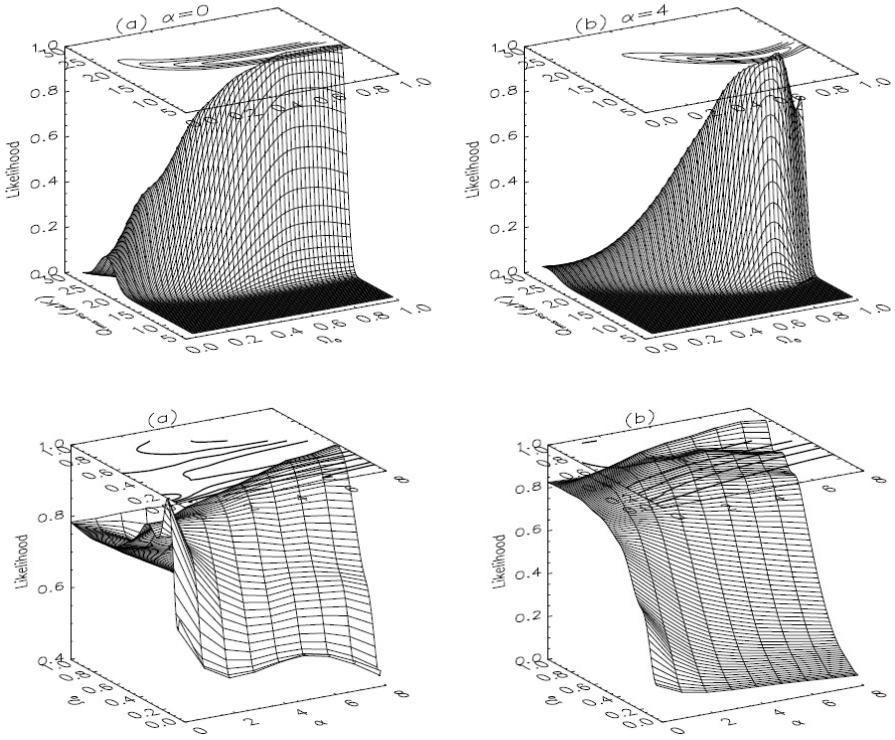

Figure 16. The model with $t_0 = 13$ Gyr and $\Omega_b h^2 = 0.014$. Likelihood functions $L(Q_{rms-PS}, \alpha, \Omega_0)$ (arbitrarily normalized to unity at the highest peak). (**Left** panel) Derived from a simultaneous analysis of DMR 53 and 90 GHz galactic-frame data. The faint high-latitude foreground Galactic emission is corrected, and the quadrupole moment in the analysis is included: a) for $\alpha = 0$ and b) for $\alpha = 4$. (**Right** panel) Derived by marginalizing $L(Q_{rms-PS}, \alpha, \Omega_0)$ over Q_{rms-PS} with an uniform prior: a) the correction for the faint high-latitude foreground Galactic emission is ignored and the quadrupole moment from the analysis is excluded, b) for the faint high latitude foreground Galactic emission is corrected and the quadrupole moment in the analysis is included. The figure is adapted from [235].

Samushia and Ratra [238] constrainted model parameters of the **ΛCDM model**, the **XCDM model**, and the **ϕCDM-RP model** using galaxy cluster gas mass fraction data [239], for this, they introduced an auxiliary random variable as opposed to integrating over nuisance parameters of the Markov Chain Monte Carlo (MCMC) method. Two different sets of priors were chosen to study the influence of the type of priors on the obtained results – one set has [7] $h = 0.73 \pm 0.03$, $\Omega_b h^2 = 0.0223 \pm 0.0008$ (1σ errors), and the other set has $h = 0.68 \pm 0.04$ [240,241], and $\Omega_b h^2 = 0.0205 \pm 0.0018$ [242]. The obtained constraints on the ϕCDM model with the RP potential are shown in Figure 17. We see that Ω_m is better constrained than α, whose best-fit value is $\alpha = 0$, corresponding to the standard spatially flat ΛCDM model, however, the scalar field ϕCDM model is not excluded.

[5] This is done by fixing at present epoch the amplitude of the initial energy density fluctuations generated in the early inflation epoch for this model, and comparing model predictions of the large angular scale spatial anisotropy in the CMB radiation with observational data. The authors computed model predictions as a function of the model parameter α, as well as other cosmological parameters, following Brax et al. [236], and then determined the normalization amplitude by comparing these predictions with COBE-DMR CMB temperature anisotropy measurements of Bennett [5] and Gorski et al. [237]

Preprints (www.preprints.org) | NOT PEER-REVIEWED | Posted: 27 October 2023 doi:10.20944/preprints202310.1818.v1

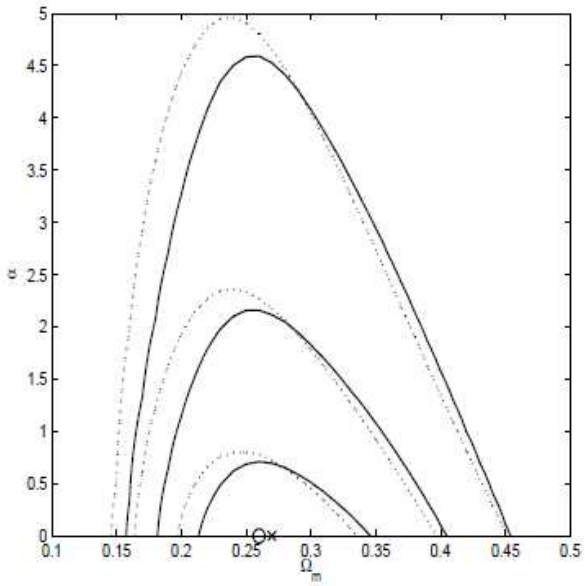

Figure 17. 1σ, 2σ and 3σ confidence level contours constraints on parameters of the scalar field ϕCDM model with the inverse power-law RP potential using cluster gas mass fraction data. Solid lines correspond to WMAP prior while dashed lines correspond to the alternate prior. The cross matches the best-fit at $\Omega_{m0} = 0.27$ and $\alpha = 0$. The circle denotes the best-fit at $\Omega_{m0} = 0.26$ and $\alpha = 0$. The horizontal axis for which $\alpha = 0$ corresponds to the spatially flat ΛCDM model. The figure is adapted from [238].

Chen et al. [243] constrained the scalar field ϕ**CDM-RP model** and the Λ**CDM model** with massive neutrinos assuming two different neutrino mass hierarchies in both the spatially flat and non flat universes, using a joint dataset comprising of CMB temperature anisotropy data [12,244], BAO peak length scale data from 6dF Galaxy Survey (6dFGS), from SDSS - Main Galaxy Sample (MGS), Baryon Oscillation Spectroscopic Survey (BOSS)-LOWZ (galaxies within the redshift range $0.2 < z < 0.43$), BOSS CMASS-DR11 (galaxies within the redshift range $0.43 < z < 0.7$) [23], the joint light-curve analysis (JLA) compilation from SNe Ia apparent magnitude measurements [245], and the Hubble Space Telescope H_0 prior observations [29]. Assuming three species of degenerate massive neutrinos, they found the 2σ upper bounds of $\sum m_\nu < 0.165\ (0.299)$ eV and $\sum m_\nu < 0.164\ (0.301)$ eV respectively for the spatially flat (spatially non-flat) ΛCDM model and the spatially flat (spatially non-flat) ϕCDM model (see Figure 18). The inclusion of spatial curvature as a free parameter leads to a significant expansion of the confidence regions for $\sum m_\nu$ and other parameters in spatially flat ϕCDM models, but the corresponding differences are larger for both the spatially non-flat ΛCDM and spatially non-flat ϕCDM models.

Preprints (www.preprints.org) | NOT PEER-REVIEWED | Posted: 27 October 2023 doi:10.20944/preprints202310.1818.v1

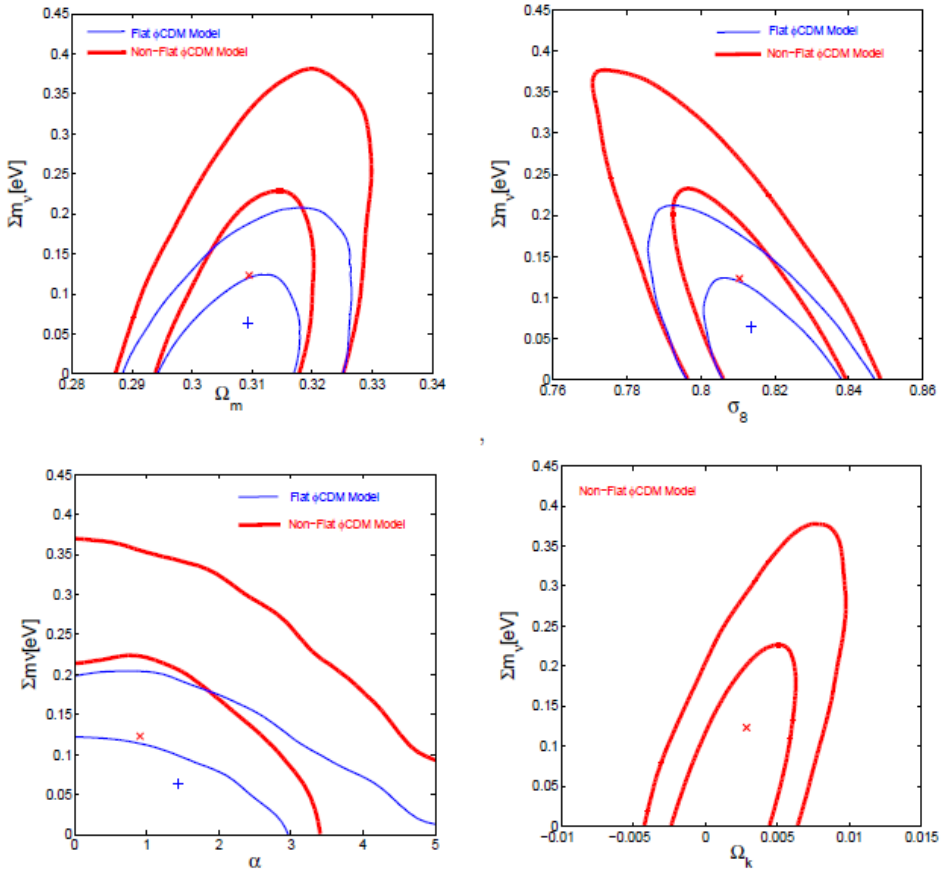

Figure 18. 1σ and 2σ confidence level contours constraints on parameters of the spatially flat and spatially non-flat scalar field ϕCDM model with the inverse power-law potential from a joint analysis using the HST H_0 prior in the scenario with three species of degenerate massive neutrinos. (Upper left, upper right and lower left panels) Contours are presented in the $\Omega_{\rm m} - \sum m_\nu$, $\sigma_8 - \sum m_\nu$ and $\alpha - \sum m_\nu$ planes. The thin blue (thick red) lines correspond to constraints in the spatially flat (spatially non-flat) universe. The "+" ("x") denotes the mean values of the pair in the spatially flat (spatially non-flat) universe. (Lower right panel) Contours are in the $\Omega_{\rm k} - \sum m_\nu$ plane for the spatially non-flat universe. The "x" denotes the mean values of the $(\Omega_{\rm k}, \sum m_\nu)$ pair. The figure is adapted from [243].

Park & Ratra [246] constrained the **spatially flat tilted** and **spatially non-flat untilted ϕCDM-RP inflation model** by analyzing CMB temperature anisotropy angular power spectrum data from the Planck 2015 mission [247], BAO peak length scale measurements [26], a Pantheon collection of 1048 SNe Ia apparent magnitude measurements over the broader redshift range of $0.01 < z < 2.3$ [163], Hubble parameter observation [21,25,28,30–34,211,248], and LSS growth rate measurements [25] (see Figures 19 and 20). Constraints on parameters of the spatially non-flat model was improved from 1.8σ to more than 3.1σ confidence level by combining CMB temperature anisotropy data with other datasets. Present observations favor a spatially closed universe with the spatial curvature contributing about two-thirds of a percent of the current total cosmological energy budget. The spatially flat tilted ϕCDM model is a 0.4σ better fit to the observational data than is the standard spatially flat tilted ΛCDM model, i.e., current observational data allow for the possibility of dynamical dark energy in the universe. The spatially non flat tilted ϕCDM model better fits the DES bounds on the rms amplitude of mass fluctuations σ_8 as a function of the matter density parameter at present epoch $\Omega_{\rm m0}$ but it does not provide such a good agreement with the larger multipoles of Planck 2015 CMB temperature anisotropy data as the spatially flat tilted ΛCDM model.

Preprints (www.preprints.org) | NOT PEER-REVIEWED | Posted: 27 October 2023 doi:10.20944/preprints202310.1818.v1

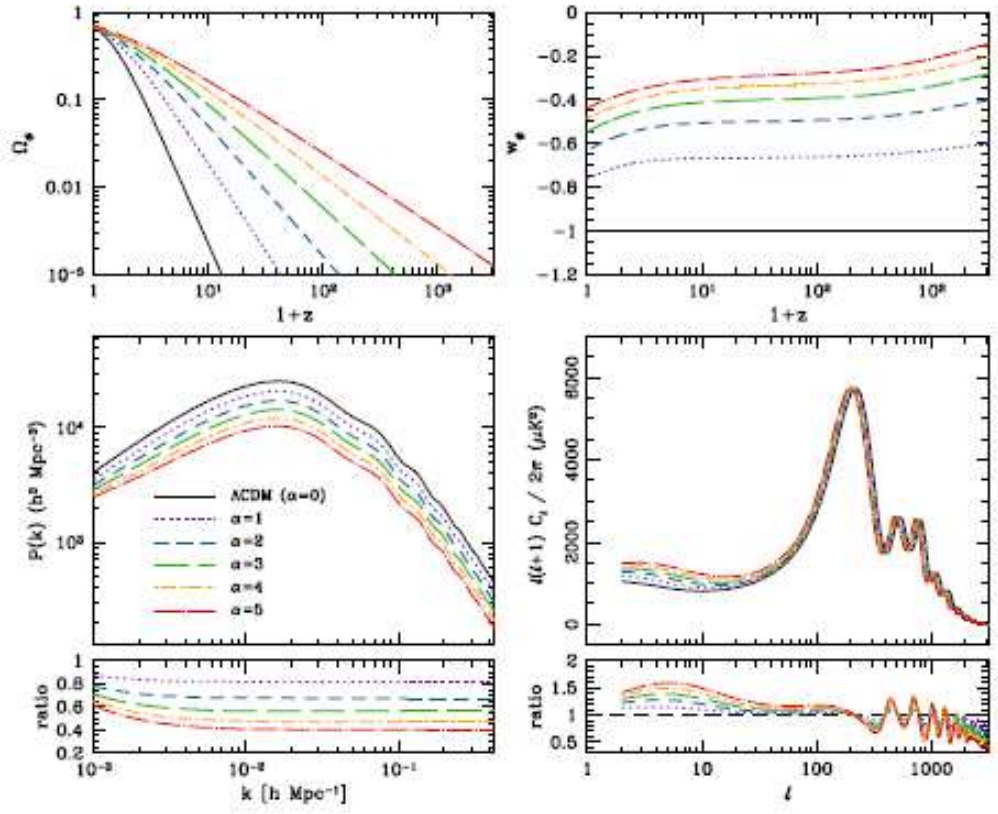

Figure 19. (**Upper** panels) Evolution of the EoS parameter w_ϕ and dark energy density parameter Ω_ϕ in the tilted spatially flat ϕCDM model for the range of values of α parameter $\alpha \in (1,5)$. The black solid curve accords to the ΛCDM model, which corresponds to reduced ϕCDM model with $\alpha = 0$. (**Middle** panels) Theoretical predictions for matter density and CMB temperature anisotropy angular power spectra for the ϕCDM model depending on parameter α. (**Lower** panels) Ratios of the ϕCDM model power spectra relative to the ΛCDM model. The figure is adapted from [246].

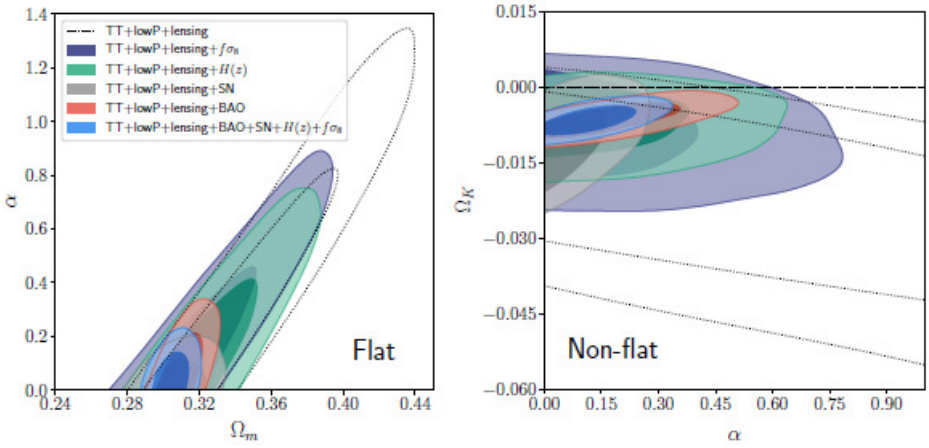

Figure 20. 1σ and 2σ confidence level contours. (**Left** panel) In the $\Omega_m - \alpha$ plane for the tilted spatially flat scalar field ϕCDM model. (**Right** panel) In the $\alpha - \Omega_k$ plane for the untilted spatially non-flat scalar field ϕCDM model. Constraints are derived from Planck CMB TT + lowP + lensing and non-CMB datasets. The horizontal dashed line indicates the spatially flat curvature with $\Omega_k = 0$. For the spatially non-flat ϕCDM model constrained with TT + lowP + lensing, the $h > 0.45$ prior has been used. The figure is adapted from [246].

Preprints (www.preprints.org) | NOT PEER-REVIEWED | Posted: 27 October 2023 doi:10.20944/preprints202310.1818.v1

Constraints on model parameters in the **XCDM** and **ϕCDM-RP (spatially flat tilted) inflation models** using the compilation of CMB [247] and BAO data [22–24,249–251] were derived by Ooba et al. [249]. The authors calculated the angular power spectra of the CMB temperature anisotropy using the CLASS code of Blas et al. (2011) [250], and executed the MCMC analysis with Monte Python (Audren et al. [251]). Results of this analysis are shown in Figure 21.

Having one additional parameter compared to the standard spatially-flat ΛCDM model, both ϕCDM and XCMB models better fit the TT + lowP + lensing + BAO peak length scale data than does the standard spatially-flat ΛCDM model. For the ϕCDM model, $\triangle\chi^2 = -1.60$, and for the XCDM model, $\triangle\chi^2 = -1.26$ relative to the ΛCDM model. The improvement over the standard spatially-flat ΛCDM model in 1.3σ and in 1.1σ for the XCDM model are not significant, but these dynamical dark energy models cannot be ruled out. Both the ϕCDM and XCMB dynamical dark energy models reduce the tension between the Planck 2015 (Aghanim et al. [247]) CMB temperature anisotropy and the weak lensing constraints of the rms amplitude of mass fluctuations σ_8.

Preprints (www.preprints.org) | NOT PEER-REVIEWED | Posted: 27 October 2023 doi:10.20944/preprints202310.1818.v1

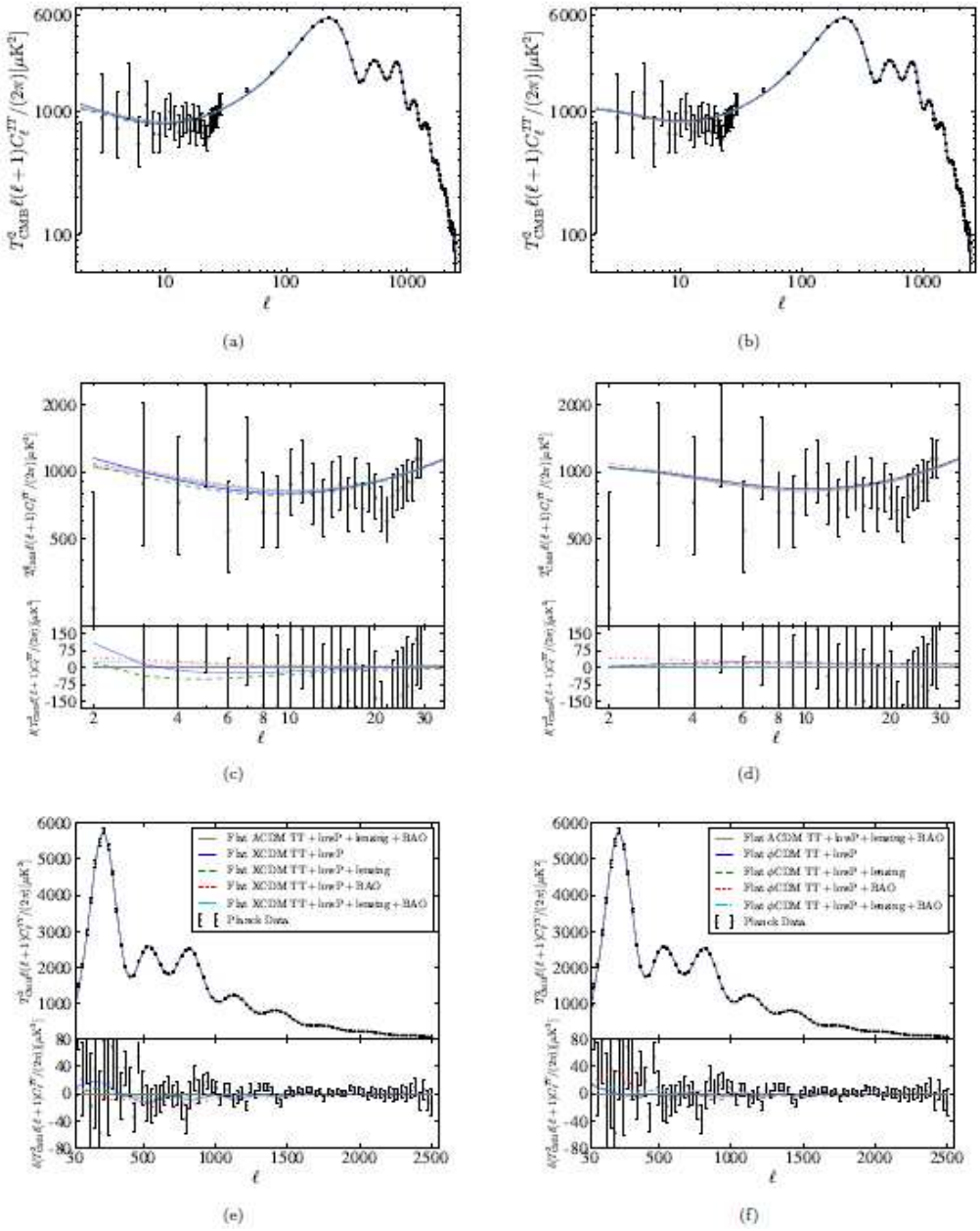

Figure 21. (**Left** panels (**a**–**e**)) The comparison of the spatially flat tilted ΛCDM model (gray solid line) with the best-fit C_l's for the XCDM model and the ϕCDM model. (**Right** panels (**b**–**f**)) The comparison of the spatially flat tilted ΛCDM model (gray solid line) with the best-fit C_l's for the ϕCDM model. The all-l region is shown on top panels. The low-l region C_l and residuals are represented on middle panels. The high-l region C_l and residuals are demonstrated on bottom panels. The figure is adapted from [249].

Park & Ratra [252] also constrained the Hubble constant H_0 value in the **spatially flat** and **spatially non-flat ΛCDM**, **XCDM**, **ϕCDM-RP models** using various combinations of datasets: BAO peak length scale measurements [26], a Pantheon collection of 1048 SNe Ia apparent magnitude measurements over the broader redshift range of $0.01 < z < 2.3$ [163], and Hubble parameter observations [21,25,28,30–34,211,248]. The resulting constraints are shown in Figure 22. According to this analysis, the dataset slightly favors to the untilted spatially non-flat dynamical XCDM and ϕCDM quintessential inflation models, as well as smaller Hubble constant H_0 values.

Preprints (www.preprints.org) | NOT PEER-REVIEWED | Posted: 27 October 2023 doi:10.20944/preprints202310.1818.v1

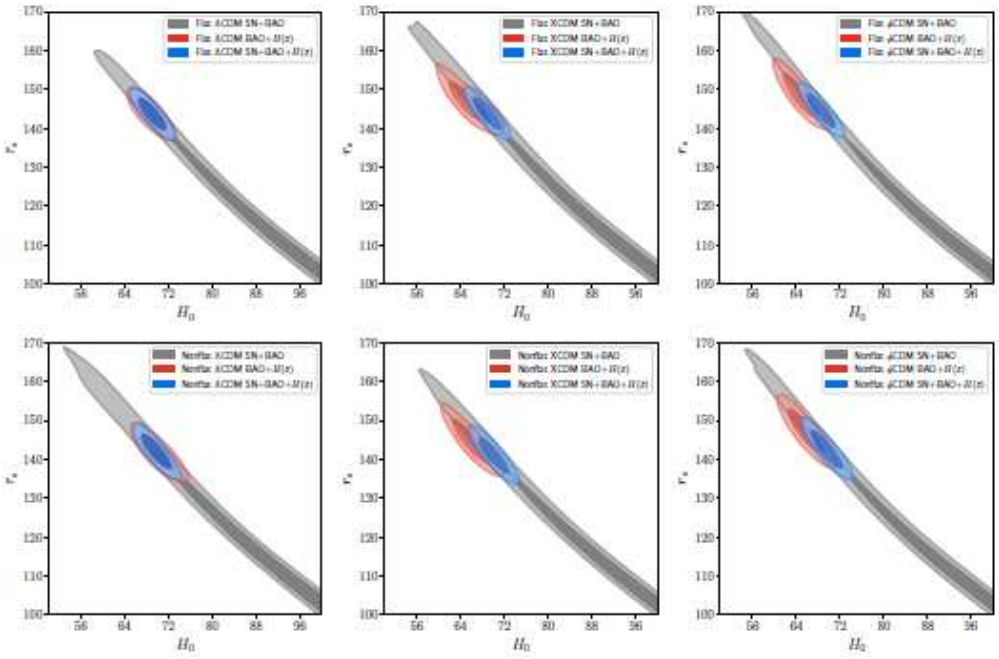

Figure 22. 1σ and 2σ confidence level contours. Hubble constant H_0 values versus sound horizon size at recombination r_* values for the spatially flat (**Upper** panels) and spatially non-flat (**Lower** panels) ΛCDM, XCDM, ϕCDM models constrained by BAO peak length scale+$H(z)$, and SNe Ia apparent magnitude+BAO peak length scale+$H(z)$ datasets. The figure is adapted from [252].

The compilation of the South Pole Telescope polarization (SPTpol) CMB temperature anisotropy data [253], alone and in combination with Planck 2015 CMB temperature anisotropy data [247] and non-CMB temperature anisotropy data, consisting of the Pantheon Type SNe Ia apparent magnitude measurements [163], BAO peak length scale measurements [22,24–26,248], Hubble parameter $H(z)$ data [21,28,30–34,211], and LSS growth rate data [25] was used by Park & Ratra [254] to obtain constraints on parameters of the **spatially flat** and **untilted spatially non-flat ΛCDM**, **XCDM**, **scalar field ϕCDM-RP quintessential quintessential inflation models** The results obtained from constraints on parameters of the untilted spatially non-flat ϕCDM model with the inverse power-law RP potential using only SPTpol CMB temperature anisotropy data and with combination of other datasets are presented in Figure 23. In each dark energy model, constraints on cosmological parameters from SPTpol measurements, Planck CMB temperature anisotropy and non-CMB temperature anisotropy measurements are largely consistent with one another. Smaller angular scale SPTpol measurements (used jointly with only Planck CMB temperature anisotropy data or with the combination of Planck CMB temperature anisotropy data and non-CMB temperature anisotropy data) favor the untilted spatially closed models.

Preprints (www.preprints.org) | NOT PEER-REVIEWED | Posted: 27 October 2023 doi:10.20944/preprints202310.1818.v1

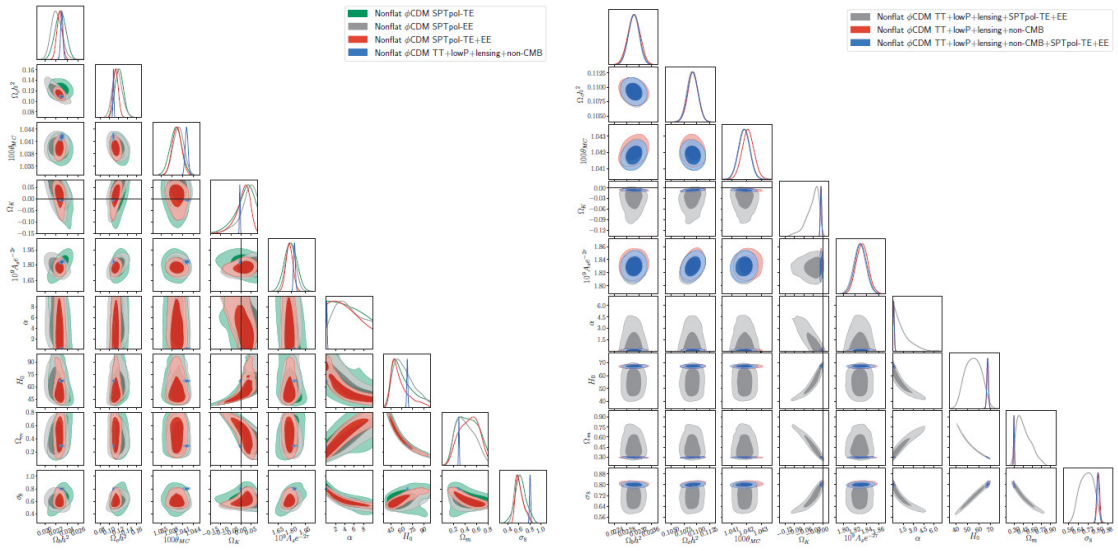

Figure 23. 1σ, 2σ and 3σ confidence level contours constraints on parameters of the untilted spatially non-flat scalar field ϕCDM model with the inverse power-law RP potential. (**Left** panel) From Planck 2015 data (TT+lowP+lensing) together with non-CMB temperature anisotropy datasets: SNe Ia apparent magnitude, BAO peak length scale, $H(z)$, and LSS growth rate are also presented. (**Right** panel) From the Planck TT+lowP+lensing measurements, non-CMB temperature anisotropy dataset, and SPTpol TE+EE measurements. Dotted straight lines denote the flat hypersurface with $\Omega_{k0} = 0$. The figure is adapted from [254].

Di Valentino et al. [88] explored the **IDE models** to find out if these models can resolve both the Hubble constant H_0 tension problem of the standard **spatially flat ΛCDM model** and resolve the contradictions between observations of Hubble constant in high and low redshifts in the **spatially non-flat ΛCDM** scenario.

The authors constrained on parameters of the **spatially flat IDE** and **ΛCDM models** as well as the **spatially non-flat IDE** and **ΛCDM models** applying CMB Planck 2018 data [13], BAO [22,24,25] measurements, 1048 data points in the redshift range $z \in (0.01, 2.3)$ of the Pantheon SNe Ia luminosity distance data [163], a Gaussian prior of the Hubble constant ($H_0 = 74.03 \pm 1.42$ km s^{-1}Mpc^{-1} at 1σ CL), obtained from a reanalysis of HST data by the SH0ES collaboration [81].

Based on the results of this observational analysis, it was found that the Planck 2018 CMB data favor spatially closed hypersurfaces at more than 99% CL (with a significance of 5σ). While a larger value of the Hubble constant, i.e., alleviation of the Hubble constant tension (with a significance of 3.6σ) has been obtained for the spatially non-flat IDE models. The authors concluded that searches for other forms of the interaction function ξ and the EoS for the dark energy component in IDE models are needed, which may further ease the tension of the Hubble constant. 1σ and 2σ confidence level contours on parameters of the spatially non-flat IDE model are shown in Figure 24.

Preprints (www.preprints.org) | NOT PEER-REVIEWED | Posted: 27 October 2023 doi:10.20944/preprints202310.1818.v1

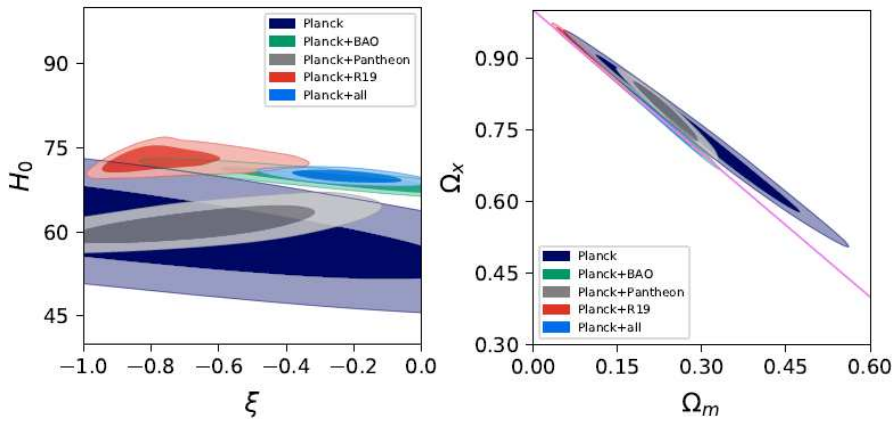

Figure 24. 1σ and 2σ confidence level contours on parameters of the spatially non-flat IDE model, presented in (H_0, ξ) plane (**Left** panel) and in $(\Omega_\Lambda, \Omega_m)$ plane (**Right** panel). The figure is adapted from [88].

3.3. Large Scale Structure Growth Rate Data

Another potentially powerful probe of ϕCDM signatures is the growth rate in low redshift LSS. The growth rate is expected to be stronger in ϕCDM models compared to their ΛCDM counterparts.

Pavlov et al. [255] constrained the **spatially flat ϕCDM-RP**, the **XCDM**, the **wCDM**, and the **ΛCDM models** from future LSS growth rate data, by considering that the full sky space-based survey will observe H_α-emitter galaxies over 15000 deg^2 of the sky. For the bias and density of observed galaxies, they applied the predictions of Orsi et al. [256] and Geach et al. [257], respectively. They also assumed that half of the galaxies would be detected within the reliable redshift range, which roughly reflects the expected outcomes of proposed space missions, such as the ESA Euclidean Space Telescope (EUCLID) mission and the NASA Wide-Field Infrared Telescope (WFIRST) mission. The obtained results are shown in Figure 25, where we see that measurements of the LSS growth rate in the near future will be able to constrain scalar field ϕCDM models with an accuracy of about 10%, considering the fiducial spatially flat ΛCDM model, an improvement of almost an order of the magnitude compared to those from currently available datasets [213,258–263]. Constraints on the growth index parameter γ are the most restrictive in the ΛCDM model than in other models. In the ϕCDM model, constraints on the growth index parameter γ are about a third more tighter than in the wCDM and XCDM models.

Preprints (www.preprints.org) | NOT PEER-REVIEWED | Posted: 27 October 2023 doi:10.20944/preprints202310.1818.v1

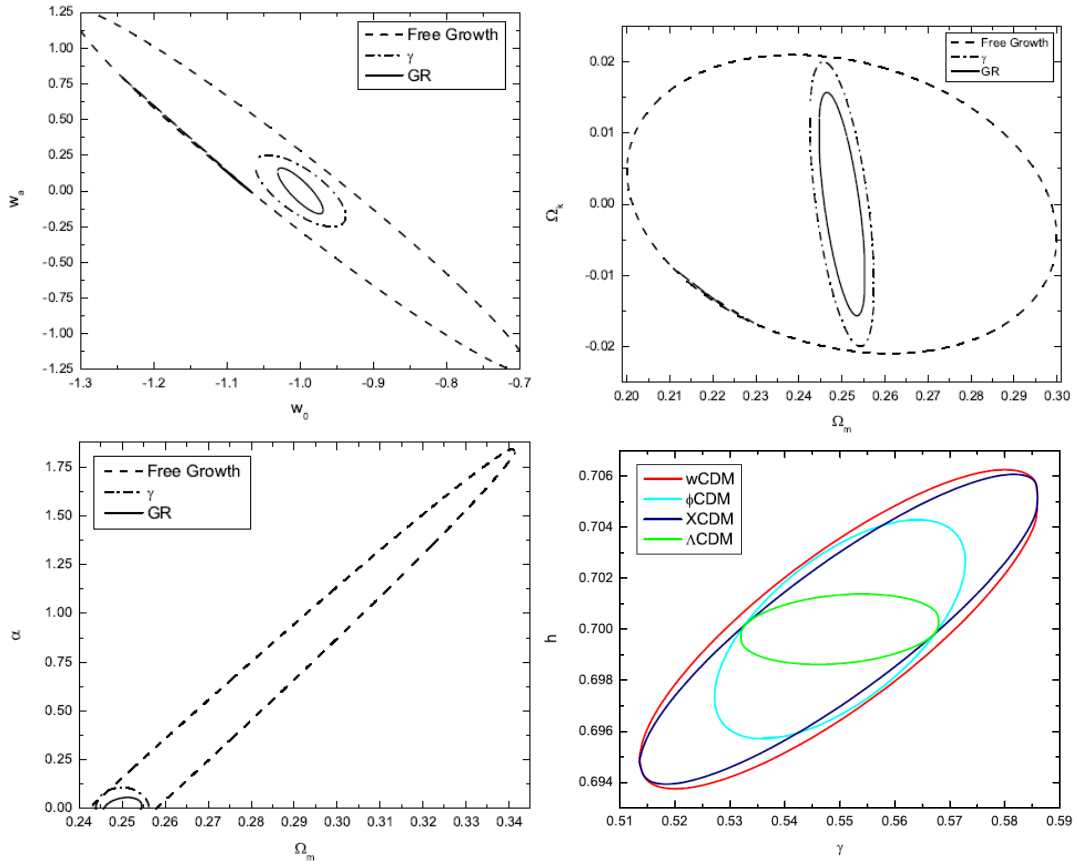

Figure 25. (Left upper panel) 1σ confidence level contours constraints on parameters w_a and w_0 in the wCDM model. (Right upper panel) 1σ confidence level contours constraints on parameters $\Omega_{\rm k}$ and $\Omega_{\rm m}$ in the wCDM model. (Left lower panel) 1σ confidence level contour constraints on parameters α and $\Omega_{\rm m}$ in the scalar field spatially flat ϕCDM model with the inverse power-law RP potential. (Right lower panel) 1σ confidence level contour constraints on the normalized Hubble constant h and the parameter γ describing deviations from general relativity for various dark energy models. The figure is adapted from [255].

Pavlov et al. [264] also obtained constraints on **the above DE models** from Hubble parameter $H(z)$ observations [28,30,211,212], from Union2.1 compilation of 580 SNe Ia apparent magnitude measurements [210], and a compilation of 14 independent LSS growth rate measurements within the redshift range $0.067 \leq z \leq 0.8$ [21,22,213,265]. The authors performed two joint analyses, first for the combination of $H(z)$ and SNe Ia apparent magnitude data, and the other for measurements of LSS growth rate, Hubble parameter $H(z)$ and SNe Ia apparent magnitude; the results of these analyses are presented in Figure 26. Constraints on cosmological parameters of the spatially flat ϕCDM model from LSS growth rate data are quite restrictive. In combination with SNe Ia apparent magnitude versus redshift data and Hubble parameter measurements, LSS growth rate data are consistent with the standard spatially flat ΛCDM model, as well as with the spatially flat ϕCDM model.

Preprints (www.preprints.org) | NOT PEER-REVIEWED | Posted: 27 October 2023 doi:10.20944/preprints202310.1818.v1

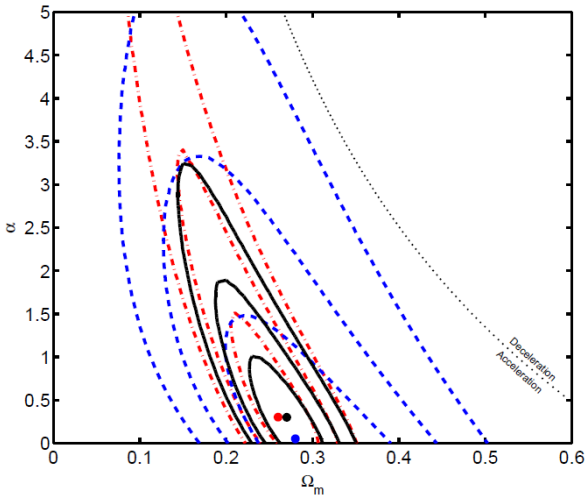

Figure 26. 1 σ, 2 σ, and 3 σ confidence level contours constraints on parameters of the spatially flat scalar field ϕCDM model with the inverse power-law RP potential from LSS growth rate measurements (blue dashed lines with blue filled circle at best-fit $(\Omega_{\rm m}, \alpha) = (0.28, 0.052)$, $\chi^2_{\rm min}/{\rm dof} = 8.62/12$); SNe Ia apparent magnitude+$H(z)$ data (red dot-dashed lines with red filled circle at best-fit $(\Omega_{\rm m}, \alpha) = (0.26, 0.302)$, $\chi^2_{\rm min}/{\rm dof} = 562/598$); and a combination of all datasets (black solid lines and black filled circle at the best-fit $(\Omega_{\rm m}, \alpha) = (0.27, 0.300)$, $\chi^2_{\rm min}/{\rm dof} = 570/612$. The horizontal axis with $\alpha = 0$ corresponds to the standard spatially flat ΛCDM model, and the curved dotted line denotes zero acceleration models. The figure is adapted from [264].

Avsajanishvili et al. [266] constrained the parameters $\Omega_{\rm m}$ and α in the **spatially flat ϕCDM-RP model**. Applying only measurements of the LSS growth rate [267], the authors obtained a strong degeneracy between the model parameters $\Omega_{\rm m}$ and α, Figure 27 (Left panel). This was followed by obtaining constraints from a compilation of data from the LSS growth rate measurements [267], and the distance-redshift ratio of the BAO peak length scale observations and prior distance from CMB temperature anisotropy [268], which eliminated the degeneracy between $\Omega_{\rm m}$ and α, giving $\Omega_{\rm m} = 0.30 \pm 0.04$ and $0 \leq \alpha \leq 1.30$ at 1σ confidence level (the best-fit value for the model parameter α is $\alpha = 0$). Constraints on $\Omega_{\rm m}$ and α from data compilation of Gupta et al. (2012) and Giostri et al. (2012) are presented in Figure 27 (Right panel).

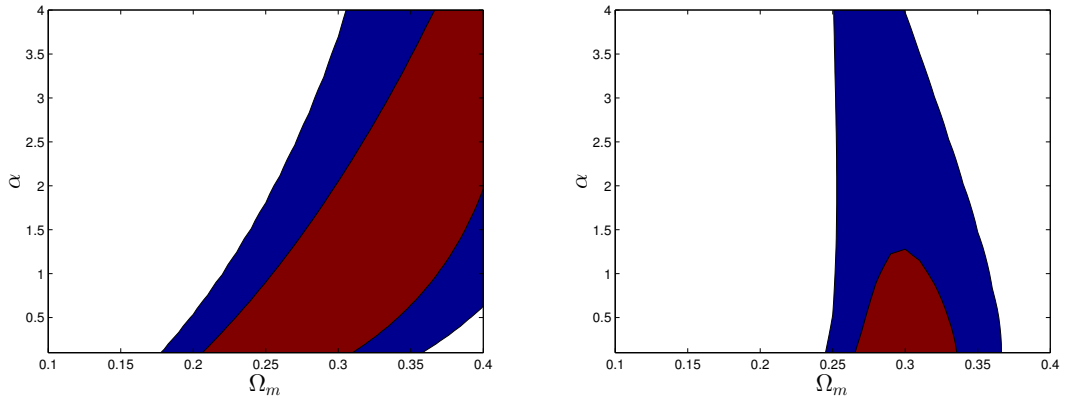

Figure 27. 1σ and 2σ confidence level contours constraints on parameters $\Omega_{\rm m}$ and α in the scalar field ϕCDM model with the inverse power-law RP potential. (**Left** panel) Constraints are obtained from the LSS growth rate data [267]. (**Right** panel) Constraints are obtained from the data compilation of Gupta et al. (2012) and Giostri et al. (2012). The figure is adapted from [266].

Preprints (www.preprints.org) | NOT PEER-REVIEWED | Posted: 27 October 2023 doi:10.20944/preprints202310.1818.v1

Avsajanishvili et al. [269] also constrained various **quintessence** and **phantom scalar field ϕCDM models** presented in Tables 1 and 2 using observational data predicted for the Dark Energy Spectroscopic Instrument (DESI) [248]. The parameters of these models were constrained using MCMC methods by comparing measurements of the expansion rate of the universe $H(z)$, the angular diameter distance, and the LSS growth rate predicted for the standard spatially flat ΛCDM model with corresponding values calculated for the ϕCDM models. Results of constraints for the Zlatev-Wang-Steinhardt potential, the phantom pNGb potential, and the inverse power-law RP potential are shown in Figures 28 and 29. To compare quintessence and phantom models, Bayesian statistical tests were conducted, namely the Bayes factor, as well as the AIC and BIC information criteria, were calculated. The ϕCDM scalar field models could not be unambiguously preferred, from the DESI predictive data, over the standard ΛCDM spatially flat model, the latter still being the most preferred dark energy model. The authors also investigated how the ϕCDM models can be approximated by the CPL parametrization, by plotting the CPL-ΛCDM 3 sigma confidence level contours, using MCMC techniques, and displayed on them the largest ranges of the current EoS parameters for each ϕCDM model. These ranges were obtained for different values of model parameters or initial conditions from the prior ranges. The authors classified the scalar field models based on whether they can or cannot be distinguished from the standard spatially flat ΛCDM model at the present epoch, as seen in Figure 31. They found that all studied models can be divided into two classes: models that have attractor solutions and models whose evolution depends on initial conditions.

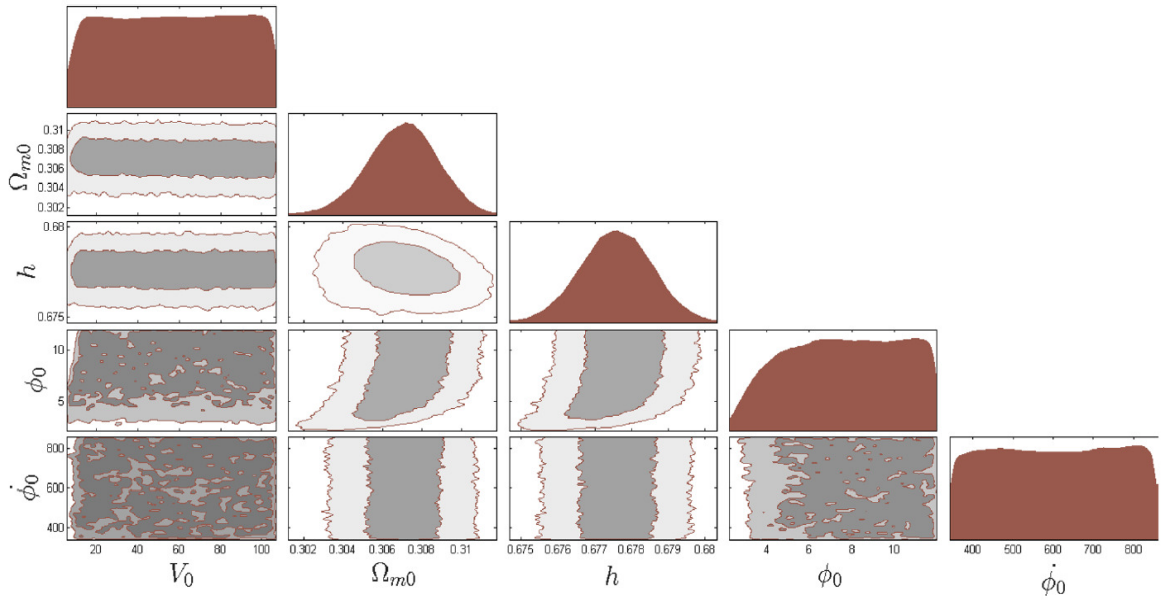

Figure 28. 1σ and 2σ confidence level contour plots for various pairs of free parameters (V_0, Ω_{m0}, h, ϕ_0, $\dot{\phi}_0$), for which the spatially flat ϕCDM model with the Zlatev-Wang-Steinhardt potential is in the best-fit with the standard spatially flat ΛCDM model. The figure is adapted from [269].

Preprints (www.preprints.org) | NOT PEER-REVIEWED | Posted: 27 October 2023 doi:10.20944/preprints202310.1818.v1

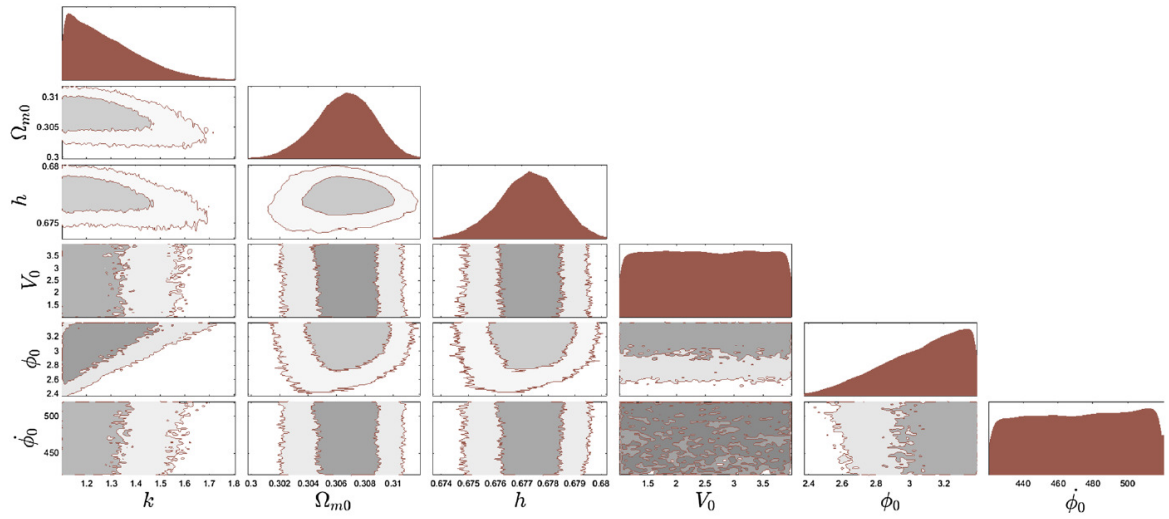

Figure 29. 1σ and 2σ confidence level contour plots for various pairs of free parameters (k, $\Omega_{\rm m0}$, h, V_0, ϕ_0, $\dot{\phi}_0$), for which the spatially flat ϕCDM model with the phantom PNGB potential is in the best-fit with the standard spatially flat ΛCDM model. The figure is adapted from [269].

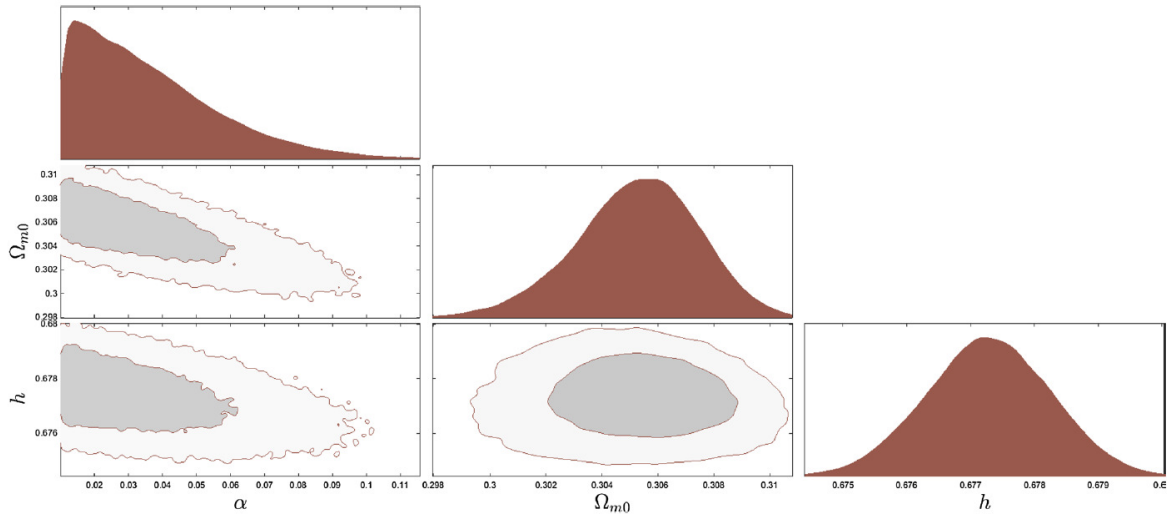

Figure 30. 1σ and 2σ confidence level contour plots for various pairs of free parameters (α, $\Omega_{\rm m0}$, h), for which the spatially flat ϕCDM model with the RP potential is in the best-fit with the standard spatially flat ΛCDM model. The figure is adapted from [269].

Preprints (www.preprints.org) | NOT PEER-REVIEWED | Posted: 27 October 2023 doi:10.20944/preprints202310.1818.v1

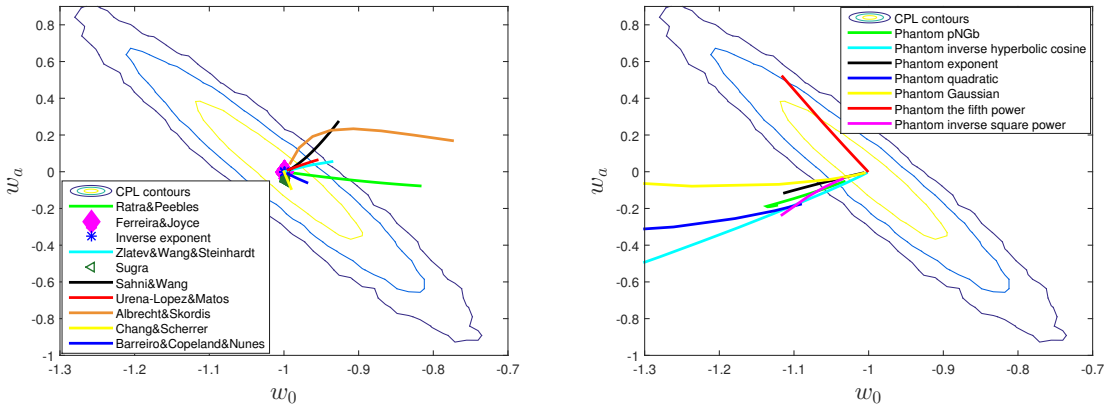

Figure 31. (**Left** panel) The comparison of the possible w_0 and w_a values for quintessence dark energy potentials in the spatially flat scalar field ϕCDM models with the CPL - ΛCDM 1σ, 2σ, and 3σ confidence level contours. (**Right** panel) The comparison of possible w_0 and w_a values for phantom dark energy potentials in the spatially flat scalar field ϕCDM models with the CPL - ΛCDM 1σ, 2σ, and 3σ confidence level contours. The figure is adapted from [269].

Peracaula et al. [270] constrained the **spatially flat ΛCDM**, **XCDM**, and **ϕCDM-RP models** by constructing three datasets: DS1/SP consisting of SNe Ia apparent magnitude+$H(z)$+BAO peak length scale+LSS growth rate+CMB temperature anisotropy data with matter power spectrum SP; DS1/BSP consisting of SNe Ia apparent magnitude+$H(z)$+BAO peak length scale+LSS growth rate+CMB temperature anisotropy data with both matter power spectrum and bispectrum; and DS2/BSP, which involves BAO peak length scale+LSS growth rate+CMB temperature anisotropy data with both matter power spectrum and bispectrum. These datasets include 1063 SNe Ia apparent magnitude data [79,163], 31 measurements of $H(z)$ from cosmic chronometers [35,211], 16 BAO peak length scale data [271,272], LSS growth rate data, specifically 18 points from data [21,272,273], one point from the weak lensing observable S_8 [274], full CMB likelihood from Planck 2015 TT+lowP+lensing [12]. The obtained constraints are shown in Figures 32 and 33. The authors tested the effect of separating the expansion history data (SNe Ia apparent magnitude+$H(z)$) from CMB temperature anisotropy characteristics and LSS formation data (BAO peak length scale+LSS), where LSS includes redshift-space distortions (RSD) and weak lensing measurements, and found that the expansion history data are not particularly sensitive to the dynamic effects of dark energy, while compilation of data BAO peak length scale+LSS+CMB temperature anisotropy is more sensitive. Also the influence of the bispectral component of the matter correlation function on the dynamics of dark energy is studied. For this, BAO peak length scale+LSS data were considered, including both the conventional power spectrum and the bispectrum. As a result, when the bispectral component is excluded, the results obtained are consistent with previous studies by other authors, which means that no clear signs of dynamical dark energy have been found in this case. On the contrary, when the bispectrum component was included in the BAO peak length scale+LSS growth rate dataset for the ϕCDM model, a significant dynamical dark energy signal was achieved at $2.5-3\sigma$ confidence level. The bispectrum can therefore be a very useful tool for tracking and examining the possible dynamical features of dark energy and their influence on the LSS formation in the linear regime.

Preprints (www.preprints.org) | NOT PEER-REVIEWED | Posted: 27 October 2023 doi:10.20944/preprints202310.1818.v1

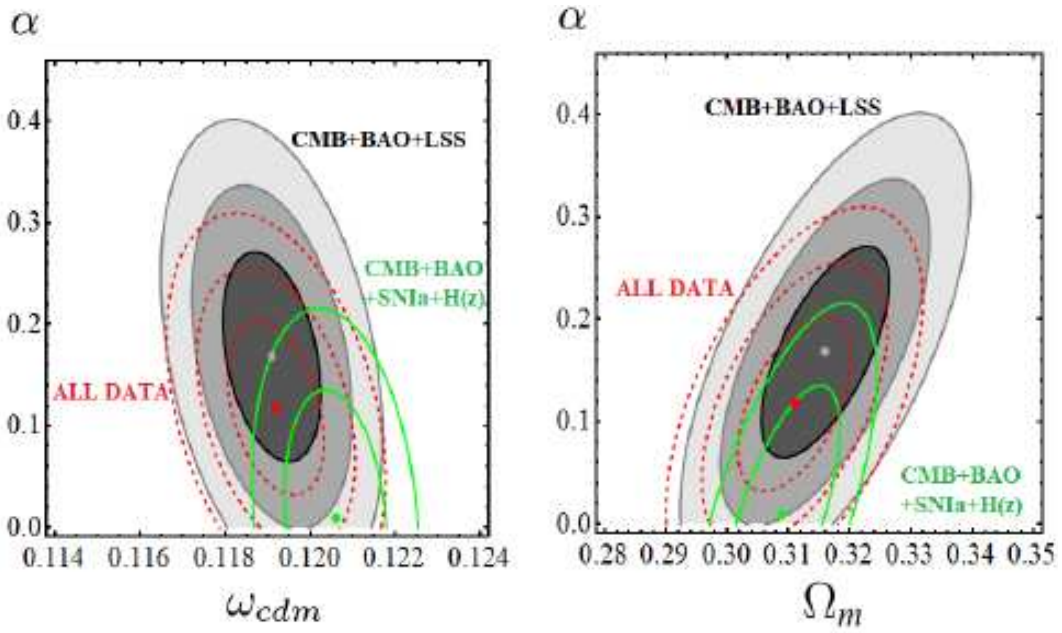

Figure 32. 1σ, 2σ and 3σ confidence level contours constraints on parameters of the spatially flat scalar field ϕCDM model with the inverse power-law RP potential using different combinations of datasets and the compressed Planck 2018 data [13]. The results obtained from DS2/BSP dataset CMB temperature anisotropy+BAO peak length scale+LSS growth rate (gray contours), DS1/BSP dataset: SNe Ia apparent magnitude+$H(z)$+BAO peak length scale+LSS growth rate+CMB temperature anisotropy (dashed red contours), and DS1/BSP dataset without LSS growth rate data CMB temperature anisotropy+BAO peak length scale+SNe Ia apparent magnitude+$H(z)$ (solid green contours). The results are presented in the $w_{\rm cdm} - \alpha$ plane (**Left** panel) and in the $w_{\rm cdm} - \Omega_{\rm m}$ plane (**Right** panel), here $w_{\rm cdm} = \Omega_{\rm m} h^2$ is a physical matter density parameter. The figure is adapted from [270].

Preprints (www.preprints.org) | NOT PEER-REVIEWED | Posted: 27 October 2023 doi:10.20944/preprints202310.1818.v1

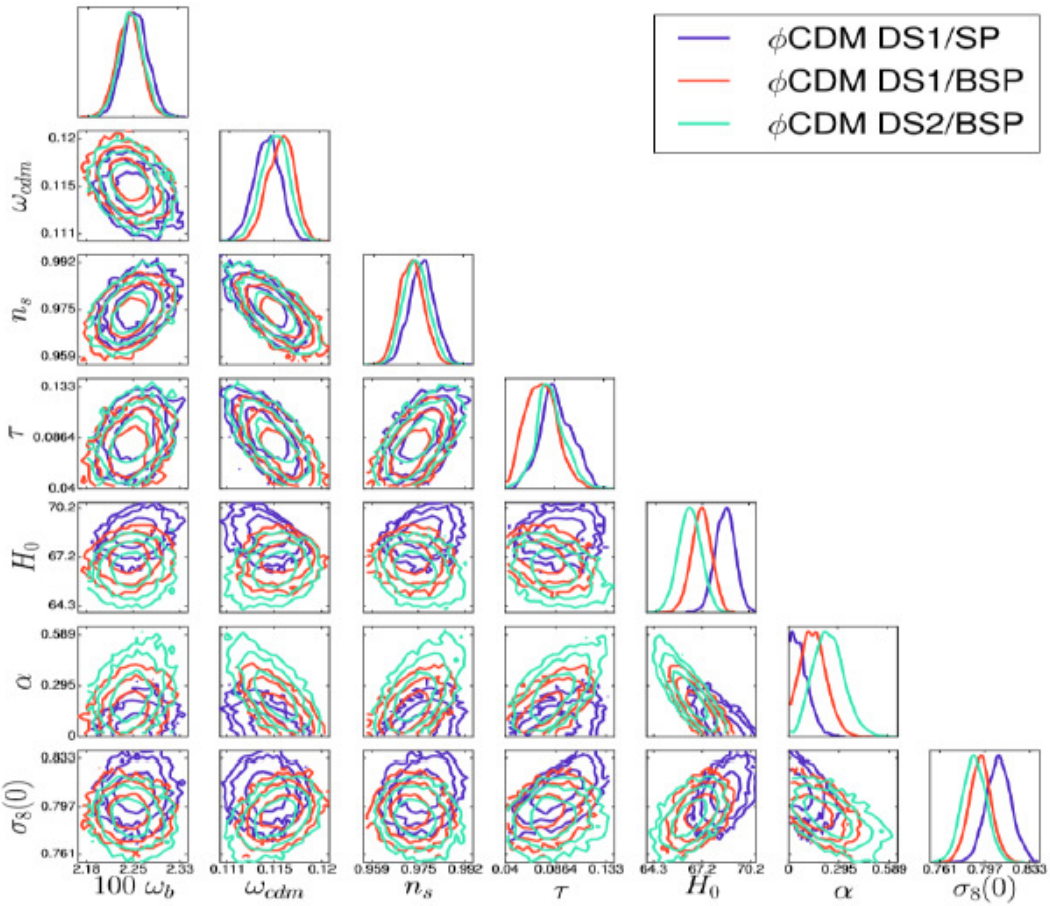

Figure 33. 1σ, 2σ and 3σ confidence level contours constraints on parameters of the spatially flat scalar field ϕCDM model with the inverse power-law RP potential from DS1/SP, DS1/BSP and DS2/BSP datasets. The figure is adapted from [270].

Park & Ratra [275] constrained the **tilted spatially flat** and **untilted spatially non-flat XCDM model** by applying the Planck 2015 CMB temperature anisotropy data [247], BAO peak length scale measurements [26], a Pantheon collection of 1048 SNe Ia apparent magnitude measurements over the broader redshift range $0.01 < z < 2.3$ [163], Hubble parameter observations [21,25,28,30–34,211,248], and LSS growth rate measurements [25], and obtained results as shown in Figures 34 and 35. These data slightly favor the spatially closed XCDM model over the spatially flat ΛCDM model at 1.2σ confidence level, while also being in better agreement with the untilted spatially flat XCDM model than with the spatially flat ΛCDM model at the 0.3σ confidence level. Current observational data is unable to rule out dynamical dark energy models. The dynamical untilted spatially nonflat XCDM model is compatible with the Dark Energy Survey (DES) limits on the current value of the rms mass fluctuations amplitude σ_8 as a function of the matter density parameter at present epoch $\Omega_{\rm m0}$, but it does not give such a good agreement with higher multipoles of CMB temperature anisotropy data, as the standard spatially flat ΛCDM model.

Preprints (www.preprints.org) | NOT PEER-REVIEWED | Posted: 27 October 2023 doi:10.20944/preprints202310.1818.v1

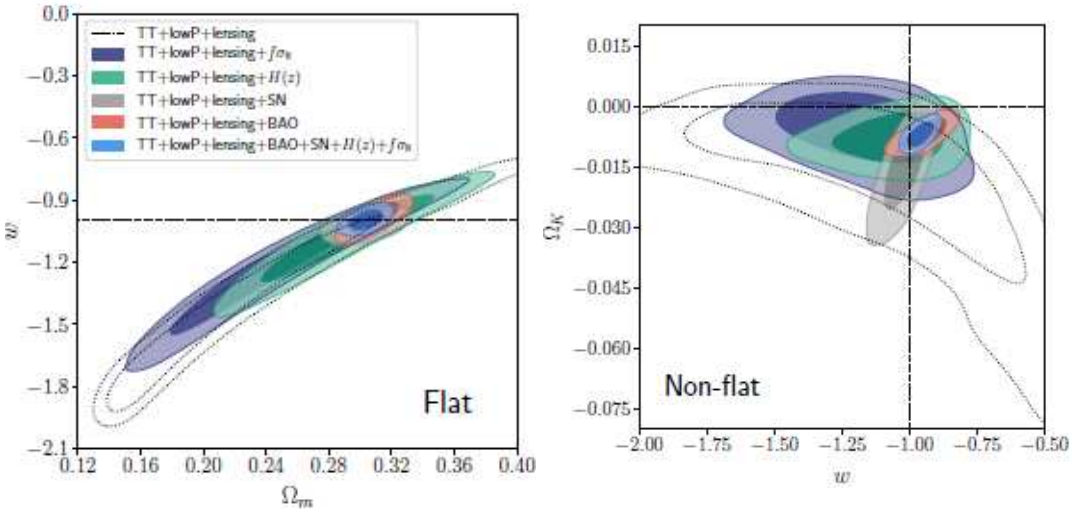

Figure 34. 1σ and 2σ confidence level contour for the tilted spatially flat XCDM model (**Left** panel) and for the untilted spatially non-flat XCDM model (**Right** panel), constrained by Planck CMB TT + lowP + lensing and non-CMB datasets. The horizontal and vertical dashed lines indicate the standard spatially flat ΛCDM model (with $w = -1$ and $\Omega_k = 0$). The figure is adapted from [275].

Preprints (www.preprints.org) | NOT PEER-REVIEWED | Posted: 27 October 2023 doi:10.20944/preprints202310.1818.v1

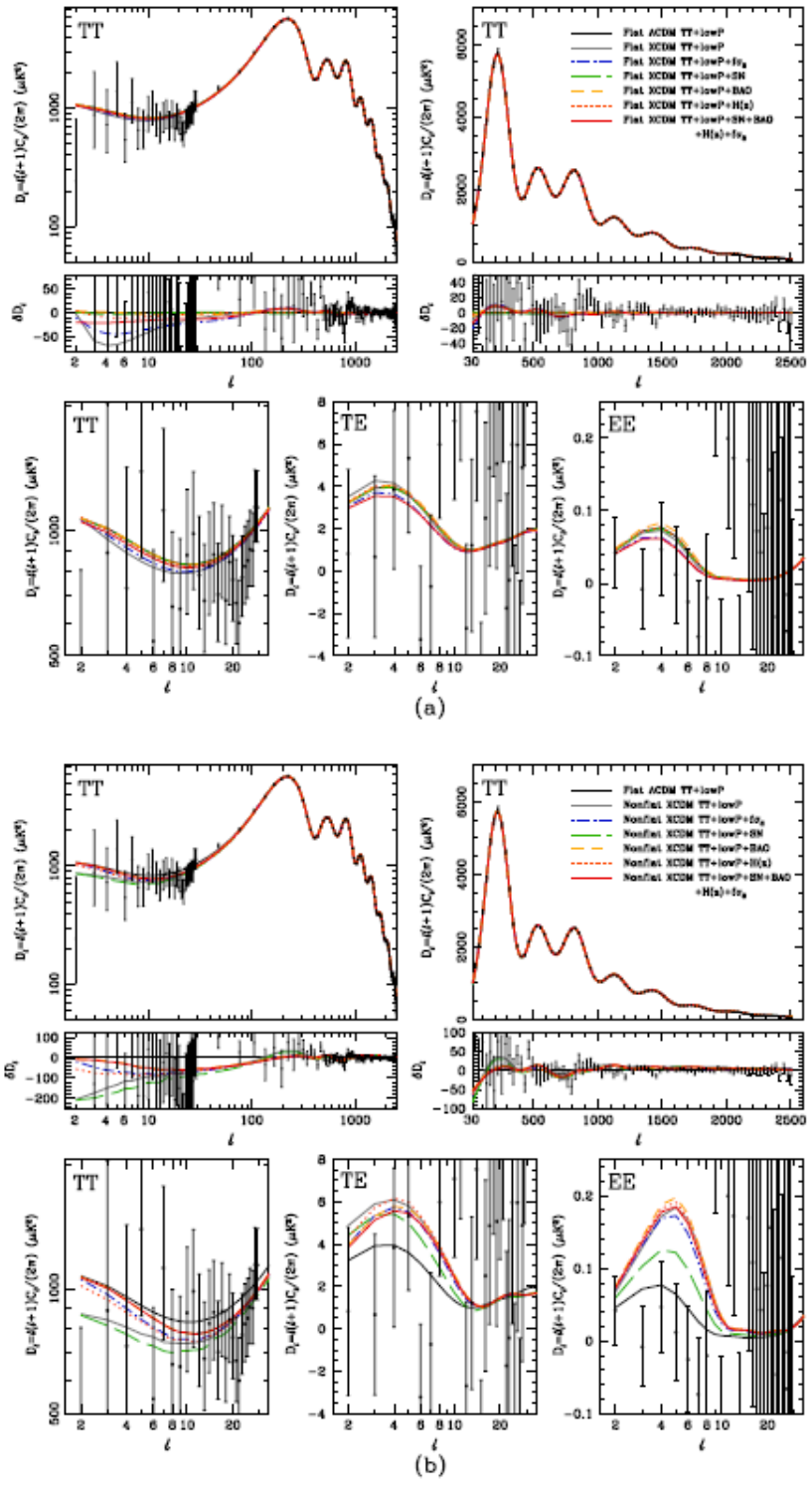

Figure 35. Best-fit CMB temperature anisotropy power spectra of (a) the tilted spatially flat XCDM model (top five panels) and (b) the untilted spatially non-flat XCDM model (bottom five panels) constrained by Plank CMB TT + lowP data (excluding lensing data) together with data of: SNe Ia apparent magnitude, BAO peak length scale, $H(z)$, and LSS growth rate. The best-fit power spectra of the tilted spatially flat ΛCDM model are shown as black curves. The residual δD_l of the TT power spectra are shown with respect to the spatially flat ΛCDM power spectrum that best fits the TT + lowP data. The high-l region C_l and residuals are shown on the bottom panels. The figure is adapted from [275].

Preprints (www.preprints.org) | NOT PEER-REVIEWED | Posted: 27 October 2023 doi:10.20944/preprints202310.1818.v1

3.4. Baryon Acoustic Oscillations Data

Samushia & Ratra [276] constrained the standard **spatially flat ΛCDM**, the **XCDM**, and the **ϕCDM-RP models** from BAO peak length scale measurements [17,20], in conjunction with WMAP measurements of the apparent acoustic horizon angle, and galaxy cluster gas mass fraction measurements [239]. These constraints are presented in Figure 36. It is seen that the measurements of Percival et al. (2007) constrain the ϕCDM model less effectively (left panel of Figure 36), while measurements of joint BAO peak length scale and galaxy cluster gas mass of the ϕCDM model give consistent and more accurate constraints than those derived from other data, i.e., $\alpha < 3.5$ (right panel of Figure 36).

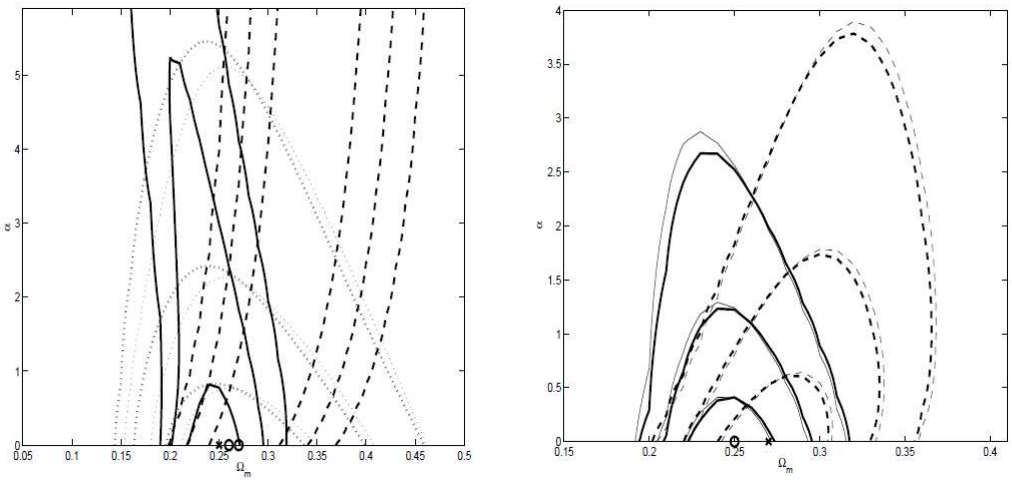

Figure 36. 1σ, 2σ and 3σ confidence level contours constraints on parameters of the scalar field ϕCDM model with the inverse power-law RP scalar field potential. The $\alpha = 0$ axis corresponds to the standard spatially flat ΛCDM model. (**Left** panel) Solid lines are constraints derived by Percival et al. (2007) using BAO peak length scale data in conjunction with WMAP data of acoustic horizon angle. Dashed lines are constraints obtained by Eisenstein et al. (2005) from BAO peak length scale data. The circle denotes the best-fit value. Two sets of dotted lines are constraints obtained from galaxy cluster gas mass fraction measurements of Samushia & Ratra (2008); thick dotted lines are derived using WMAP priors for h and $\Omega_b h^2$ while thin dotted lines are obtained for alternate priors. The cross denotes the best-fit value. (**Right** panel) Solid lines are joint constraints obtained by Percival et al. (2007) from BAO peak length scale data in conjunction with WMAP data of acoustic horizon angle and galaxy cluster gas mass fraction measurements. (The circle denotes the best-fit value with a suitable $\chi^2 \simeq 58$ for 42 degrees of freedom); dashed lines are joint constraints derived by Eisenstein et al. (2005) using BAO peak length scale data. The cross denotes the best-fit value with a suitable $\chi^2 \simeq 52$ for 41 degrees of freedom. Thick lines are derived using the WMAP priors for h and $\Omega_b h^2$, and thin lines are for alternate priors. Joint best-fit values for two prior sets overlap. Here Ω_m and α ranges are smaller than those shown on the left panel. The figure is adapted from [276].

The above models were also constrained by Samushia et al. [277] using lookback time versus redshift data [278], passively evolving galaxies data [211], current BAO peak length scale data, and SNe Ia apparent magnitude measurements. Applying a bayesian prior on the total age of the universe based on WMAP data, the authors obtained constraints on the ϕCDM model as shown in Figure 37. Constraints on the ϕCDM model by joint datasets consisting of measurements of the age of the universe, SNe Ia Union apparent magnitude and BAO peak length scale are more tighter than those obtained from datasets consisting of data of the lookback time and the age of the universe.

Preprints (www.preprints.org) | NOT PEER-REVIEWED | Posted: 27 October 2023 doi:10.20944/preprints202310.1818.v1

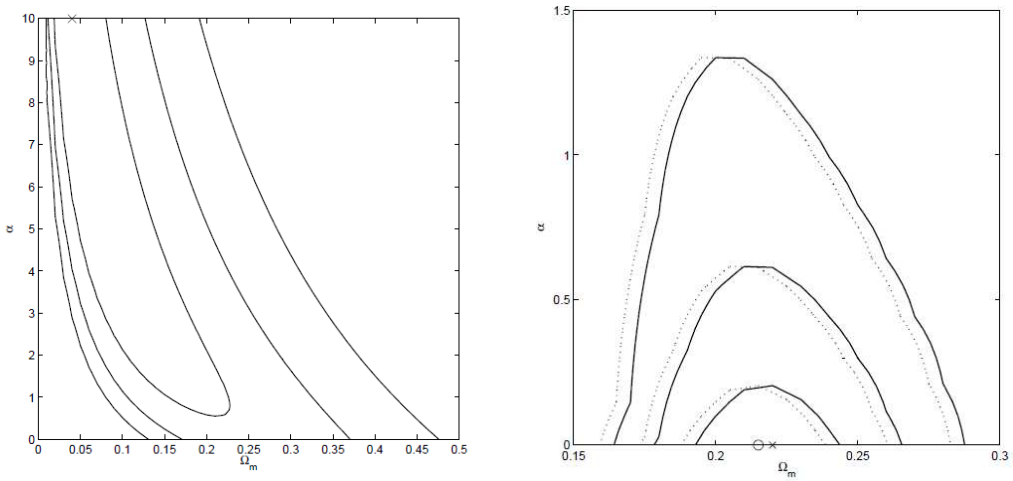

Figure 37. 1σ, 2σ and 3σ confidence level contours constraints on parameters of the scalar field ϕCDM model with the inverse power-law RP potential. The horizontal axis with $\alpha = 0$ corresponds to the standard spatially flat ΛCDM model. (**Left** panel) From the lookback time data and measurements of the age of the universe. The cross denotes the best-fit parameters $\Omega_m = 0.04$ and $\alpha = 10$ with $\chi^2 = 22$, for $\alpha = 0$ with $\chi^2 = 359$ for 346 degrees of freedom are derived using measurements of the lookback time, the age of the universe, SNe Ia apparent magnitude, and BAO peak length scale, while solid lines are derived using only SNe Ia apparent magnitude measurements and BAO peak length scale data. The cross denotes the best-fit point at $\Omega_m = 0.22$ and $\alpha = 0$ with $\chi^2 = 329$ for 307 degrees of freedom. The figure is adapted from [277].

The **quintessential inflation model with the generalized exponential potential** $V(\phi) \propto \exp(-\lambda\phi^n/M_{pl}^n)$, $n > 1$ was studied by Geng et al. [131]. The authors extended this model including massive neutrinos that are non-minimally coupled with a scalar field, obtaining observational constraints on parameters using combinations of data: CMB temperature anisotropy [244,244], BAO peak length scale from BOSS [23,263], and 11 SNe Ia apparent magnitudes from Supernova Legacy Survey (SNLS) [207]. It was found that the upper bound on possible values of the sum of neutrino masses $\sum m_\nu < 2.5$ eV is significantly larger than in the spatially flat ΛCDM model (Figure 38). The authors concluded that the model under consideration is in good agreement with observations and represents a successful scheme for the unification of primordial inflaton field causing inflation in the very early universe and dark energy causing the accelerated expansion of the universe at the present epoch.

Preprints (www.preprints.org) | NOT PEER-REVIEWED | Posted: 27 October 2023 doi:10.20944/preprints202310.1818.v1

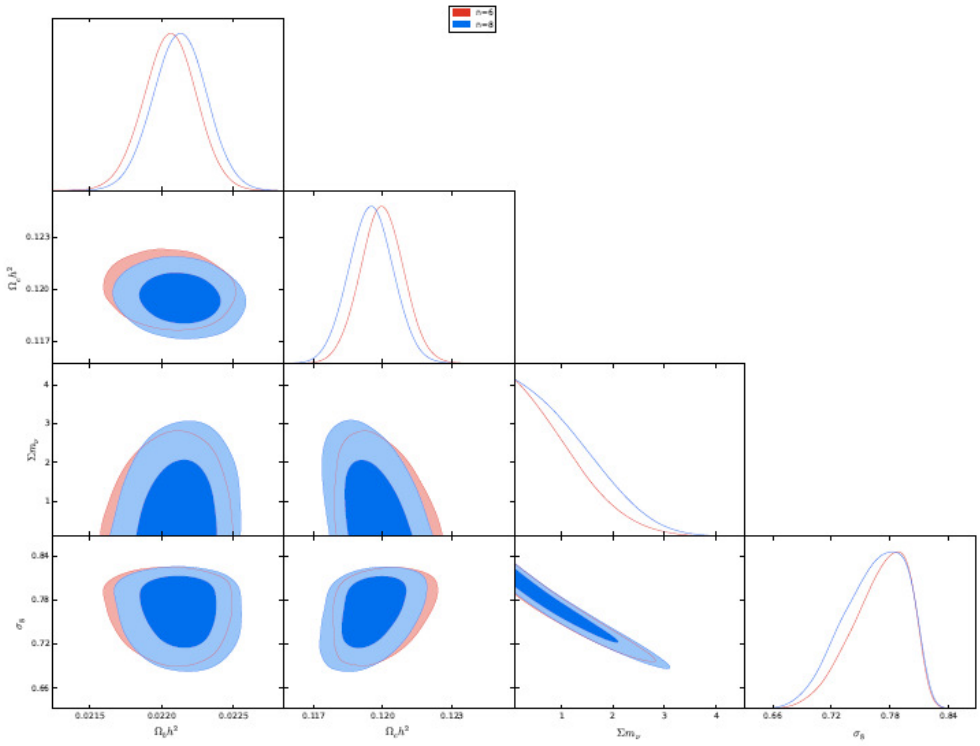

Figure 38. 1σ, 2σ confidence level contours of one and two-dimensional distributions of $\Omega_b h^2$, $\Omega_{\rm m} h^2$, $\sum m_\nu$, σ_8 for the quintessential inflation model with the exponential potential $V(\phi) \propto \exp(-\lambda\phi^n / M_{\rm pl}^n)$, $n = 6$ (orange line) and $n = 8$ (blue line). The figure is adapted from [131].

The compilation of CMB angular power spectrum data from the Planck 2015 mission [247], and BAO peak length scale measurements from the matter power spectra obtained by missions: 6dFGS [22], BOSS, LOWZ and CMASS [23], and SDSS-MGS [24] was applied by Ooba et al. [279] to obtain constraints on the **spatially non-flat quintessential inflation ϕCDM-RP model**. The theoretical angular power spectra of the CMB temperature anisotropy were calculated using the Cosmic Linear Anisotropy Solving System (CLASS) code of Blas et al. [250], and the MCMC analysis was performed with Monte Python of Audren et al. [251]. The results of this analysis are presented in Figure 39. The authors also used a physically consistent power spectrum for energy density inhomogeneities in the spatially non-flat (spatially closed) quintessential inflation ϕCDM model, and found that the spatially closed ϕCDM model provides a better fit to the lower multipole region of CMB temperature anisotropy data compared to that provided by the tilted spatially flat ΛCDM model. The former reduces the tension between the Planck and the weak lensing σ_8 constraints, while the higher multipole region of the CMB temperature anisotropy data is in better agreement with the tilted spatially flat ΛCDM model than with the spatially closed ϕCDM model (see Figure 40).

Preprints (www.preprints.org) | NOT PEER-REVIEWED | Posted: 27 October 2023 doi:10.20944/preprints202310.1818.v1

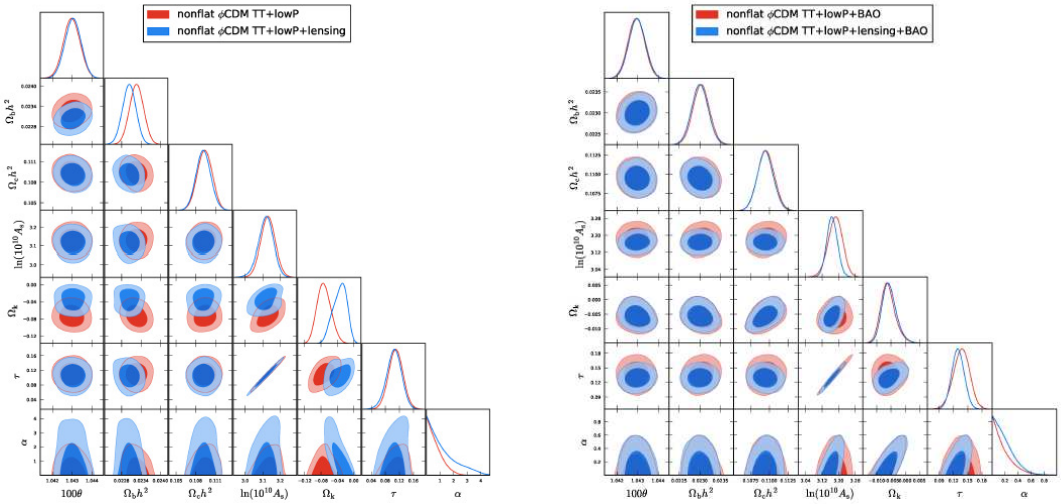

Figure 39. (**Left** panel) 1σ and 2σ confidence level contours constraints on the parameters of the spatially non-flat ϕCDM model with the RP potential, applying different datasets with marginalization of other parameters. The figure is adapted from [279].

Preprints (www.preprints.org) | NOT PEER-REVIEWED | Posted: 27 October 2023 doi:10.20944/preprints202310.1818.v1

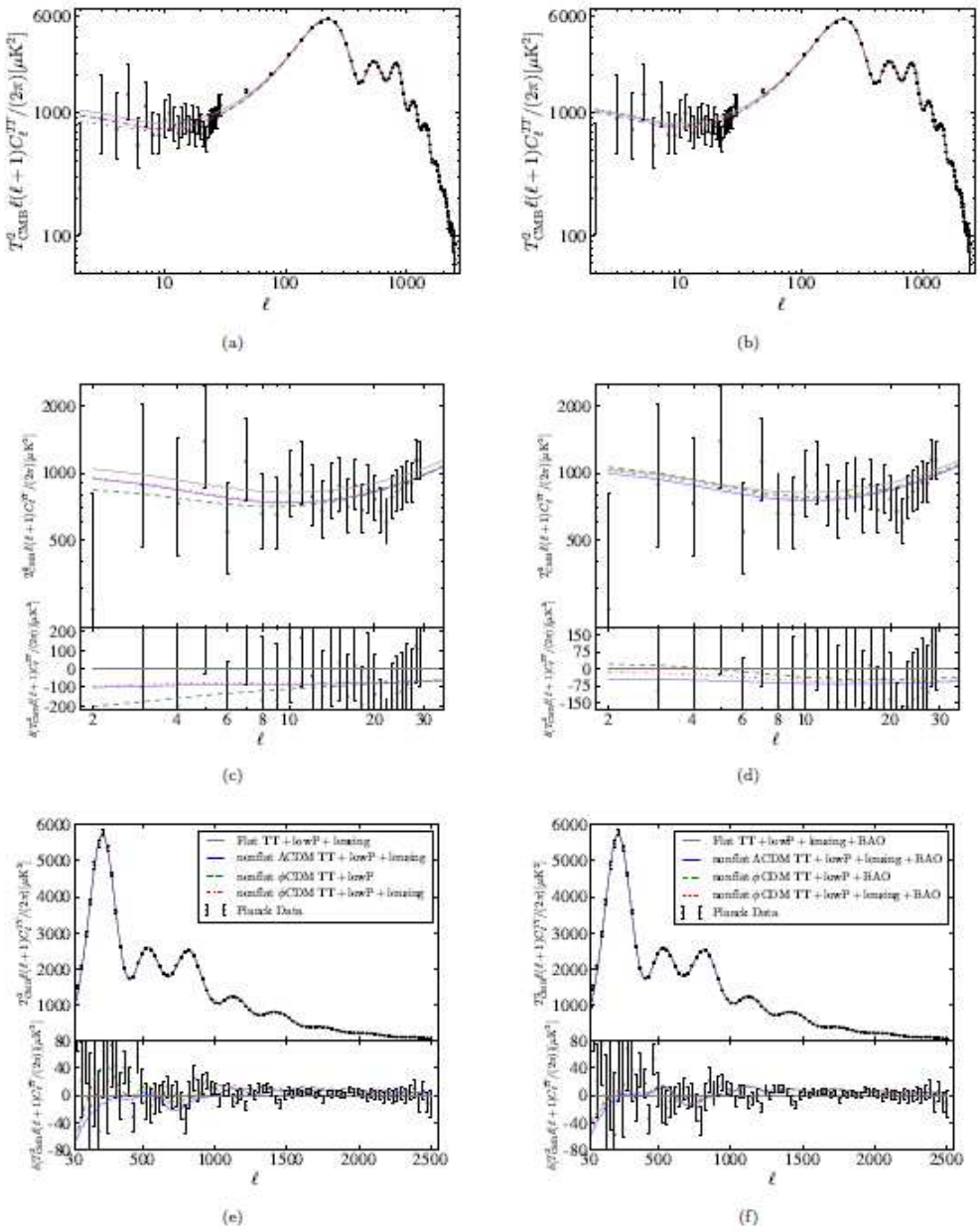

Figure 40. The C_l for the best-fit spatially non-flat ϕCDM, spatially non-flat ΛCDM and spatially flat tilted ΛCDM (gray solid line) models. (Left panels) (a), (c), (e) results obtained from only CMB temperature anisotropy data. (Right panels) (b), (d), (f) results obtained only from CMB temperature anisotropy+BAO peak length scale data. All-l regions are demonstrated on top panels. The low-l region C_l and residuals are shown on the middle panels. The high-l region C_l and residuals are presented on the bottom panels. The figure is adapted from [279].

Ryan et al. [280] constrained the parameters of the **ϕCDM-RP**, the **XCDM**, and the **ΛCDM models** from BAO peak length scale measurements [22,24–26,248], and the Hubble parameter $H(z)$ data [21,28,30–34,211]. The results obtained for the ϕCDM model are presented in Figure 41, which shows that this dataset is consistent with the standard spatially flat ΛCDM model. Depending on the value of the Hubble constant H_0 as a prior and the cosmological model under consideration, data provides evidence in favor of the **spatially non-flat scalar field ϕCDM model**.

Preprints (www.preprints.org) | NOT PEER-REVIEWED | Posted: 27 October 2023 doi:10.20944/preprints202310.1818.v1

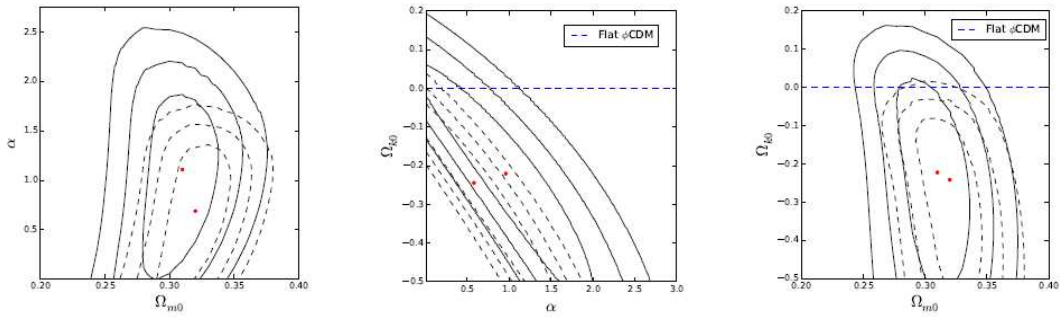

Figure 41. 1σ, 2σ and 3σ confidence level contours constraints on parameters of the spatially non-flat ϕCDM model with the RP potential. Solid (dashed) contours correspond to $H_0 = 68 \pm 2.8$ (73.24 ± 1.74) km s^{-1}Mpc^{-1} prior, the red dots indicate the location of the best-fit point in each prior case. The horizontal axis with $\alpha = 0$ denotes the spatially flat ΛCDM model. (**Left** panel) The results obtained for the Ω_{k0} marginalization. (**Center** panel) The results obtained for the Ω_{m0} marginalization. (**Right** panel) The results obtained for the parameter α marginalization. The figure is adapted from [280].

Chudaykin et al. [281] obtained constraints on the parameters of the o**CDM**, **XCDM** (here w_0**CDM**), and w**CDM** models by using the joint analysis from data of BAO peak length scale, BBN and SNe Ia apparent magnitude. The resulting constraints are completely independent of the CMB temperature anisotropy data but compete with the CMB temperature anisotropy constraints in terms of parameter error bars. The authors consequently obtained the value of the spatial curvature density parameter at present epoch $\Omega_{k0} = -0.043^{+0.036}_{-0.036}$ at 1σ confidence level, which is consistent with the spatially flat universe; in the spatially flat XCDM model, the value of the dark energy EoS parameter at present epoch $w_0 = -1.031^{+0.052}_{-0.048}$ at 1σ confidence level, which approximately equals to the value of the EoS parameter for the ΛCDM model; values of the w_0 and w_a in the CPL parameterization of the EoS parameter of the wCDM model $w_0 = -0.98^{+0.099}_{-0.11}$ and $w_a = -0.33^{+0.63}_{-0.48}$ at 1σ confidence level. The authors also found that the exclusion of the SNe Ia apparent magnitude data from the joint data analysis does not significantly weaken the resulting constraints. It means that when using a single external BBN prior, full-shape and BAO peak length scale data can provide reliable constraints independent of CMB temperature anisotropy constraints. The resulting constraints on model parameters of the spatially flat XCDM and wCDM models are shown in Figure 42. The authors also tightened the observational constraints on cosmological parameters with the inclusion of the hexadecapole ($l = 4$) moment of the redshift-space power spectrum (see Figure 43).

Preprints (www.preprints.org) | NOT PEER-REVIEWED | Posted: 27 October 2023 doi:10.20944/preprints202310.1818.v1

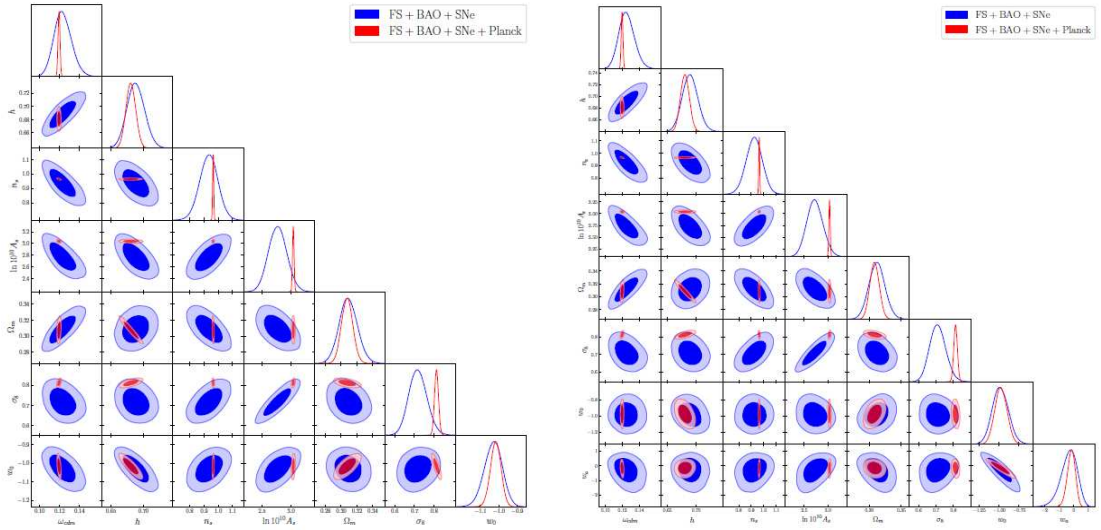

Figure 42. 1σ, 2σ confidence level contours constraints on the parameters of the spatially flat XCDM model (**Left** panel) and wCDM model (**Right** panel). The figure is adapted from [281].

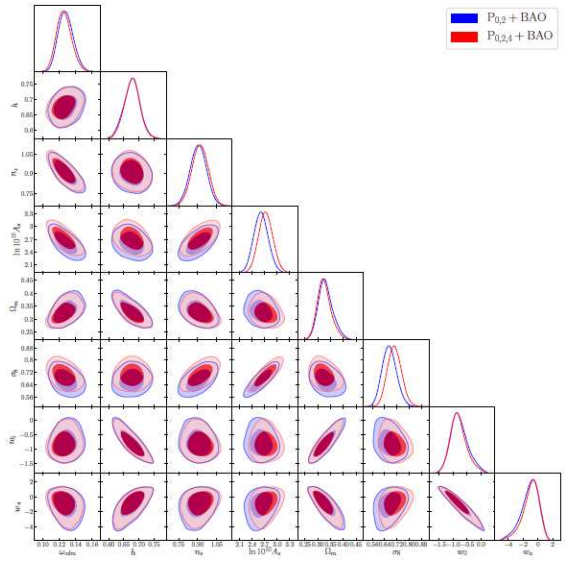

Figure 43. 1σ and 2σ confidence level contour constraints on the parameters of the spatially flat XCDM model with the inclusion of the hexadecapole ($l = 4$) moment and without it. The figure is adapted from [281].

Bernui et al. [67] investigated the effect of BAO measurements on **IDE models** that have significantly different dynamic behavior compared to the prediction of the standard ΛCDM model. The authors used the compilation of 15 transversal 2D BAO measurements [282,283] and CMB data [86] to constrain IDE models. It was found that transversal 2D BAO and traditional 3D BAO measurements can generate completely different observational constraints on the coupling parameter in IDE models. Moreover, in contrast to the joint Planck + BAO analysis, where it is not possible to solve the Hubble constant H_0 tension, the joint Planck + BAO (transversal) analysis agrees well with the measurements made by the SH0ES team and applied to the IDE models, solves the Hubble constant H_0 tension. 1σ and 2σ confidence level contours constraints on the coupling parameter ξ in IDE model using the 2D transversal 2D BAO are shown in Figure 44.

Preprints (www.preprints.org) | NOT PEER-REVIEWED | Posted: 27 October 2023 doi:10.20944/preprints202310.1818.v1

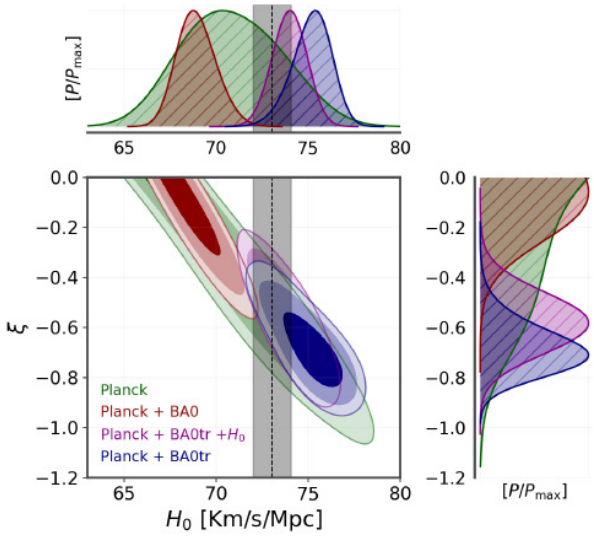

Figure 44. 1σ and 2σ confidence level 2D contours constraints on the coupling parameter ξ in the IDE model and 1D posteriors for the cases only cases without lensing. The grey vertical stripe refers to the value of H_0 measured by the SH0ES team ($H_0 = 73.04 \pm 1.04$ km s^{-1} Mpc^{-1} at 1σ confidence level). The figure is adapted from [67].

3.5. Hubble Parameter Data

Samushia & Ratra [284] used the Simon, Verde & Jimenez (SVJ) [211] definition of the redshift dependence of the Hubble parameter $H(z)$ (so-called SVJ $H(z)$ data) to constrain cosmological parameters in the **scalar field ϕCDM-RP model**. According to the results obtained (see Figure 45), using the $H(z)$ data, the constraints on the matter density parameter $\Omega_{\rm m}$ are more stringent than those on the model parameter α. Constraints on the matter density $\Omega_{\rm m}$ are approximately as tight as the ones derived from the galaxy cluster gas mass fraction data [285] and from the SNe Ia apparent magnitude data [286].

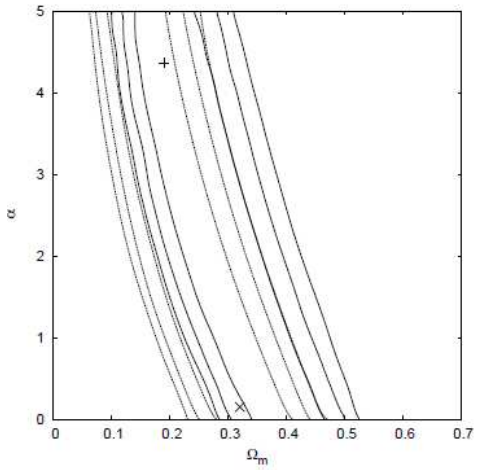

Figure 45. 1σ, 2σ and 3σ confidence level contours constraints on parameters of the ϕCDM model with the RP potential. Solid lines correspond to $H_0 = 73 \pm 3$ km s^{-1} Mpc^{-1}, while dashed lines correspond to $H_0 = 68 \pm 4$ km s^{-1} Mpc^{-1}. The cross denotes the maximum likelihood at $\Omega_{\rm m0} = 0.32$ and $\alpha = 0.15$ with reduced $\chi^2 = 1.8$. The cross denotes the maximum likelihood at $\Omega_{\rm m0} = 0.19$ and $\alpha = 4.37$ with reduced $\chi^2 = 1.89$. The horizontal axis for which $\alpha = 0$ corresponds to the spatially flat ΛCDM model. The figure is adapted from [284].

Preprints (www.preprints.org) | NOT PEER-REVIEWED | Posted: 27 October 2023 doi:10.20944/preprints202310.1818.v1

Chen & Ratra [287] analyzed constrains on the model parameters of the ϕ**CDM-RP**, the **XCDM**, and the Λ**CDM models**, using 13 Hubble parameter $H(z)$ data versus redshift [28,212]. The authors showed (see Figure 46) that the Hubble parameter $H(z)$ data yield quite strong constraints on the parameters of the ϕCDM model. The constraints derived from the $H(z)$ measurements are almost as restrictive as those implied by the currently available lookback time observations, and the GRB luminosity data, but more stringent than those based on the currently available galaxy cluster angular size data. However, they are less restrictive than those following from the joint analysis of SNe Ia apparent magnitude and BAO peak length scale data. The joint analysis of the Hubble parameter $H(z)$ data with SNe Ia apparent magnitude and BAO peak length scale data favor the standard spatially flat ΛCDM model but do not exclude the dynamical scalar field ϕCDM model.

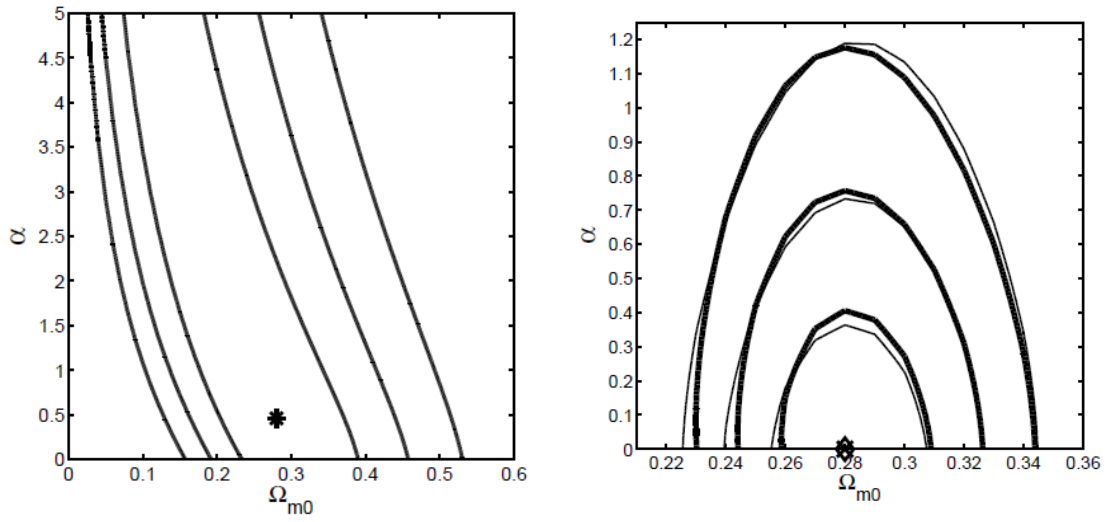

Figure 46. 1σ, 2σ and 3σ confidence level contours constraints on parameters of the ϕCDM model with the RP potential. The horizontal axis with $\alpha = 0$ corresponds to the standard spatially flat ΛCDM model. (**Left** panel) Contours obtained from $H(z)$ data. The star denotes the best-fit pair $(\Omega_{m0}, \alpha) = (0.28, 0.46)$, $\chi^2_{min} = 10.1$. (**Right** panel) Contours were obtained from a joint analysis of the BAO peak length scale and SNe Ia apparent magnitude data (with systematic errors), with (and without) $H(z)$ data. The cross denotes the best-fit point determined from the joint sample with $H(z)$ data at $\Omega_{m0} = 0.28$ and $\alpha = 0$, with $\chi^2_{min} = 531$. The diamond denotes the best-fit point obtained from the joint sample with $H(z)$ data at $\Omega_{m0} = 0.28$ and $\alpha = 0$, $\chi^2_{min} = 541$. The figure is adapted from [287].

In [288], Farooq et al. obtained constrains on the parameters of the ϕ**CDM-RP**, the **XCDM**, the w**CDM**, and the Λ**CDM models** from analysis of measurements of the BAO peak length scale, SNe Ia apparent magnitude [210], 21 Hubble parameter $H(z)$ [28,30,211,212]. The results of this analysis are shown in Figure 47. Constraints are more restrictive with the inclusion of 8 new $H(z)$ measurements [30] than those derived by Chen & Ratra [287]. This analysis favors the standard spatially flat ΛCDM model but does not exclude the scalar field ϕCDM model.

Preprints (www.preprints.org) | NOT PEER-REVIEWED | Posted: 27 October 2023 doi:10.20944/preprints202310.1818.v1

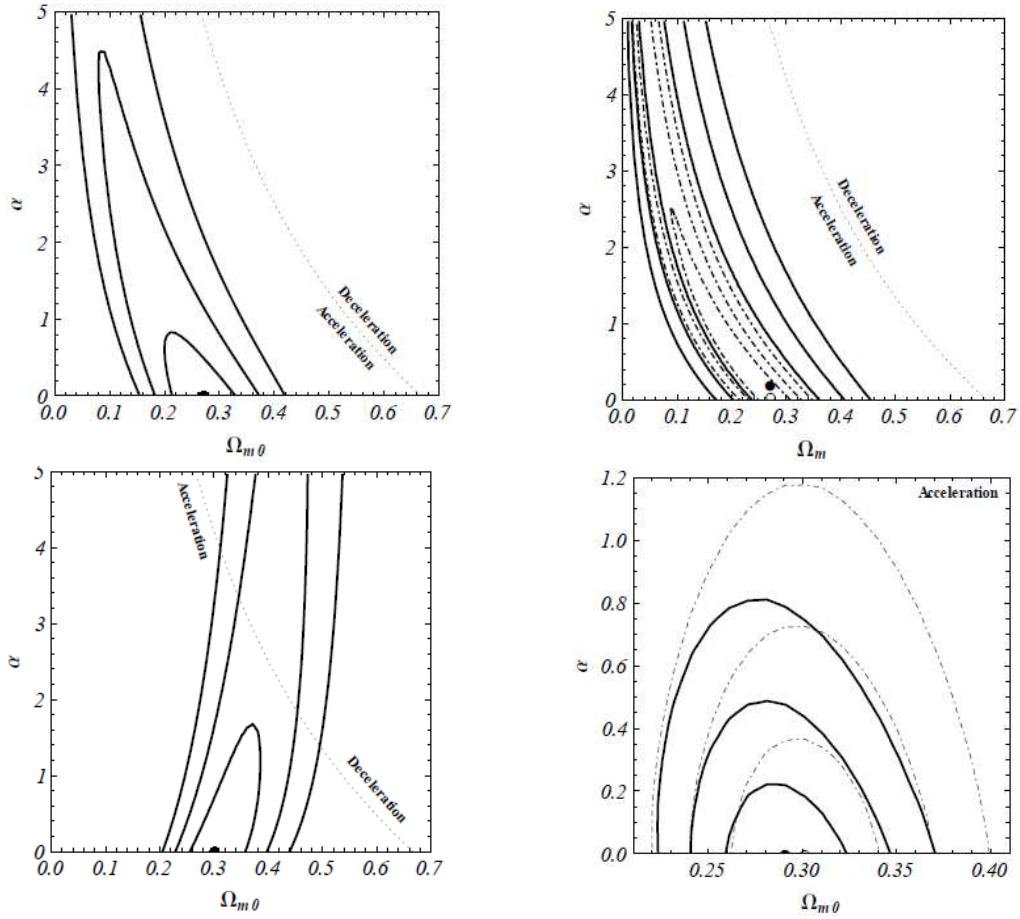

Figure 47. Thick solid lines are 1σ, 2σ and 3σ confidence level contours constraints on the parameters of the spatially flat ϕCDM model with the RP potential, for the prior $H_0 = 73.8 \pm 2.4$ km s^{-1}Mpc^{-1}. The horizontal axis with $\alpha = 0$ corresponds to the standard spatially flat ΛCDM model. (Left upper panel) Contours obtained from $H(z)$ data. Thin dot-dashed lines are 1σ, 2σ and 3σ confidence level contours reproduced from [287], where the prior is $H_0 = 68 \pm 3.5$ km s^{-1}Mpc^{-1}, the empty circle corresponds to the best-fit point. The curved dotted lines denote zero acceleration models. The filled black circles correspond to best-fit points. (Right upper panel) Contours obtained from only SNe Ia apparent magnitude data with (without) systematic errors. Filled (open) circles denote likelihood maxima for the case of data with (without) systematic errors. (Left lower panel) Contours were obtained from only the BAO peak length scale data. Filled circles denote likelihood maxima. (Right lower panel) Contours obtained from data of the BAO peak length scale and SNe Ia apparent magnitude (with systematic errors), with (without) $H(z)$ data. The full (empty) circle denotes the best-fit point determined from a joint analysis with (without) $H(z)$ data. The figure is adapted from [288].

Farooq & Ratra [289] worked out constrains on the parameters of the **ϕCDM-RP**, the **XCDM**, and the **ΛCDM models** from measurements of the Hubble parameter $H(z)$ at redshift $z = 2.3$ [290] and 21 lower redshift measurements [28,30,211,212]. Constraints with the inclusion of the new $H(z)$ measurement of Busca et al. are more restrictive than those derived by Farooq et al., Figure 48. As seen in this figure, the $H(z)$ constraints depend on the Hubble constant prior to H_0 used in the analysis. The resulting constraints are more stringent than those which follow from measurements of the SNe Ia apparent magnitude of Suzuki et al. (2012). This joint analysis consisting of measurements of $H(z)$, SNe Ia apparent magnitude, and BAO peak length scale favor the standard spatially flat ΛCDM model, but the dynamical scalar field ϕCDM model is not excluded as well.

Preprints (www.preprints.org) | NOT PEER-REVIEWED | Posted: 27 October 2023 doi:10.20944/preprints202310.1818.v1

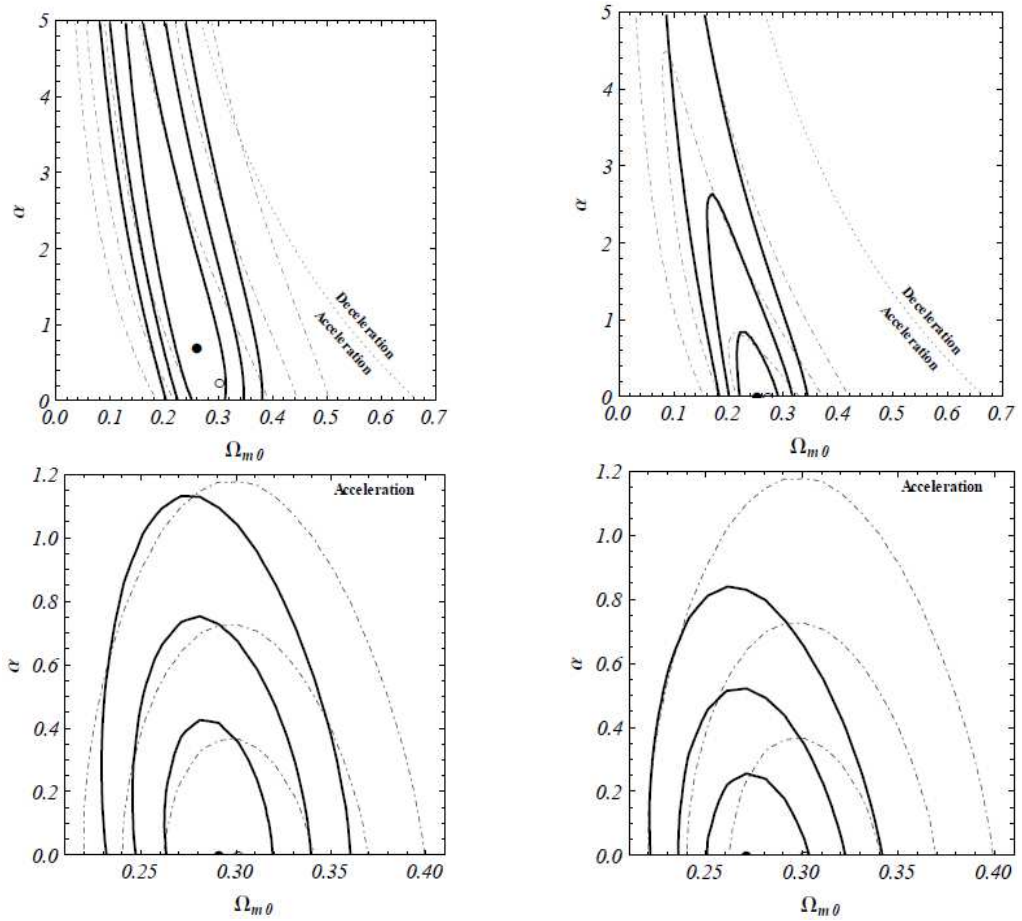

Figure 48. Thick solid (thin dot-dashed) lines are 1σ, 2σ and 3σ confidence level contours constraints on the parameters of the spatially flat ϕCDM model with the RP potential from the new $H(z)$ data (old $H(z)$ data were used in [288]). The filled (empty) circle is the best-fit point from new (old) $H(z)$ measurements. The horizontal axis with $\alpha = 0$ corresponds to the standard spatially flat ΛCDM model. The curved dotted lines denote zero acceleration models. (Left upper panel) Contours obtained for the $H_0 = 68 \pm 3.5$ kms^{-1}Mpc^{-1} prior. The filled circles correspond to the best-fit pair $(\Omega_{\rm m0}, \alpha) = (0.36, 0.70)$, $\chi^2_{\rm min} = 15.2$. The empty circles correspond to the best-fit pair $(\Omega_{\rm m0}, \alpha) = (0.30, 0.25)$, $\chi^2_{\rm min} = 14.6$. (Right upper panel) Contours obtained for the $H_0 = 73.8 \pm 2.4$ kms^{-1}Mpc^{-1} prior. The filled circles correspond to the best-fit pair $(\Omega_{\rm m0}, \alpha) = (0.25, 0)$, $\chi^2_{\rm min} = 16.1$. Empty circles correspond to the best-fit pair $(\Omega_{\rm m0}, \alpha) = (0.27, 0)$, $\chi^2_{\rm min} = 15.6$. (Left lower panel) Contours obtained from joint analysis with SNe Ia apparent magnitude data (with systematic errors), BAO peak length scale data, with (without) $H(z)$ data. The full (empty) circle marks the best-fit point determined from a joint analysis with (without) $H(z)$ data. Contours obtained for $H_0 = 68 \pm 3.5$ kms^{-1}Mpc^{-1} prior. The full circle indicates the best-fit pair $(\Omega_{\rm m0}, \alpha) = (0.29, 0)$, $\chi^2_{\rm min} = 567$ while the empty circle corresponds to the best-fit pair $(\Omega_{\rm m0}, \alpha) = (0.30, 0)$, $\chi^2_{\rm min} = 551$. (Right lower panel) Contours obtained for the $H_0 = 73.8 \pm 2.4$ kms^{-1}Mpc^{-1} prior. The empty circle denotes the best-fit pair $(\Omega_{\rm m0}, \alpha) = (0.30, 0)$, $\chi^2_{\rm min} = 551$ while the full circle denotes the best-fit pair $(\Omega_{\rm m0}, \alpha) = (0.27, 0)$, $\chi^2_{\rm min} = 569$. The figure is adapted from [289].

Farooq & Ratra [291] found constraints on the parameters of the **ϕCDM-RP model** from the compilation of 28 independent measurements of the Hubble parameter $H(z)$ within the range of redshift $0.07 \leq z \leq 2.3$. Measurements of $H(z)$ require a currently accelerating cosmological expansion at 3σ confidence level. The authors determined the deceleration-acceleration transition redshift $z_{\rm da} = 0.74 \pm 0.05$. This result is in good agreement with the result obtained by Busca et al. [290], which is $z_{\rm da} = 0.82 \pm 0.08$ based on 11 measurements of $H(z)$ from BAO peak length scale data within the

Preprints (www.preprints.org) | NOT PEER-REVIEWED | Posted: 27 October 2023 doi:10.20944/preprints202310.1818.v1

range of redshift $0.2 \leq z \leq 2.3$. The resulting constraints with different priors of H_0 are demonstrated in Figure 49.

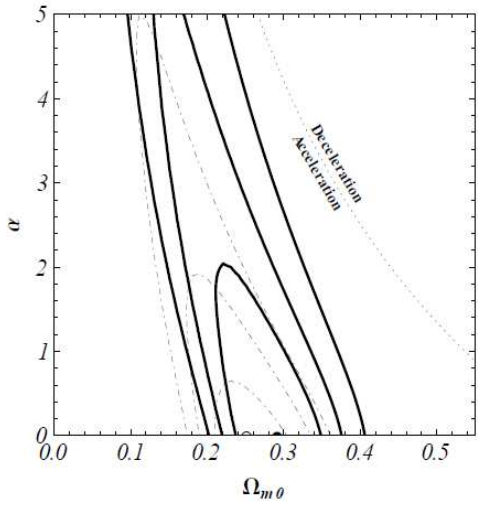

Figure 49. Thick solid and thin dot-dashed lines are 1σ, 2σ and 3σ confidence level contours constraints on the parameters of the scalar field ϕCDM model with the RP potential from the compilation of $H(z)$ data for $H_0 = 68 \pm 3.5$ km s^{-1}Mpc^{-1} and $H_0 = 73.8 \pm 2.4$ km s^{-1}Mpc^{-1} priors, respectively. The horizontal axis with $\alpha = 0$ corresponds to the standard spatially flat ΛCDM model, and the curved dotted line denotes zero acceleration models. Filled and empty circles are best-fit points for which $(\Omega_{\rm m0}, \alpha) = (0.29, 0)$, $\chi^2_{\rm min} = 18.24$ and $(\Omega_{\rm m0}, \alpha) = (0.25, 0)$, $\chi^2_{\rm min} = 20.64$, respectively. The figure is adapted from [291].

Farooq et al. [214] analyzed constraints on the parameters of the **spatially flat ϕCDM-RP**, the **XCDM**, and the **ΛCDM models** from a compilation of measurements of the Hubble parameter $H(z)$. To get this compilation, the authors used weighted mean and median statistics techniques to combine 23 independent lower redshifts $z < 1.04$, Hubble parameter $H(z)$ measurements, and define binned forms of them. Then this compilation was combined with 5 $H(z)$ measurements at the higher redshifts $1.3 \leq z \leq 2.3$. The resulting constraints are shown in Figure 50. As seen from the figure, the weighted mean binned data are almost identical to those derived from analysis using 28 independent measurements of $H(z)$. Binned weighted-mean values of $H(z)/(1+z)$ versus redshift data are presented in Figure 51. These results are consistent with a moment of the deceleration-acceleration transition at redshift $z_{da} = 0.74 \pm 0.05$ derived by Farooq & Ratra [291], which corresponds to the standard spatially flat ΛCDM model.

Preprints (www.preprints.org) | NOT PEER-REVIEWED | Posted: 27 October 2023 doi:10.20944/preprints202310.1818.v1

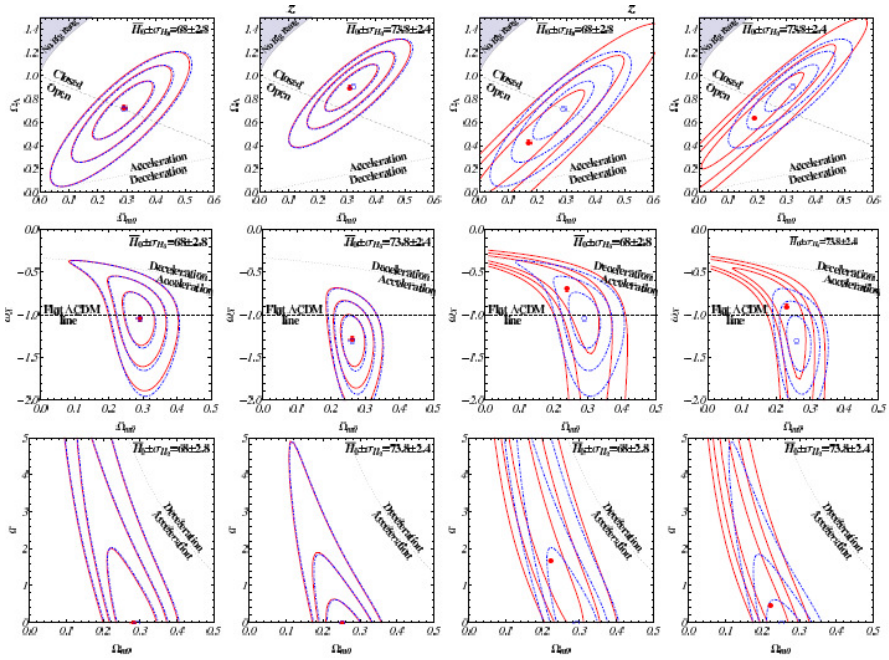

Figure 50. Thick solid and thin dot-dashed lines are 1σ, 2σ and 3σ confidence level contours constraints on the parameters of the ϕCDM model with the RP potential, the XCDM model, and the ΛCDM model from 7 or 9 measurements per bin data. In these three rows, the first two plots include red weighted-mean constraints while the second two include red median statistics. Filled red and empty blue circles correspond to the best-fit points. Dashed diagonal lines denote spatially flat models, and dotted lines show zero acceleration models. The figure is adapted from [214].

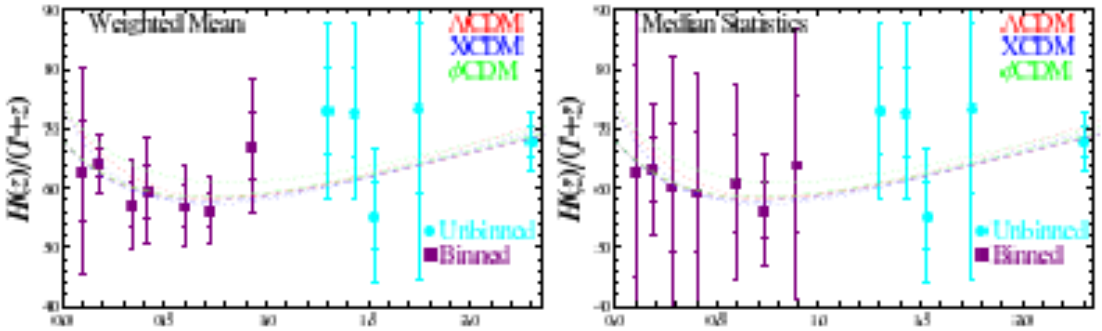

Figure 51. The $H(z)/(1+z)$ data binned with 7 or 9 measurements per bin, as well as 5 higher measurements of redshift, and Farooq & Ratra [291] best-fit model predictions. Dashed and dotted lines correspond to $H_0 = 68 \pm 3.5$ km s^{-1}Mpc^{-1} and $H_0 = 73.8 \pm 2.4$ km s^{-1}Mpc^{-1} priors, respectively. The figure is adapted from [214].

Chen et al. [292] used 28 measurements of Hubble parameter $H(z)$ within the redshift range $0.07 \leq z \leq 2.3$ [21,28,30,31,211,290,293] to define the value of the Hubble constant H_0 in the **ϕCDM-RP**, the **wCDM**, and **the spatially flat and spatially non-flat ΛCDM models**. The result obtained for the ϕCDM-RP model is shown in Figure 52. The value of the Hubble constant H_0 is found as: for the spatially flat and spatially non-flat ΛCDM model, $H_0 = 68.3^{+2.7}_{-3.3}$ km s^{-1}Mpc^{-1} and $H_0 = 68.4^{+2.9}_{-3.3}$ km s^{-1}Mpc^{-1}; for the wCDM model, $H_0 = 65.0^{+6.5}_{-6.6}$ km s^{-1}Mpc^{-1}; for the ϕCDM model, $H_0 = 67.9^{+2.4}_{-2.4}$ km s^{-1}Mpc^{-1} (at 1σ confidence level). The obtained H_0 values are more consistent with the smaller values determined from the recent CMB temperature anisotropy and BAO peak length

Preprints (www.preprints.org) | NOT PEER-REVIEWED | Posted: 27 October 2023 doi:10.20944/preprints202310.1818.v1

scale data and with the values derived from the median statistics analysis of Huchra's compilation of H_0 data.

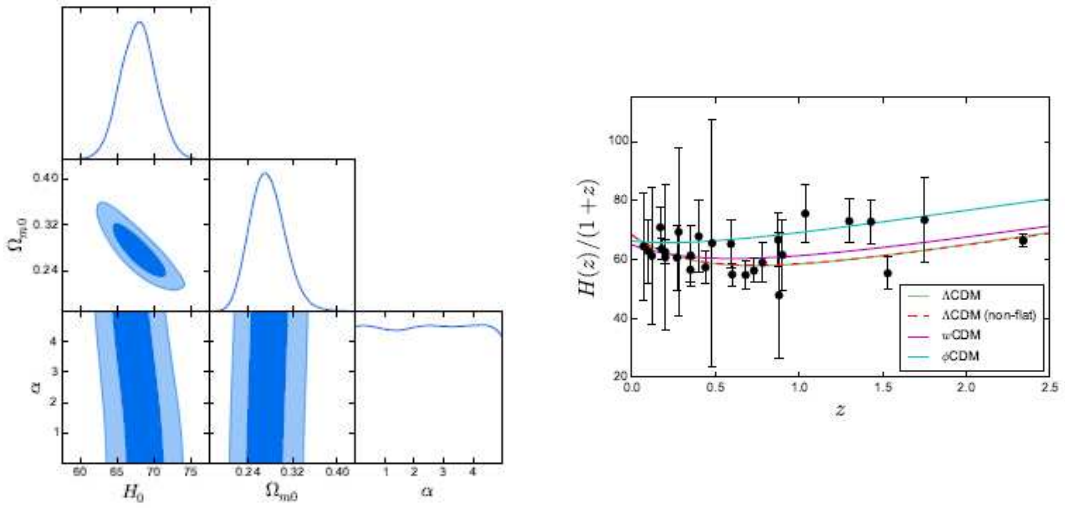

Figure 52. (**Left** panel) 1σ and 2σ confidence level contours constraints on the parameters of the ϕCDM model with the RP potential. (**Right** panel) Best-fit model curves from the 28 $H(z)$ data points for the spatially flat ϕCDM model, wCDM model, and the spatially flat and spatially non-flat ΛCDM model. The figure is adapted from [292].

Farooq et al. [142] determined constraints on the parameters of the **ϕCDM-RP**, the **XCDM**, the **wCDM**, and the **ΛCDM models** in the spatially **flat** and spatially **non-flat** universe. The authors used the updated compilation of 38 measurements of the Hubble parameter $H(z)$ within the redshift range $0.07 \leq z \leq 2.36$ [21,25,28,30–34,211,248]. The result for these constraints is shown in Figure 53. The authors determined the redshift of the cosmological deceleration-acceleration transition, $z_{\rm da}$, and the value of the Hubble constant H_0 from the $H(z)$ measurements. The determined values of $z_{\rm da}$ are insensitive to the chosen model, and depend only on the assumed value of the Hubble constant H_0. The weighted mean of these measurements is $z_{\rm da} = 0.72 \pm 0.05$ (0.84 ± 0.03) for $H_0 = 68 \pm 2.8$ (73.24 ± 1.74) km s^{-1}Mpc^{-1}. The authors proposed a model-independent method to determine the value of the Hubble constant H_0. The $H(z)$ data are consistent with the standard spatially flat ΛCDM model while do not rule out the spatially non-flat XCDM and spatially non-flat ϕCDM models.

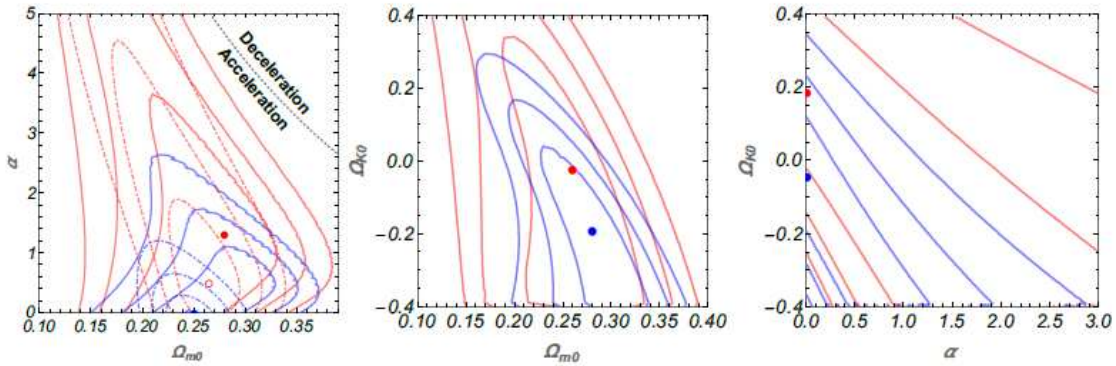

Figure 53. 1σ, 2σ and 3σ confidence level contours constraints on the parameters of the spatially non-flat ϕCDM model with the RP potential. Red (blue) solid lines are for the lower (higher) H_0 prior. (**Left**, **center**, and **right** panels) The results obtained correspond to the marginalization over $\Omega_{\rm k0}$, α and $\Omega_{\rm m0}$, respectively. Red (blue) solid circles are the best-fit points for the lower (higher) H_0 prior. Red (blue) dot-dashed lines in the left panel are 1σ, 2σ and 3σ for the lower (higher) H_0 prior in the spatially flat ϕCDM model. The figure is adapted from [142].

Preprints (www.preprints.org) | NOT PEER-REVIEWED | Posted: 27 October 2023 doi:10.20944/preprints202310.1818.v1

3.6. Quasar Angular Size Data

Ryan et al. [143] determined constraints on the parameters of the **spatially flat and spatially non-flat ΛCDM**, **XCDM**, **ϕCDM-RP models** using BAO peak length scale measurements [22,24–26,248], the Hubble parameter $H(z)$ data [21,30–34,211], and quasar (QSO) angular size data [294,295]. 1σ, 2σ and 3σ confidence level contours constraints on the parameters of the spatially non-flat ϕCDM model with the RP potential from $H(z)$, QSO and BAO peak length scale datasets are presented in Figure 54. Depending on the chosen model and dataset, the observational data slightly favor both the spatially closed hypersurfaces with $\Omega_{k0} < 0$ at 1.7σ confidence level, and the dynamical dark energy models over the standard spatially flat ΛCDM model at a slightly higher than 2σ confidence level. Furthermore, depending on the dataset and the model, the observational data favor a lower Hubble constant value than the one measured by the local data at 1.8σ confidence level to 3.4σ confidence level.

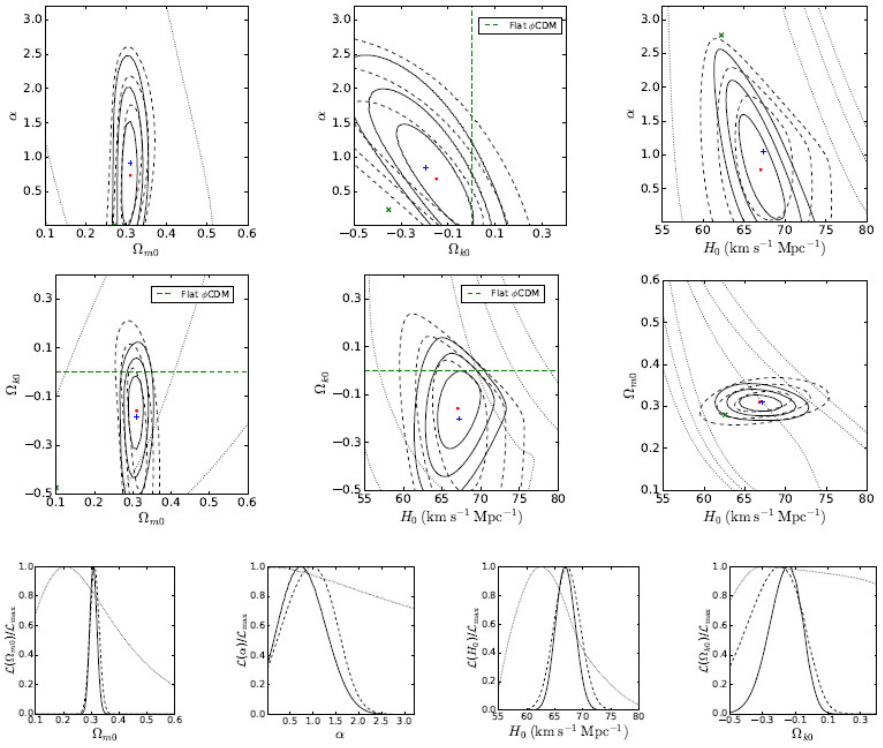

Figure 54. 1σ, 2σ and 3σ confidence level contours constraints on the parameters of the spatially non-flat ϕCDM model with the RP potential from data of $H(z)$, QSO and BAO peak length scale. (**Upper** and **middle** panels) The vertical green dashed line in the upper center panel, the horizontal green dashed lines in the middle left and middle center panels separate spatially closed models (with $\Omega_{k0} < 0$) from spatially open models (with $\Omega_{k0} > 0$). The horizontal line with $\alpha = 0$ in the upper panels corresponds to the spatially non-flat ΛCDM model. (**Lower** panel) One-dimensional likelihoods for $\Omega_{m0}, \alpha, H_0, \Omega_{k0}$. The figure is adapted from [143].

Cao et al. [296] found constraints on the parameters of the **spatially flat** and **non-flat ΛCDM**, **XCDM**, and **ϕCDM-RP models** using H_{II} starburst galaxy apparent magnitude measurements [297,298], the compilation of 1598 X-ray and UV flux measurements of QSO 2015 data within the redshift range $0.036 \leq z \leq 5.1003$ and 2019 QSO data [299,300] only and in conjunction with BAO peak length scale measurements [22,24–26,248], Hubble parameter $H(z)$ data [21,28,30–34,211]. The constraints on the parameters of the spatially flat and spatially non-flat ϕCDM model with the RP potential obtained from datasets mentioned above are shown in Figure 55. A combined analysis of all datasets leads to the relatively model-independent and restrictive estimates for the values of matter

Preprints (www.preprints.org) | NOT PEER-REVIEWED | Posted: 27 October 2023 doi:10.20944/preprints202310.1818.v1

density parameter at present epoch Ω_{m0} and the Hubble constant H_0. Depending on the cosmological model, these estimates are consistent with a lower value of H_0 in the range of 2.0σ to 3.4σ confidence level. Combined datasets favor the spatially flat ΛCDM, while at the same time do not rule out dynamical dark energy models.

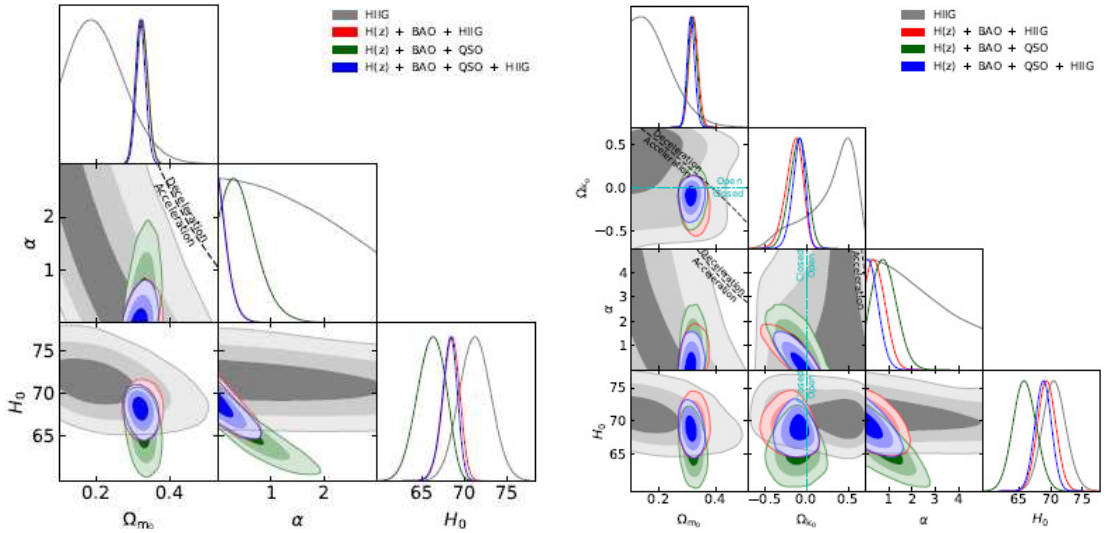

Figure 55. 1σ, 2σ and 3σ confidence level contours constraints on the parameters of the spatially flat ϕCDM model with the RP potential (**Left** panel). The black dotted line splits the parameter space into accelerated and decelerated regions. The axis with $\alpha = 0$ denotes the spatially flat ΛCDM model. Constraints for the spatially non-flat ϕCDM model with the RP potential are depicted in the right panel. The figure is adapted from [296].

The compilation of 1598 X-ray and UV flux measurements of QSO 2015 data within the redshift range $0.036 \leq z \leq 5.1003$ and 2019 QSO data [299,300] only and in conjunction with BAO peak length scale measurements [22,24–26,248], Hubble parameter $H(z)$ data[21,28,30–34,211] was applied by Khadka & Ratra [145] to impose constraints on the parameters of the **tilted spatially flat** and **untilted spatially non-flat ΛCDM**, **XCDM**, and **ϕCDM-RP quintessential inflation models**. Obtained constraints for the untilted spatially non-flat ϕCDM-RP model from the combination of various datasets and extended QSO data only are presented in Figure 56. In most of the models, the QSO data favor the values of the matter density parameter $\Omega_{m0} \sim 0.5 - 0.6$, while in a combined analysis of QSO data with $H(z)$ + BAO peak length scale dataset, the values of the matter density parameter at present epoch Ω_{m0} are shifted slightly towards larger values. A combined set of data QSO + BAO peak length scale + $H(z)$ is consistent with the standard spatially flat ΛCDM model, but favors slightly both the spatially closed hypersurfaces and the dynamical dark energy models.

Preprints (www.preprints.org) | NOT PEER-REVIEWED | Posted: 27 October 2023 doi:10.20944/preprints202310.1818.v1

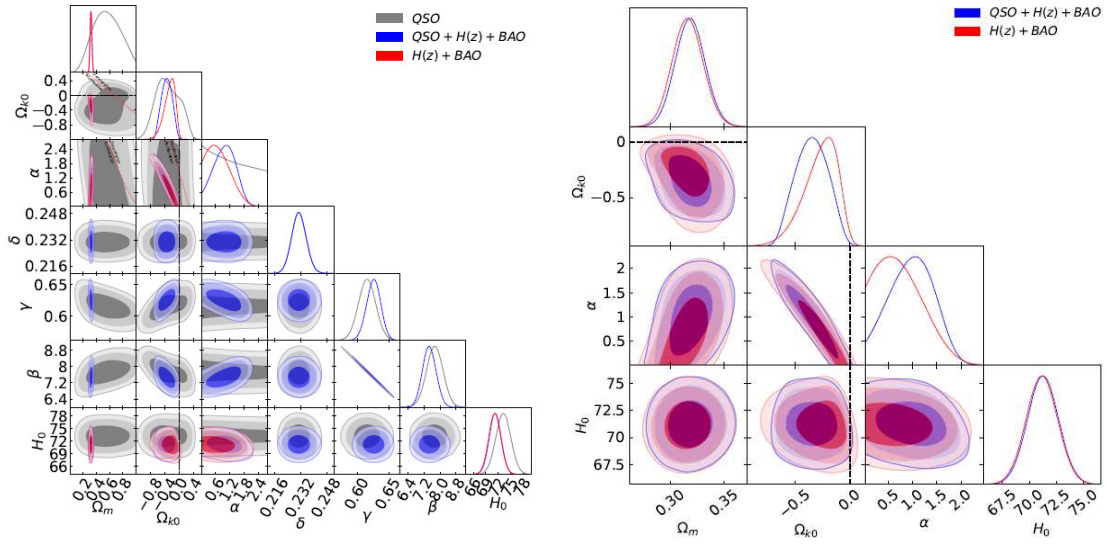

Figure 56. 1σ, 2σ and 3σ confidence level contours constraints on the parameters of the untilted spatially non-flat ϕCDM model with RP potential using the combination of datasets: QSO (grey line), $H(z)$ + BAO peak length scale (red line), and QSO + $H(z)$ + BAO peak length scale (blue line). (**Left** panel) Contours and one-dimensional likelihoods for all free parameters. The red dotted curved lines denote zero acceleration lines. (**Right** panel) Plots for $\Omega_{\rm m0}, \Omega_{\rm k0}, \alpha, H_0$ cosmological parameters, without constraints from QSO data. These plots are for $H_0 = 73.24 \pm 1.74$ km s^{-1}Mpc^{-1} as a prior. The black dashed straight lines denote the flat hypersurface with $\Omega_{\rm k0} = 0$. The figure is adapted from [145].

Khadka & Ratra [146] obtained constraints on the parameters of the **tilted spatially flat** and **untilted spatially non-flat ΛCDM**, **XCDM**, **ϕCDM-RP quintessential inflation models** from a compilation of 808 X-ray and UV flux measurements of QSOs (quasi-stellar objects) within the redshift range $0.061 \leq z \leq 6.28$ alone [299] and in conjunction with BAO peak length scale measurements [22,24–26,248], Hubble parameter $H(z)$ data [21,28,30–34,211]. 1σ, 2σ and 3σ confidence level contours constraints on the parameters of the untilted spatially non-flat ϕCDM model with the RP potential from the combination of various datasets are presented in Figure 57. The constraints using only the QSO data are significantly weaker but consistent with those from the combination of the $H(z)$ + BAO peak length scale data. Combined analysis from QSO + $H(z)$ + BAO peak length scale data is consistent with the standard spatially flat ΛCDM model but slightly favors both closed spatial hypersurfaces and the untilted spatially non-flat ϕCDM model.

Preprints (www.preprints.org) | NOT PEER-REVIEWED | Posted: 27 October 2023 doi:10.20944/preprints202310.1818.v1

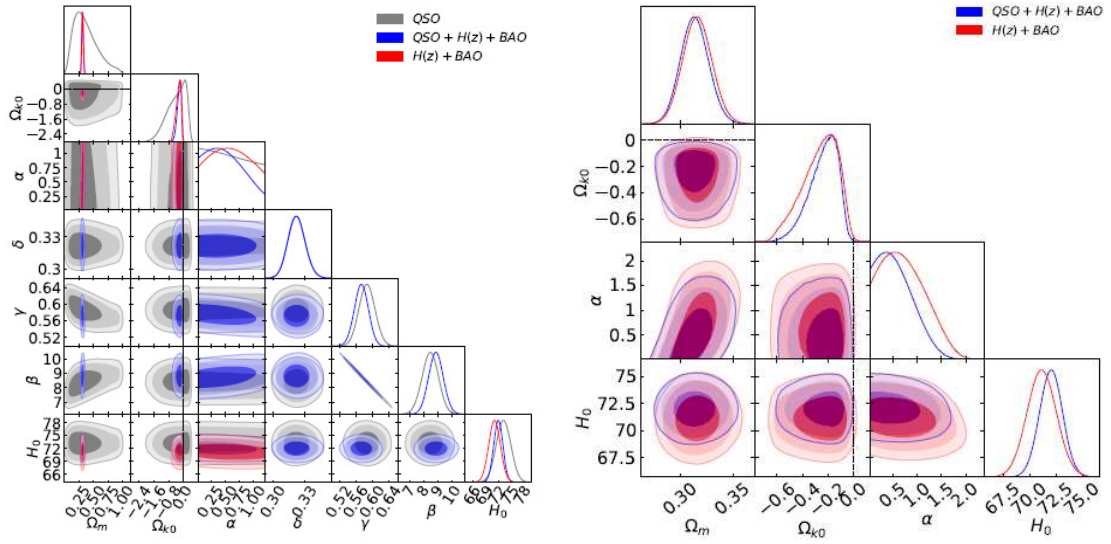

Figure 57. 1σ, 2σ and 3σ confidence level contours constraints on the parameters of the untilted spatially non-flat ϕCDM model with the RP potential using the combination of datasets: QSO (grey line), $H(z)$ + BAO peak length scale (red line), and QSO + $H(z)$ + BAO peak length scale (blue line). (**Left** panel) Contours and one-dimensional likelihoods for all free parameters. (**Right** panel) Plots for only $\Omega_{\rm m0}, \Omega_{\rm k0}, \alpha, H_0$ cosmological parameters, without constraints only from QSO data. These plots are for $H_0 = 73.24 \pm 1.74$) km s^{-1}Mpc^{-1} as a prior. Black dashed straight lines denote the spatially flat hypersurface with $\Omega_{\rm k0} = 0$. The figure is adapted from [146].

Cao et al. [301] found constraints on the parameters of the **spatially flat** and **non-flat** Λ**CDM**, **XCDM**, and ϕ**CDM-RP models** using the higher-redshift GRB data [302,303], starburst galaxy (H_{II}G) measurements [297,298,304], and QSO angular size (QSO-AS) data [294,295]. Constraints from the combined analysis of cosmological parameters of the spatially flat and non-flat ϕCDM-RP model are presented in Figure 58. The constraints from the combined analysis of these datasets are consistent with the currently accelerating cosmological expansion, as well as with the constraints obtained from the analysis of the Hubble parameter $H(z)$ data and the measurements of the BAO peak length scale. From the analysis of the $H(z)$ + BAO peak length scale + QSO-AS + H_{II}G + GRB dataset, the model-independent values of the matter density parameter at present epoch $\Omega_{\rm m0} = 0.313 \pm 0.013$ and the Hubble constant $H_0 = 69.3 \pm 1.2$ km s^{-1}Mpc^{-1} are obtained. This analysis favors the spatially flat ΛCDM model but also does not rule out dynamical dark energy models.

Preprints (www.preprints.org) | NOT PEER-REVIEWED | Posted: 27 October 2023 doi:10.20944/preprints202310.1818.v1

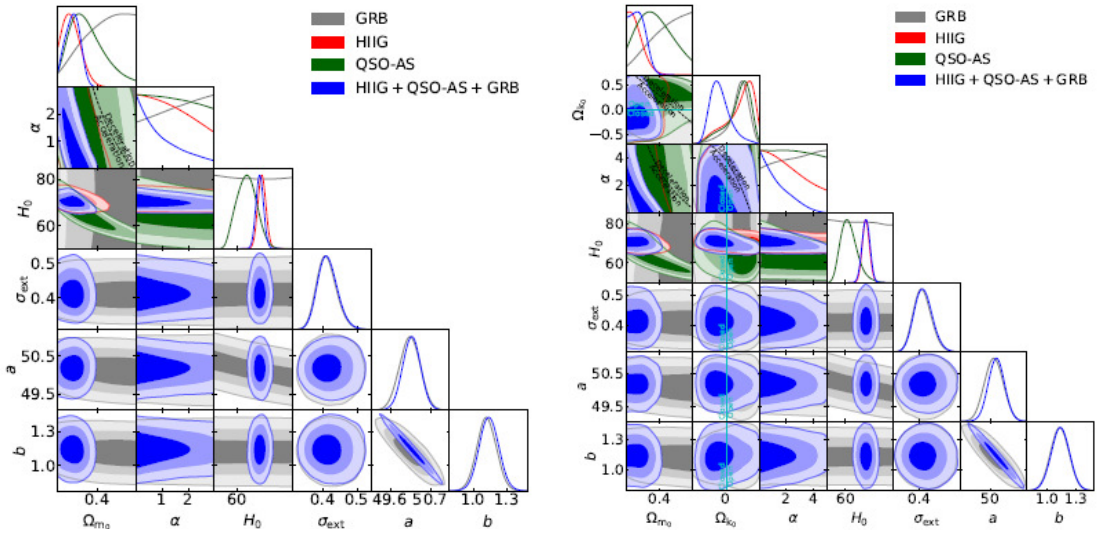

Figure 58. 1σ, 2σ and 3σ confidence level contours constraints on the parameters of the spatially flat (**Left** panel) and spatially non-flat (**Right** panel) ϕCDM models with the RP potential from various datasets. The black dotted line splits the parameter space into the regions of the currently decelerating and accelerating cosmological expansion. The axis with $\alpha = 0$ denotes the spatially flat ΛCDM model. The figure is adapted from [301].

Khadka & Ratra [147] determined constraints on the parameters of the **spatially flat** and **non-flat** Λ**CDM**, **XCDM**, and ϕ**CDM-RP models** from the compilation of X-ray and UV flux measurements of 2038 QSOs which span the redshift range $0.009 \leq z \leq 7.5413$ [300,305]. The obtained results are shown in Figure 59. The authors found that for the full QSO dataset, parameters of the X-ray and UV luminosities $L_X - L_{UV}$ relation used to standardize these QSO data depends on the cosmological model, and therefore cannot be used to constrain the cosmological parameters in these models. Subsets of these QSOs, limited by redshift $z \leq 1.5 - 1.7$, obey the $L_X - L_{UV}$ relation in a way that is independent of the cosmological model and can therefore be used to constrain the cosmological parameters. Constraints from these smaller subsets of lower redshift QSO data are generally consistent, but much weaker than those inferred from the Hubble parameter $H(z)$ and the BAO peak length scale measurements.

Preprints (www.preprints.org) | NOT PEER-REVIEWED | Posted: 27 October 2023 doi:10.20944/preprints202310.1818.v1

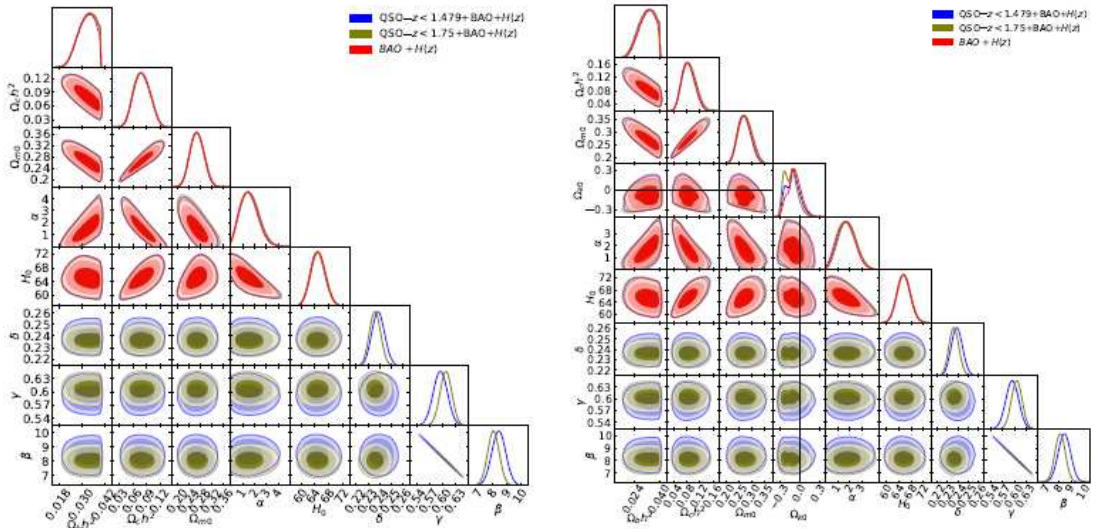

Figure 59. 1σ, 2σ and 3σ confidence level contours constraints on the parameters of the spatially flat (**Left** panel) and spatially non-flat (**Right** panel) ϕCDM models with the RP potential, using QSO ($z < 1.497$) + BAO peak length scale + $H(z)$ (blue), QSO ($z < 1.75$) + BAO peak length scale + $H(z)$ (olive), BAO peak length scale + $H(z)$ (red) datasets for all free parameters. In the Ω_{k0} subpanels of the right panel, black dotted straight lines correspond to $\Omega_{k0} = 0$. The axis with $\alpha = 0$ denotes the spatially flat ΛCDM model. The figure is adapted from [147].

Cao et al. [151] determined constraints on the parameters of the **spatially flat** and **non-flat ΛCDM**, **XCDM**, and **ϕCDM-RP models** by analyzing total of 1383 measurements consisting of 1048 Pantheon SNe Ia apparent magnitude measurements of Scolnic et al. (2018) [163], and 20 binned SNe Ia apparent magnitude measurements of DES Collaboration [306,307], 120 QSO measurements [299,300,305], 153 H_{II}G data [297,298,304], 11 BAO peak length scale measurements [22,24–26,248], 31 Hubble parameter $H(z)$ data [21,28,30–34,211]. Constraints on the parameters of the spatially non-flat ϕCDM model with the RP potential from that analysis of the data are shown in Figure 60. From the analysis of those datasets, the model-independent estimates of the Hubble constant, $H_0 = 68.8 \pm 1.8$ km s^{-1}Mpc^{-1}, as well as the matter density parameter at the present epoch, $\Omega_{m0} = 0.294 \pm 0.020$ are obtained. While the constraints favor dynamical dark energy and slightly spatially closed hypersurfaces, they do not preclude dark energy from being a cosmological constant and spatially flat hypersurfaces.

Preprints (www.preprints.org) | NOT PEER-REVIEWED | Posted: 27 October 2023 doi:10.20944/preprints202310.1818.v1

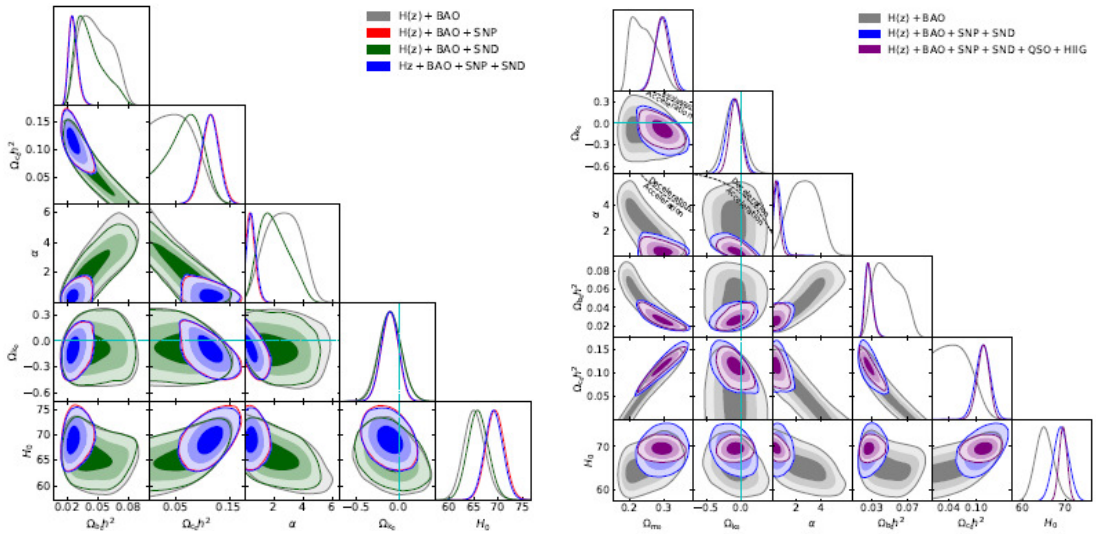

Figure 60. 1σ, 2σ and 3σ confidence level contours constraints on the parameters of the spatially non-flat ϕCDM model with the RP potential. The zero-acceleration line splits the parameter space into regions of the currently decelerating and accelerating cosmological expansion. The cyan dash-dot lines show the spatially flat ϕCDM model, regions with spatially closed geometry are located either below or to the left. The axis with $\alpha = 0$ denotes the spatially flat ΛCDM model. The figure is adapted from [151].

Khadka & Ratra [148] found constraints on the parameters of the **spatially flat** and **non-flat** Λ**CDM**, **XCDM**, and ϕ**CDM-RP models** from 78 reverberation-measured $MgII$ time-lag QSOs within the redshifs range $0.0033 \leq z \leq 1.89$ [308,309]. The authors applied the radius-luminosity or $R - L$ relation to standardized 78 $MgII$ QSOs data. In each model, the authors simultaneously determined the $R - L$ relation and parameters in these models, thus avoiding the problem of circularity. It was found that values of the $R - L$ relation parameter are independent of the model used in the analysis, which makes it possible to establish that current $MgII$ QSOs data are standardizable candles. Constraints on parameters of the spatially flat and non-flat ϕCDM-RP models, using $MgII$ QSO-78 and BAO peak length scale + $H(z)$ data, are shown in Figure 61. Constraints derived from the QSO data only are significantly weaker than those derived from the combined set of the BAO peak length scale and the Hubble parameter $H(z)$ measurements but are consistent with both of them. The constraints obtained from the $MgII$ QSOs data in conjunction with the BAO peak length scale + $H(z)$ measurements agree with the spatially flat ΛCDM model as well as with spatially non-flat dynamical dark energy models.

Preprints (www.preprints.org) | NOT PEER-REVIEWED | Posted: 27 October 2023 doi:10.20944/preprints202310.1818.v1

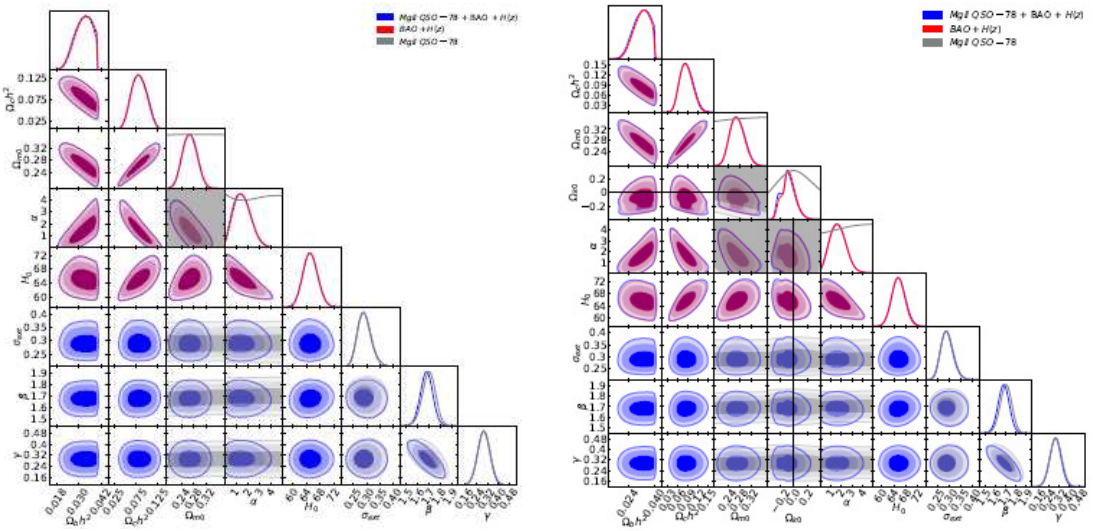

Figure 61. 1σ, 2σ and 3σ confidence level contours constraints on the parameters of the spatially flat (**Left** panel) and spatially non-flat (**Right** panel) ϕCDM models with the RP potential from Mg_{II} QSO-78 (gray), BAO peak length scale + $H(z)$ (red), and Mg_{II} QSO-78 + BAO peak length scale + $H(z)$ (blue) measurements. In Ω_{k0} subpanels of the right panel, black dashed straight lines correspond to $\Omega_{k0} = 0$. The axis with $\alpha = 0$ denotes the spatially flat ΛCDM model. The figure is adapted from [148].

Khadka & Ratra [149] found that the recent compilation of the QSO X-ray and UV flux measurements [305] includes the QSO data that appear to be not standardized via the X-ray luminosity and the UV luminosity $L_X - L_{UV}$ relation parameters that are dependent on both the cosmological model and the redshift, so it should not be used to constrain the model parameters. These data include a compilation of seven different subsamples. The authors analyzed these subgroups, and some combinations of subgroups to define which QSO subgroups are responsible for questions specified in the paper of Khadka & Ratra [147]. They considered that the largest of the seven sub-samples in this compilation, SDSS-4XMM QSOs, which contribute about 2/3 of all QSOs have the $L_X - L_{UV}$ ratios that depend on both the accepted cosmological model and the redshift, and thus are the source of a similar problem found earlier when collecting the full QSO data.

The second and third largest subsamples, SDSS-Chandra and XXL QSOs, which together account for about 30% of total QSO data, appear to be standardized. Constraints on the cosmological parameters from these subsamples are weak and consistent with the standard spatially flat ΛCDM model or with the constraints from the better-established cosmological probes. Constraints on the cosmological parameters of the spatially flat and spatially non-flat ϕCDM models with the RP potential, using SDSS-Chandra, XXL QSO data as well as $H(z)$ data, BAO peak length scale data are presented in Figure 62.

Preprints (www.preprints.org) | NOT PEER-REVIEWED | Posted: 27 October 2023 doi:10.20944/preprints202310.1818.v1

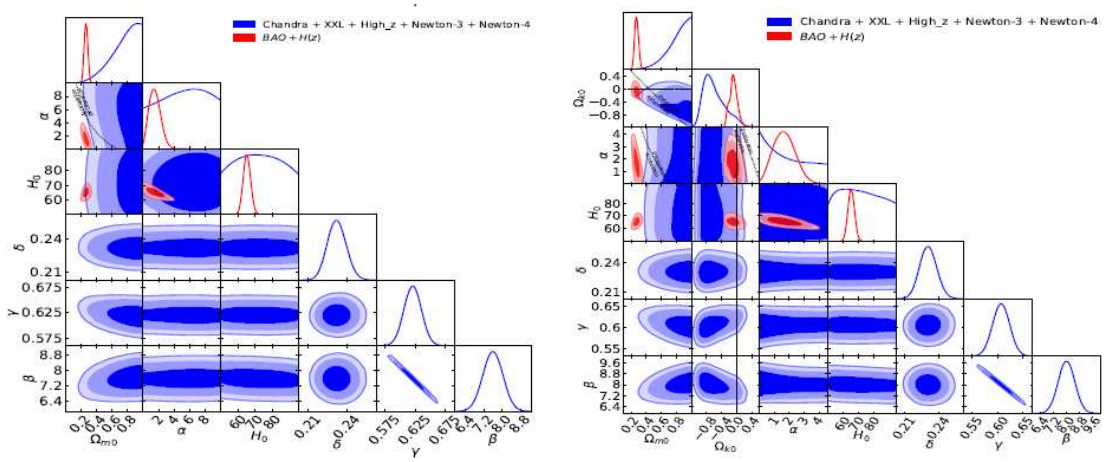

Figure 62. 1σ, 2σ and 3σ confidence level contours constraints on the parameters of the spatially flat (**Left** panel) and spatially non-flat (**Right** panel) ϕCDM models with the RP potential, using Chandra + XXL + High-z + Newton-3 + Newton-4 (blue) and BAO peak length scale + $H(z)$ (red) datasets. In all plots, black dotted lines are zero acceleration lines, which split the parameter space into the regions of current acceleration and deceleration. Black dashed line corresponds to $\Omega_{k0} = 0$. The axis with $\alpha = 0$ denotes the spatially flat ΛCDM model. The figure is adapted from [149].

Khadka et al. [150] used 118 $H\beta$ QSO measurements [310] within the redshift range $0.0023 \leq z \leq 0.89$ to simultaneously constrain cosmological model parameters and QSO 2-parameter radius-luminosity $R - L$ relation parameters of the **spatially flat** and **non-flat** Λ**CDM**, **XCDM**, and ϕ**CDM-RP models**. The authors found that the $R - L$ relation parameters for $H\beta$ QSOs data are independent in models under investigation, therefore QSO data seem to be standardizable through $R - L$ relation parameters. The constraints derived using $H\beta$ QSO data are weak, slightly favoring the currently accelerating cosmological expansion, and are generally in the 2σ tension with the constraints derived from analysis of the measurements of the BAO peak length scale and the Hubble parameter $H(z)$. Constraints on the cosmological parameters of the spatially flat and non-flat ϕCDM-RP model, from the $H\beta$ QSO measurements, the $H(z)$ and BAO peak length scale data are presented in Figure 63.

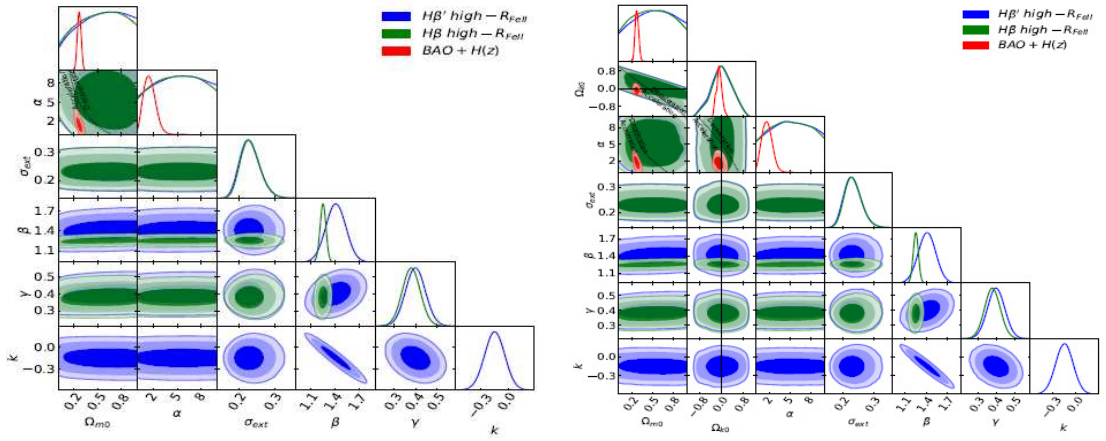

Figure 63. 1σ, 2σ and 3σ confidence level contours constraints on the parameters of the spatially flat (**Left** panel) and spatially non-flat (**Right** panel) ϕCDM model with the RP potential from 3-parameter $H\beta'$ high-$\Re_{FeII}$ (blue), 2-parameter $H\beta'$ high-$\Re_{FeII}$ (green), and $H(z)$ + BAO peak length scale (red) measurements. Black dotted lines correspond to zero acceleration lines. Black dashed lines represent $\Omega_{k0} = 0$. The figure is adapted from [150].

Khadka et al. [311] determined constraints on the parameters of the **spatially flat** and **spatially non-flat** Λ**CDM**, **XCDM**, and ϕ**CDM-RP models** using the observations of 66 reverberation-measured

Preprints (www.preprints.org) | NOT PEER-REVIEWED | Posted: 27 October 2023 doi:10.20944/preprints202310.1818.v1

Mg_{II} QSOs within the redshift range $0.36 \leq z \leq 1.686$. Constraints on the cosmological parameters of the spatially flat and spatially non-flat ϕCDM models with the RP potential from various QSO datasets are shown in Figure 64. The authors also studied the two- and three-parameter radius-luminosity $R-L$ relations [312,313] for Mg_{II} QSO sources, and found that these relations do not depend on the assumed cosmological model, therefore they can be used to standardize QSO data. The authors found for the two-parameter $R-L$ relation that the data subsets with low-$\Re_{FeII}$ and high-$\Re_{FeII}$ obey the same $R-L$ relation within the error bars. Extending the two-parameter $R-L$ relation to three parameters does not lead to the expected decrease in the intrinsic variance of the $R-L$ relation. None of the three-parameter $R-L$ relations provides a significantly better measurement fit than the two-parameter $R-L$ relation. The results obtained differ significantly from those found by Khadka et al. [150] from analysis of reverberation-measured $H\beta$ QSOs.

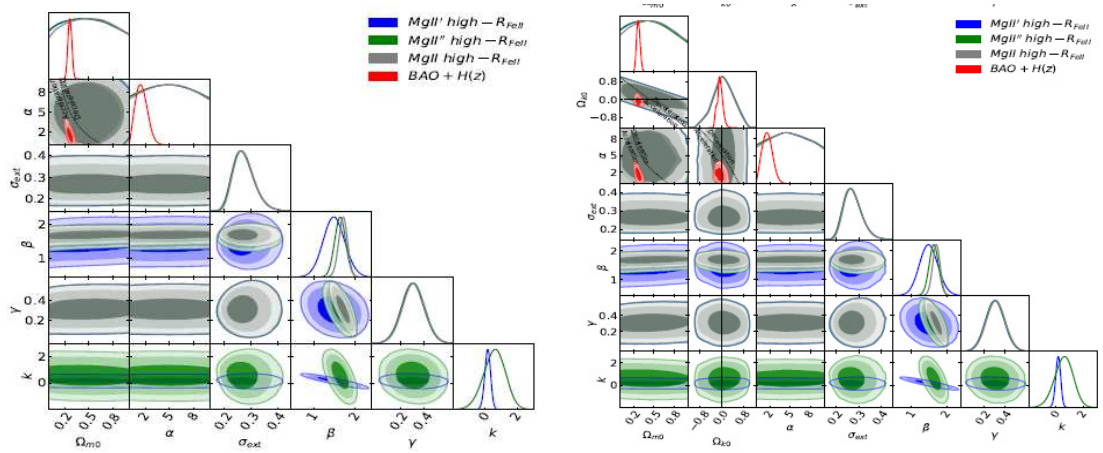

Figure 64. 1σ, 2σ and 3σ confidence level contours constraints on the parameters of the spatially flat (**Left** panel) and spatially non-flat (**Right** panel) ϕCDM models with the RP potential from the measurements of $Mg_{II'}$ high-$\Re_{FeII}$ (blue), MgII'' high-$\Re_{FeII}$ (green), Mg_{II} high-$\Re_{FeII}$ (gray), and BAO peak length scale + $H(z)$. Black dotted lines correspond to zero acceleration lines. Black dashed lines represent $\Omega_{k0} = 0$. The figure is adapted from [311].

Cao et al. [153] determined constraints on the parameters of the **spatially flat** and **non-flat** Λ**CDM**, **XCDM**, ϕ**CDM-RP models**, as well as on the QSO radius-luminosity $R-L$ relation parameters from the 38 C_{IV} QSO reverberation-measured data in the redshift range $0.001064 \leq z \leq 3.368$. An improved method is used that takes into account more accurately the asymmetric error bars for the time-delay measurements. The authors found that the parameters of the $R-L$ relation do not depend on the cosmological models considered, and therefore, the $R-L$ relation can be used to standardize the C_{IV} QSO data. Mutually consistent constraints on the cosmological parameters from C_{IV}, Mg_{II} and $H(z)$ + BAO peak length scale data allow conducting the analysis from C_{IV} + Mg_{II} dataset as well as from the $H(z)$ + BAO peak length scale + C_{IV} + Mg_{II} datasets. Although the C_{IV} + Mg_{II} cosmological constraints are weak, they slightly (at $\sim 0.1\sigma$ confidence level) change the constraints from the $H(z)$ + BAO peak length scale + C_{IV} + Mg_{II} datasets. The constraints on the cosmological parameters of the spatially flat and non-flat ϕCDM-RP from various QSO datasets are shown in Figure 65.

Preprints (www.preprints.org) | NOT PEER-REVIEWED | Posted: 27 October 2023 doi:10.20944/preprints202310.1818.v1

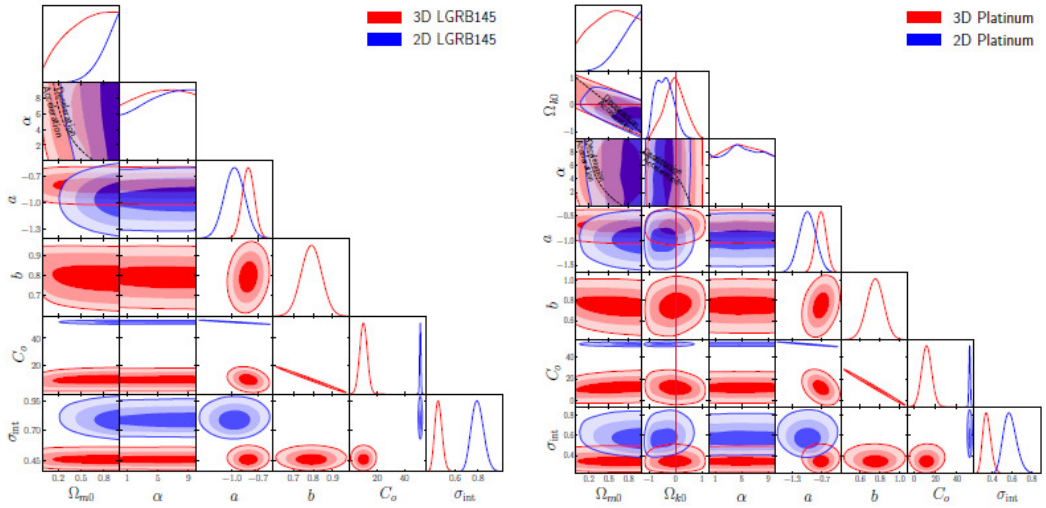

Figure 65. 1σ, 2σ and 3σ confidence level contours constraints on the parameters of the spatially flat (**Left** panel) and spatially non-flat (**Right** panel) ϕCDM models with the RP potential from various combinations of datasets. The axis with $\alpha = 0$ denotes the spatially flat ΛCDM model. The black dash-dotted lines denote spatially flat hypersurfaces $\Omega_{k0} = 0$, closed spatial hypersurfaces are located either below or to the left. The black dotted lines correspond to the lines of zero acceleration and split the parameter space into currently accelerating (bottom left) and decelerating (top right) regions. The figure is adapted from [153].

3.7. Gamma Ray Burst Distances Data

Samushia & Ratra [314] derived constraints on the parameters of the **spatially flat ΛCDM**, **XCDM**, and **ϕCDM-RP models** using the observational datasets of SNe Ia Union apparent magnitude data [315], BAO peak length scale data [17], measurements of gamma-ray burst (GRB) distances [316,317]. The authors applied two methods for analyzing the GRB data fitting luminosity relation of GRB, Wang's method [317] and Schaefer's method [316]. The constraints on the cosmological parameters of the ϕCDM model from analysis of the SNe Ia Union apparent magnitude data and the BAO peak length scale measurements, with and without the GRB measurements are presented in Figure 66. The constraints from the GRB data obtained by two different methods disagree with each other at more than 2σ confidence level. The cosmological parameters of the ϕCDM model could not be tightly constrained only by the current GRB data.

Preprints (www.preprints.org) | NOT PEER-REVIEWED | Posted: 27 October 2023 doi:10.20944/preprints202310.1818.v1

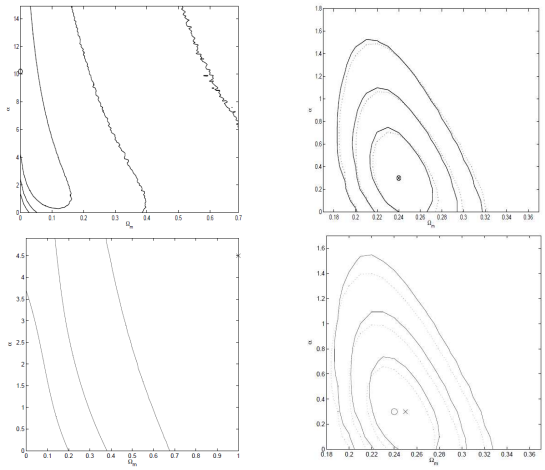

Figure 66. 1σ, 2σ and 3σ confidence level contours constraints on parameters of the ϕCDM model with the RP potential. The horizontal axis with $\alpha = 0$ corresponds to the standard spatially flat ΛCDM model. (Left upper panel) Contours are obtained by Wang's (2008) method. The circle indicates the best-fit parameter values $\Omega_{\rm m} = 0$, $\alpha = 10.2$ with $\chi^2 = 1.39$ for 4 degrees of freedom. (Right upper panel) Contours are derived using the GRB data by Wang's (2008) method, the SNe Ia Union apparent magnitude data, and the BAO peak length scale measurements, while dotted lines (here the cross denotes the best-fit point) are derived using only the SNe Ia apparent magnitude data and the BAO peak length scale measurements. The best fit parameters in both cases are: $\Omega_{\rm m} = 0.24$, $\alpha = 0.3$ with $\chi^2 = 326$ for 313 degrees of freedom (solid lines) and $\chi^2 = 321$ for 307 degrees of freedom. (Left lower panel) Contours are obtained using GRB data by Schaefer's (2007) method (here the cross indicates the best-fit parameter values): $\Omega_{\rm m} = 1$, $\alpha = 4.5$ with $\chi^2 = 77.8$ for 67 degrees of freedom. (Right lower panel) Contours are obtained using the data by Schaefer's (2007) method, the SNe Ia Union apparent magnitude data, and the BAO peak length scale measurements, while dotted lines are obtained using the SNe Ia apparent magnitude data and the BAO peak length scale measurements only. Here the cross denotes the best-fit point. The best-fit matter density parameters are $\Omega_{\rm m} = 0.24$, $\alpha = 0.30$ with $\chi^2 = 401$ for 376 degrees of freedom (solid lines), and $\Omega_{\rm m} = 0.25$, $\alpha = 0.3$ with $\chi^2 = 321$ for 307 degrees of freedom (dotted lines). The figure is adapted from [314].

Khadka & Ratra [318] performed an analysis of constraints on the parameters of the **spatially flat** and **non-flat ΛCDM**, **XCDM**, and **ϕCDM-RP models** from measurements of the peak photon energy and bolometric fluence of 119 GRBs extending over the redshift range of $0.34 \leq z \leq 8.2$ [302,303], and Amati relation parameters [319], BAO peak length scale measurements [22,24–26,248], Hubble parameter $H(z)$ data [21,28,30–34,211]. Resulting constraints on the parameters of the spatially flat and spatially non-flat ϕCDM model with the RP potential are presented in Figure 67.

The Amati relation between the peak photon energy of the GRB in the cosmological rest frame, E_p and $E_{\rm iso}$ is given as

$$\log(E_{\rm iso}) = a + b\log(E_p), \tag{52}$$

where a and b are free parameters defined from data, representing points of intersection and slope in the Amati relation, respectively. E_p and $E_{\rm iso}$ are specified as

$$E_{\rm iso} = \frac{4\pi D_{\rm L}^2(z,p) S_{\rm bolo}}{(1+z)}, \quad E_p = E_{p,{\rm obs}}(1+z), \tag{53}$$

where $D_{\rm L}(z,p)$ is the luminosity distance, p is a cosmological parameter, $S_{\rm bolo}$ is the measured bolometric fluence, $E_{p,{\rm obs}}$ is the measured peak energy of the GRB.

The resulting Amati relation parameters are almost identical in all considered cosmological models, which confirms the use of the Amati relation parameters to standardize these GRBs data. The constraints on the cosmological parameters of the models under consideration from the GRB data

Preprints (www.preprints.org) | NOT PEER-REVIEWED | Posted: 27 October 2023 doi:10.20944/preprints202310.1818.v1

are consistent with the constraints obtained from the analysis of the BAO peak length scale and the measurements of the Hubble parameter $H(z)$ but are less restrictive.

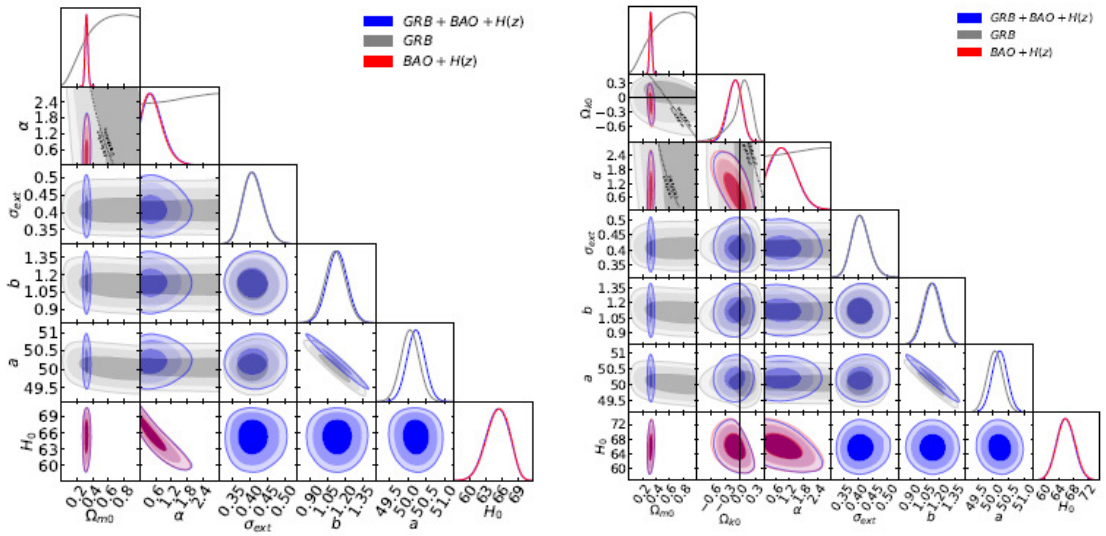

Figure 67. 1σ, 2σ and 3σ confidence level contours constraints on the parameters of the spatially flat (**Left** panel) and spatially non-flat (**Right** panel) ϕCDM models with the RP potential, using the combination of datasets: GRB (grey line), $H(z)$ + BAO peak length scale (red line), and GRB + $H(z)$ + BAO peak length scale (blue line). The black dotted line splits the parameter space into accelerating and decelerating regions. The axis with $\alpha = 0$ denotes the spatially flat ΛCDM model. The figure is adapted from [318].

Khadka et al. [320] analyzed constraints on the parameters of the **spatially flat** and **non-flat ΛCDM**, **XCDM**, and **ϕCDM-RP models** from the GRB data. The authors considered eight different GRB datasets to test whether the current GRB measurements, which probe a largely unexplored range of cosmological redshifts, can be used to reliably constrain the parameters of these models. The authors applied the MCMC analysis implemented in Monte Python to find the most appropriate correlations and cosmological parameters for the eight GRB samples, with and without the BAO peak length scale and the $H(z)$ data.

They applied three Amati correlation samples [319] and five Combo correlation samples [321] to obtain correlations and constraints on the model parameters. Constraints on the parameters of the **spatially non-flat ϕCDM-RP model**, using various datasets of GRB, as well as the BAO peak length scale + $H(z)$ data, are shown in Figure 68. The authors found that the cosmological constraints, determined from the A118 sample consisting of 118 bursts, agree but are much weaker than those following from the BAO peak length scale and the $H(z)$ data. These constraints are consistent with the spatially-flat ΛCDM as well as with the spatially non-flat dynamical dark energy models.

Preprints (www.preprints.org) | NOT PEER-REVIEWED | Posted: 27 October 2023 doi:10.20944/preprints202310.1818.v1

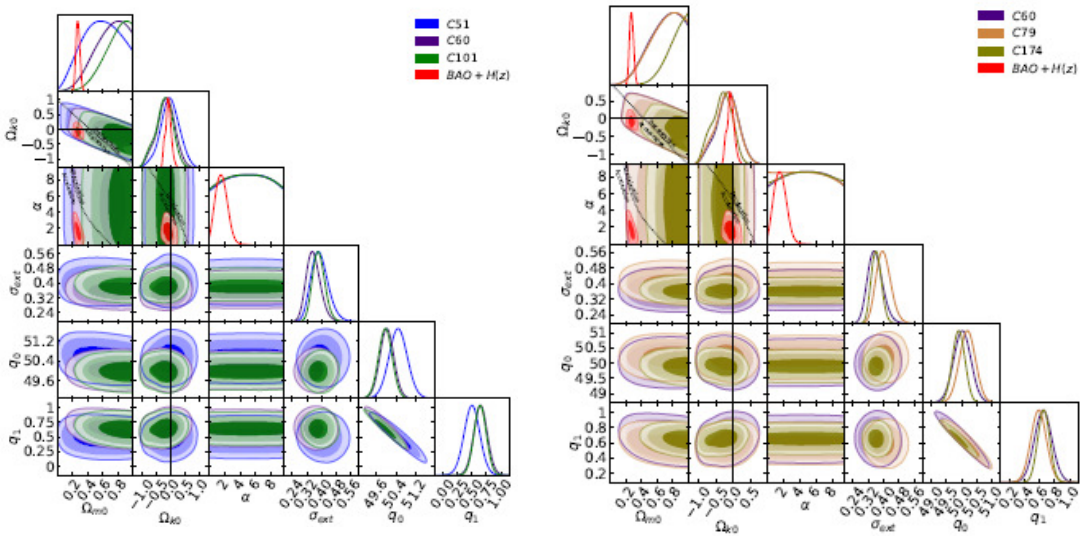

Figure 68. 1σ, 2σ and 3σ confidence level contours constraints on the parameters of the spatially non-flat ϕCDM model with the RP potential, using various GRB datasets and the BAO peak length scale + $H(z)$ datasets. The black dotted line in the $\alpha - \Omega_{\mathrm{m0}}$ subpanels is the line of the zero acceleration, under which the accelerated cosmological expansion occurs. The axis with $\alpha = 0$ denotes the spatially flat ΛCDM model. The figure is adapted from [147].

Cao et al. [152] applied the **spatially flat** and **non-flat** Λ**CDM**, **XCDM**, and ϕ**CDM-RP models** in the analysis of the three (ML, MS, and GL) ($L_0 - t_b$) Dianotti-correlated sets of GRB measurements collected by Wang et al. [322] and Hu et al. [323] that together explore the redshift range $0.35 \leq z \leq 5.91$. The authors found that each dataset, as well as the combinations of MS + GL, ML + GL, and ML + MS, obey the cosmological model-independent Dainotti correlations [324–326]) and therefore are standardized. The luminosity of the plateau phase for GRBs that obey the Dainotti correlation is defined as

$$L_0 = \frac{4\pi D_L^2 F_0}{(1+z)}^{1-\beta'}, \tag{54}$$

here F_0 is the GRB X-ray flux, β' is the spectral index in the plateau phase, and D_L is the luminosity distance.

The authors applied these GRB data in combination with the best currently available Amati-correlated GRB data of Amati [319] that explore the redshift range $0.3399 \leq z \leq 8.2$ to constrain the cosmological model parameters. As a result, constraints are weak, providing lower bounds on the matter density parameter at present epoch Ω_{m0}, moderately favoring the non-zero spatial curvature, and largely consistent with both the currently accelerated cosmological expansion and with constraints determined on the basis of more reliable data. Constraints of cosmological parameters of the **spatially flat** and **non-flat** ϕ**CDM-RP model**, using the Dianotti-correlated sets of the GRB measurements as well as the $H(z)$ and BAO peak length scale data are presented in Figure 69.

Preprints (www.preprints.org) | NOT PEER-REVIEWED | Posted: 27 October 2023 doi:10.20944/preprints202310.1818.v1

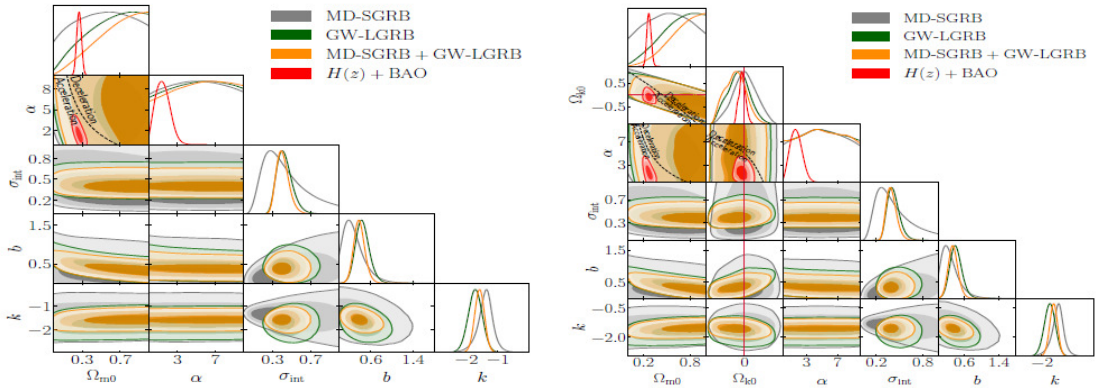

Figure 69. 1σ, 2σ and 3σ confidence level contours constraints on the parameters of the spatially flat (**Left** panel) and spatially non-flat (**Right** panel) ϕCDM models with the RP potential from MD-SGRB (gray), GWLGRB (green), MD-SGRB + GW-LGRB (orange), and $H(z)$ + BAO peak length scale (red) data. Black dashed lines denote zero-acceleration lines, which split the parameter space into two regions of current acceleration and deceleration. Dash-dotted crimson lines correspond to spatially flat hypersurfaces with spatially closed hypersurfaces either below or to the left. The magenta lines correspond to the ϕCDM model, the closed spatial geometry are either below or to the left. The axis with $\alpha = 0$ denotes the spatially flat ΛCDM model. The figure is adapted from [152].

Cao et al. [154] used the **spatially flat** and **non-flat** Λ**CDM**, **XCDM**, and ϕ**CDM-RP models** to analyze compilation of data from 50 Platinum GRB within the redshift range $0.553 \leq z \leq 5.0$. The authors found that these data obey the three-parameter fundamental plane or Dainotti correlation, independent of the cosmological model, and therefore they are amenable to standardization and can be used to constrain cosmological parameters. To improve the accuracy of the constraints for the GRBs data only, the authors excluded ordinary GRB data from the larger Amati-correlated A118 dataset of 118 GRBs and analyzed the remaining 101 Amati-correlated GRBs with 50 Platinum GRB datasets. This joint dataset of 151 GRBs is being investigated within the little-studied redshift range $z \in (2.3, 8.2)$. Due to the consistency of cosmological constraints from the platinum GRB data with the $H(z)$ + BAO peak length scale dataset, the authors combined platinum GRB and the $H(z)$ + BAO peak length scale data to carry out the analysis and found small changes in the cosmological parameter constraints compared to the constraints from the $H(z)$ + BAO peak length scale data. The resulting constraints from the GRBs only are more stringent than those from the $H(z)$ + BAO peak length scale dataset but are less precise. The constraints on the cosmological parameters of the spatially flat and spatially non-flat ϕCDM model with the RP potential, using platinum GRB measurements along with the $H(z)$ and BAO peak length scale data are presented in Figure 70.

Preprints (www.preprints.org) | NOT PEER-REVIEWED | Posted: 27 October 2023 doi:10.20944/preprints202310.1818.v1

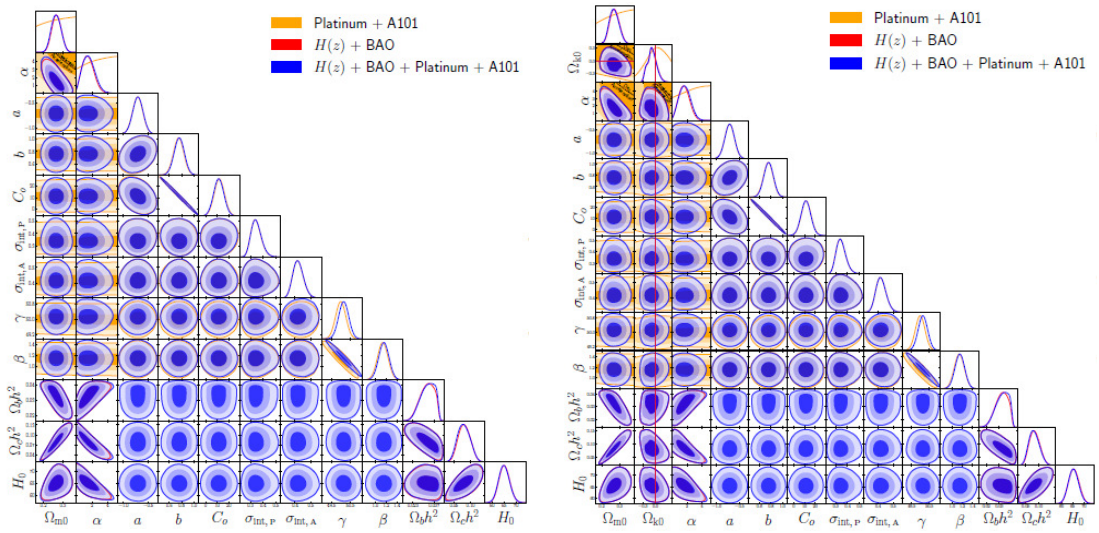

Figure 70. 1σ, 2σ and 3σ confidence level contours constraints on the parameters of the spatially flat (**Left** panel) and spatially non-flat (**Right** panel) ϕCDM models with the RP potential, using various combinations of datasets. The axis with $\alpha = 0$ denotes the spatially flat ΛCDM model. The black dotted lines correspond to lines of zero acceleration and split the parameter space into currently accelerating (bottom left) and currently decelerating (top right) regions of the cosmological expansion. The crimson dash-dot lines denote spatially flat hypersurfaces $\Omega_{k0} = 0$, spatially closed hypersurfaces are located either below or to the left. The figure is adapted from [154].

Cao et al. [155] proposed the constraints on the parameters of the **spatially flat** and **non-flat** Λ**CDM**, **XCDM**, and ϕ**CDM-RP models**, using the extended set of the GRB data including the 50 platinum GRBs within the redshift range $0.553 \leq z \leq 5$ by Dainotti et al. [327], the LGRB95 data that contains 95 long GRBs measurements within the redshift range $0.297 \leq z \leq 9.4$ by Dainotti et al. [327]. The compilation of the 145 GRB data sets was also used. The constraints on the cosmological parameters of the spatially flat and spatially non-flat ϕCDM model with the RP potential, using various GRB datasets are shown in Figure 71. The authors also examined which of two correlations, the two-dimensional Dainotti correlation [328] or the three-dimensional Dainotti correlation [329,330], fits better the GRB datasets. Based on the results of AIC, BIC, and Deviation Information Criterion (DIC) analysis, the authors found that the three-dimensional Danotti correlation is much more preferable than the two-dimensional one for the GRB datasets.

Preprints (www.preprints.org) | NOT PEER-REVIEWED | Posted: 27 October 2023 doi:10.20944/preprints202310.1818.v1

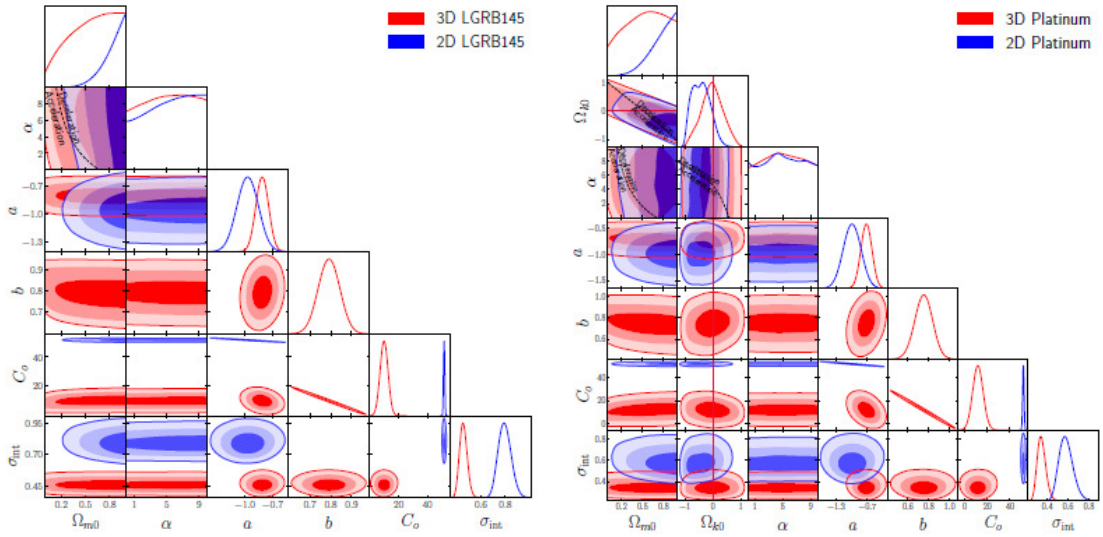

Figure 71. 1σ, 2σ and 3σ confidence level contours on parameters of the spatially flat (**Left** panel) and spatially non-flat (**Right** panel) ϕCDM models with the RP potential, using various combinations of GRB datasets. The axis with $\alpha = 0$ denotes the spatially flat ΛCDM model. The black dotted lines correspond to lines of zero acceleration and split the parameter space into currently accelerating (bottom left) and currently decelerating (top right) regions. The crimson dash-dot lines denote spatially flat hypersurfaces $\Omega_{k0} = 0$, closed spatial hypersurfaces are located either below or to the left. The figure is adapted from [155].

3.8. Starburst Galaxy Data

Mania & Ratra [331] analyzed constraints on the parameters of the **ϕCDM-RP**, the **XCDM**, and **the ΛCDM models** from the H_{II} starburst galaxy apparent magnitude versus redshift data of Siegel et al. [332]. The authors followed the Percival et al. [213] procedure to obtain these constraints. The results are demonstrated in Figure 72. These constraints are largely consistent but not as restrictive as those derived from the measurements of the BAO peak length scale, the SNe Ia apparent magnitude, and the CMB temperature anisotropy.

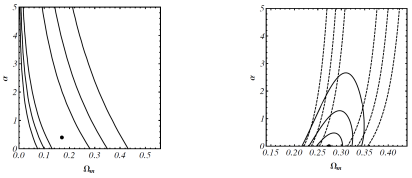

Figure 72. 1σ, 2σ and 3σ confidence level contours constraints on the parameters of the spatially flat ϕCDM model with the RP potential. The horizontal axis with $\alpha = 0$ corresponds to the standard spatially flat ΛCDM model. (**Left** panel) Contours obtained from H_{II} galaxy data. The best-fit point with $\chi^2_{\rm min} = 53.3$ is indicated by the solid black circle at $\Omega_{\rm m0} = 0.17$ and $\alpha = 0.39$. (**Right** panel) Contours obtained from joint H_{II} galaxy and BAO peak length scale data (solid lines) and BAO peak length scale data only (dashed lines). The best-fit point with $-2\log(L_{\rm max}) = 55.6$ is indicated by the solid black circle at $\Omega_{\rm m0} = 0.27$ and $\alpha = 0$. The figure is adapted from [331].

Cao et al. [333] derived constraints on the parameters of the **spatially flat** and **non-flat ΛCDM**, **XCDM**, and **ϕCDM-RP models** from the compilation of the H_{II} starburst galaxy (H_{II}G) data of González-Morán et al. [304] and the H_{II}G data of González-Morán et al. [334]. The authors tested the model independence of the QSO angular size measurements. They found that the new compilation of 2019 H_{II}G data provides tighter constraints and favors lower values of the cosmological parameters than those from the 2019 H_{II}G data. The use of QSO measurements gives model-independent constraints on the characteristic linear size l_m of QSO within a sample. Analysis of the data of the $H(z)$,

Preprints (www.preprints.org) | NOT PEER-REVIEWED | Posted: 27 October 2023 doi:10.20944/preprints202310.1818.v1

BAO peak length scale, the SNe Ia apparent magnitude-Pantheon, the SNe Ia apparent magnitude-DES, QSO, and the latest compilation of the H_{II}G data provides almost model-independent estimates of the Hubble constant, the matter density parameter at the present epoch, and the characteristic linear size, respectively, as $H_0 = 69.7 \pm 1.2$ km s^{-1}Mpc^{-1}, $\Omega_{\rm m0} = 0.295 \pm 0.021$, and $l_m = 10.93 \pm 0.25$ pc. Constraints on the parameters of the spatially non-flat ϕCDM model with RP potential from various combinations of the H_{II}G, QSO, BAO peak length scale, and the $H(z)$ datasets, are shown in Figure 73.

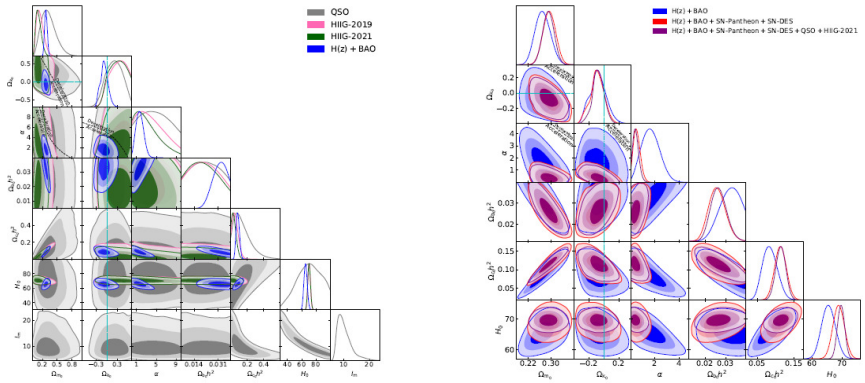

Figure 73. 1σ, 2σ and 3σ confidence level contours constraints on the parameters of the spatially non-flat ϕCDM model with the RP potential from various datasets. The cyan dash-dot lines correspond to the ϕCDM model, the closed spatial geometry are either below or to the left. The axis with $\alpha = 0$ denotes the spatially flat ΛCDM model. The figure is adapted from [333].

Cao & Ratra [156] performed analysis of constraints on the parameters of the **spatially flat** and **non-flat ΛCDM**, **XCDM**, and **ϕCDM-RP models** from joint datasets consisting of data of the updated 32 $H(z)$ Hubble parameter, 12 BAO peak length scale, 1048 Pantheon SNe Ia apparent magnitudes, 20 binned DES-3yr SNe Ia apparent magnitudes, 120 QSO-AS and 78 Mg_{II} reverberation-measured QSO, 181 H_{II} starburst galaxy, and 50 Platinum Amati-correlated GRB. As a result, the authors found that constraints from each dataset are mutually consistent. There is a slight difference between constraints determined from the set QSO-AS + H_{II}G + Mg_{II} QSO + A118 data and those from QSO-AS + H_{II}G + Mg_{II} QSO + Platinum + A101 data, so the authors considered only the cosmological constraints from the joint dataset $H(z)$ + BAO peak length scale + SNe Ia apparent magnitudes + QSO-AS + H_{II}G + Mg_{II} QSO + A118 (HzBSNQHMA). The model-independent value of the Hubble constant $H_0 = 69.7 \pm 1.2$ km s^{-1}Mpc^{-1}, and the matter density parameter at present epoch, $\Omega_{\rm m0} = 0.295 \pm 0.017$ obtained by using the HzBSNQHMA dataset. The obtained value of the constraint for H_0 lies in the middle of the spatially flat ΛCDM model result of Planck Collaboration 2018 of Aghanim et al. [13] and the local expansion rate $H(z)$ result of Riess et al. [335], a bit closer to the former. Based on the DIC analysis, the spatially flat ΛCDM model is the most preferable, but both dynamic dark energy models and space curvature are not ruled out. Constraints on the cosmological parameters of the spatially flat and non-flat ϕCDM-RP model, from various datasets, are shown in Figure 74.

Preprints (www.preprints.org) | NOT PEER-REVIEWED | Posted: 27 October 2023 doi:10.20944/preprints202310.1818.v1

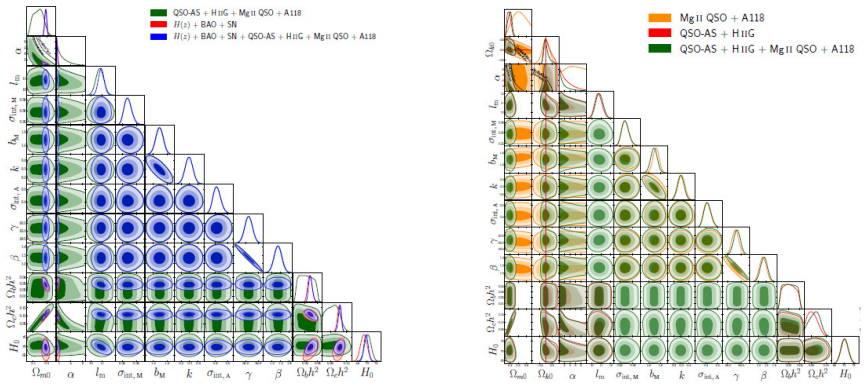

Figure 74. 1σ, 2σ and 3σ confidence level contours constraints on the parameters of the spatially flat (**Left** panel) and spatially non-flat (**Right** panel) ϕCDM model with the RP potential, using various combinations of datasets. The axis with $\alpha = 0$ denotes the spatially flat ΛCDM model. The black dotted lines correspond to lines of zero acceleration and split the parameter space into currently accelerating (bottom left) and currently decelerating (top right) regions. The crimson dash-dot lines denote spatially flat hypersurfaces $\Omega_{k0} = 0$, closed spatial hypersurfaces are located either below or to the left. The figure is adapted from [156].

3.9. X-Ray Gas Mass Fraction of Clusters Data

Using Chandra measurements of X-ray gas mass fraction of 26 rich clusters obtained by Allen et al. [336], Chen & Ratra [285] constrained the parameters of the **ϕCDM-RP**, **ΛCDM**, and the **XCDM models**. Resulting constraints are consistent with those derived from other cosmological tests but favor more the spatially flat ΛCDM model, Figure 75. Constraints on the parameters of the ϕCDM model are tighter than those derived from the SNe Ia apparent magnitude data of Podariu & Ratra [193], Waga & Frieman [337], redshift-angular size data of Chen & Ratra [338], Podariu et al. [339], gravitational lensing statistics of Chae et al. [340], Figure 75 (Left panel).

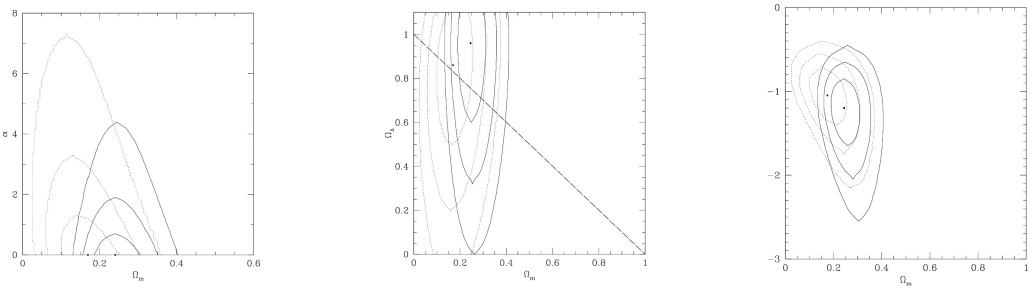

Figure 75. 1σ, 2σ and 3σ confidence level contours constraints on parameters. (**Left** panel) For the spatially flat ϕCDM model with the RP potential and non-relativistic CDM. Continuous lines are obtained for $h = 0.72 \pm 0.08$ and $\Omega_b h^2 = 0.0214 \pm 0.002$ while dotted lines match $h = 0.68 \pm 0.04$ and $\Omega_b h^2 = 0.014 \pm 0.004$. (**middle** panel) For the spatially flat ΛCDM model. Continuous lines are obtained for $h = 0.72 \pm 0.08$ and $\Omega_b h^2 = 0.0214 \pm 0.002$ while dotted lines obtained for $h = 0.68 \pm 0.04$ and $\Omega_b h^2 = 0.014 \pm 0.004$. The diagonal dash-dotted line delimits spatially flat models. (**Right** panel) For the XCDM model. Continuous lines are obtained for $h = 0.72 \pm 0.08$ and $\Omega_b h^2 = 0.0214 \pm 0.002$ while dotted lines are derived for $h = 0.68 \pm 0.04$ and $\Omega_b h^2 = 0.014 \pm 0.004$. In all pictures, two dots indicate the place of maximum probability. The figure is adapted from [285].

Wilson et al. [286] used the R04 gold SNe Ia apparent magnitude versus the redshift data of Riess et al. [162], and X-ray gas mass fraction of clusters data of Allen et al. [336] to constrain the **ϕCDM-RP model**; the results are given in Figure 76. According to these results, the standard spatially flat ΛCDM model is more preferable, but the ϕCDM model is not ruled out either. The contours obtained from joint R04 gold SNe Ia apparent magnitude data and galaxy cluster gas mass fraction data are tighter

Preprints (www.preprints.org) | NOT PEER-REVIEWED | Posted: 27 October 2023 doi:10.20944/preprints202310.1818.v1

constrained than those obtained by Podariu & Ratra [193] from earlier SNe Ia apparent magnitude versus redshift data.

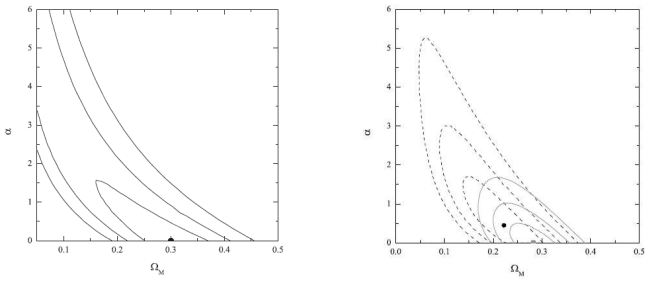

Figure 76. 1σ, 2σ and 3σ confidence level contours constraints on the parameters of the ϕCDM model with the RP potential. (**Left** panel) For the R04 gold SNe Ia apparent magnitude sample. The dot indicates the maximum likelihood for which $\Omega_{\rm m0} = 0.30$ and $\alpha = 0$. (**Right** panel) For the joint R04 gold SNe Ia apparent magnitude sample and galaxy cluster gas mass fraction data. The solid gray lines are computed for $h = 0.72 \pm 0.08$ and $\Omega_{\rm b}h^2 = 0.0214 \pm 0.002$ with maximum likelihood at $\Omega_{\rm m0} = 0.28$ and $\alpha = 0$. The black dotted lines are computed for $h = 0.68 \pm 0.04$ and $\Omega_{\rm b}h^2 = 0.014 \pm 0.004$, with maximum likelihood at $\Omega_{\rm m0} = 0.22$ and $\alpha = 0.45$. The figure is derived from constraints on the parameters of the spatially flat ΛCDM, the XCDM, and the ϕCDM models with the RP potential adapted from [286].

Constraints on the model parameters w_0 and w_a of the w**CDM model** using the X-ray temperature data of massive galaxy clusters within the redshift range $0.05 \leq z \leq 0.83$ with massive galaxy clusters ($M_{\rm cluster} > 8 \times 10^{14}\ h^{-1} M_\odot$ within a comoving radius of $R_{\rm cluster} = 1.5\ h^{-1}$Mpc), were determined by Campanelli et al. [341]. The results are presented in Figure 77. Current data on massive clusters weakly constrain w_0 and w_a parameters around the $(w_0, w_a) = (-1, 0)$ values corresponding to the ΛCDM model. In the analysis including data from the galaxy cluster number count, Hubble parameter $H(z)$, CMB temperature anisotropy, BAO peak length scale, and the SNe Ia apparent magnitude, the values of $w_0 = -1.14^{+0.14}_{-0.16}$ and $w_a = 0.85^{+0.42}_{0.60}$ were obtained at 1σ confidence level.

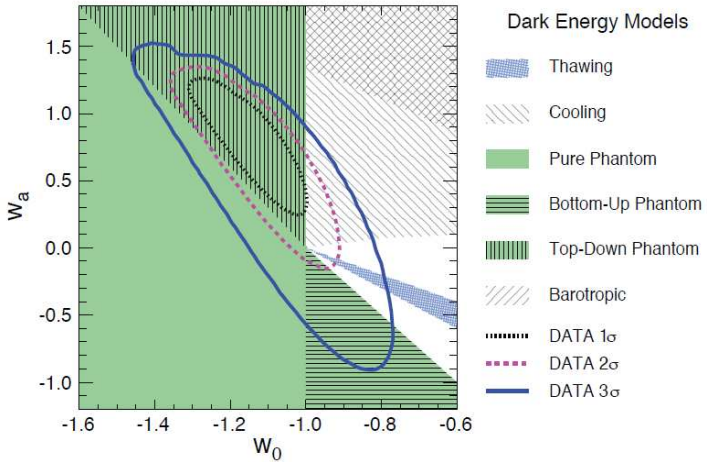

Figure 77. 1σ, 2σ and 3σ confidence level contours in the $w_0 - w_a$ plane from the data analysis of the galaxy cluster number count, Hubble parameter $H(z)$, CMB temperature anisotropy, BAO peak length scale, and the SNe Ia apparent magnitude. The shaded areas represent various types of dynamical dark energy models. The figure is adapted from [341]

.

Chen and Ratra [342] applied angular size versus redshift measurements for galaxy clusters from Bonamente et al. [343] to constraint parameters of the ϕ**CDM-RP**, the **XCDM**, and the Λ**CDM**

Preprints (www.preprints.org) | NOT PEER-REVIEWED | Posted: 27 October 2023 doi:10.20944/preprints202310.1818.v1

models. X-ray observations of the intracluster medium in combination with radio observations of the Sunyaev-Zel'dovich effect of galaxy clusters make it possible to estimate the distance from the angular diameter d_A of galaxy clusters. The authors applied the 38 angular diameter distance measurements of Bonamente et al. (2006) to constrain cosmological parameters of the models presented above. The results are demonstrated in Figure 78. The analysis of the angular size measurements along with the more restrictive BAO peak length scale data and the SNe Ia apparent magnitude measurements favors the spatially flat ΛCDM model but does not exclude the ϕCDM model.

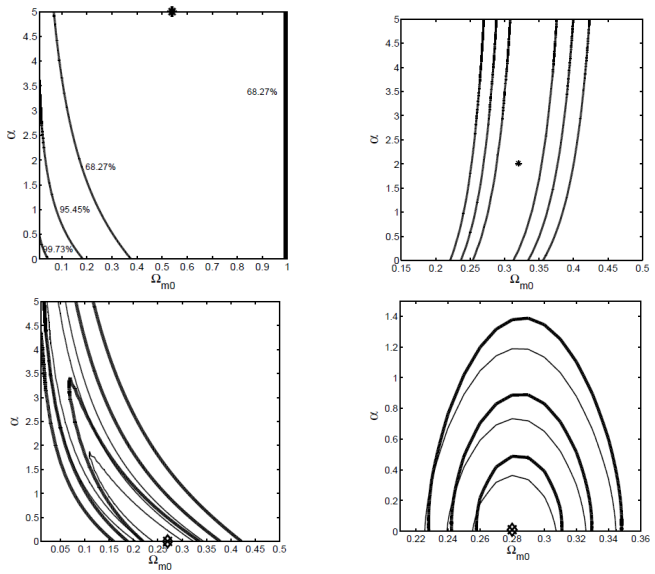

Figure 78. 1σ, 2σ and 3σ confidence level contours constraints on the parameters of the ϕCDM model with the RP potential. The horizontal axis with $\alpha = 0$ corresponds to the standard spatially flat ΛCDM model. (**Left upper** panel) Contours obtained from angular diameter distance data. (**Right upper** panel) Contours obtained using BAO peak length scale data. (**Left lower** panel) Contours obtained from SNe Ia apparent magnitude data. (**Right lower** panel) Contours were obtained from a joint analysis of BAO peak length scale and SNe Ia apparent magnitude (with systematic errors) data, with (and without) angular diameter distance data. The figure is adapted from [342].

3.10. Reionization Data

Mitra et al. [144] studied the influence of dynamical dark energy and spatial curvature on cosmic reionization. For this aim, the authors examined reionization in the **tilted spatially flat** and **untilted spatially non-flat XCDM** and **ϕCDM-RP quintessential inflation models**. Statistical analysis was performed based on a principal component analysis and the MCMC analysis using a compilation of the lower-redshift reionization data by Wyithe & Bolton [344], Becker & Bolton [345] to estimate uncertainties in the model reionization histories. The obtained constraints for the tilted spatially flat and untilted spatially non-flat dynamical inflation ϕCDM model with the RP potential are shown in Figure 79. The authors found that regardless of the nature of dark energy, there are significant differences between the reionization histories of the spatially flat and spatially non-flat cosmological models. Although both the flat and non-flat models fit well the low-redshift $z \leq 6$ reionization observations, there is a discrepancy between high-redshifts $z \geq 7$ Lyman-α emitter data by Songaila & Cowie [346], Prochaska et al. [347] and the predictions from spatially non-flat models.

Preprints (www.preprints.org) | NOT PEER-REVIEWED | Posted: 27 October 2023 doi:10.20944/preprints202310.1818.v1

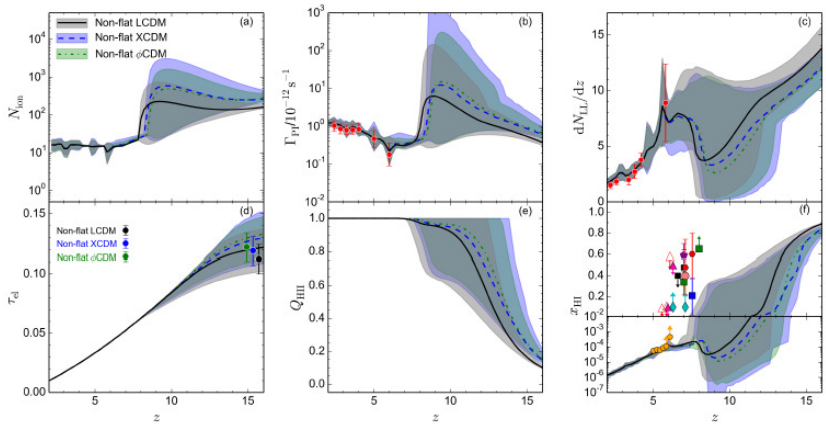

Figure 79. Constraints on various quantities related to reionization obtained from the MCMC analysis for the untilted spatially non-flat ΛCDM, XCDM, ϕCDM quintessential inflation models that fit best the dataset: Planck 2015 TT + lowP + lensing and SNe Ia apparent magnitude, BAO peak length scale, $H(z)$ and LSS growth rate data. The thick central lines along with surrounding shaded regions correspond to best-fit models and their 2σ uncertainty ranges. (**Upper** panels) (**a**) a number of ionizing photons in the IGM per baryon in stars, (**b**) photoionization rates for hydrogen along with observational data of Wyithe & Bolton [344], Becker & Bolton [345], (**c**) a specific number of Lyman-limit systems with data points of Songaila & Cowie [346], Prochaska et al. [347]. (Lower panel) (**d**) electron scattering optical depths along with their values of Park & Ratra [246], (**e**) volume filling factor of ionized regions, (**f**) global neutral hydrogen fraction with different present observational limits. The figure is adapted from [252].

3.11. Gravitational Lensing Data

Constraints on the parameters of two **ϕCDM models**, with the **RP** and the **pNGb potentials**, were analyzed by Waga & Frieman [337]. These models predict radically different futures for our universe. In the model with the RP potential, the expansion of the universe will continue to accelerate. In the model with the pNGb potential, the present epoch of the expansion of the universe with acceleration will be followed by a return to the matter-dominated epoch. For these observational tests, the authors used the compilation of measurements: gravitational lensing statistics [348–352], and the high-z SNe Ia apparent magnitudes [162,353,354]. The results of these studies are presented in Figure 80, where it is shown that a large region of parameter space for the considered models is consistent with the SNe Ia apparent magnitude data if $\Omega_{m0} > 0.15$. The authors obtained the constraint on the model parameter α of the RP potential, $\alpha < 5$. The ϕCDM model with the pNGb potential is constrained by the SNe Ia apparent magnitude and lensing measurements at 2σ confidence level.

Preprints (www.preprints.org) | NOT PEER-REVIEWED | Posted: 27 October 2023 doi:10.20944/preprints202310.1818.v1

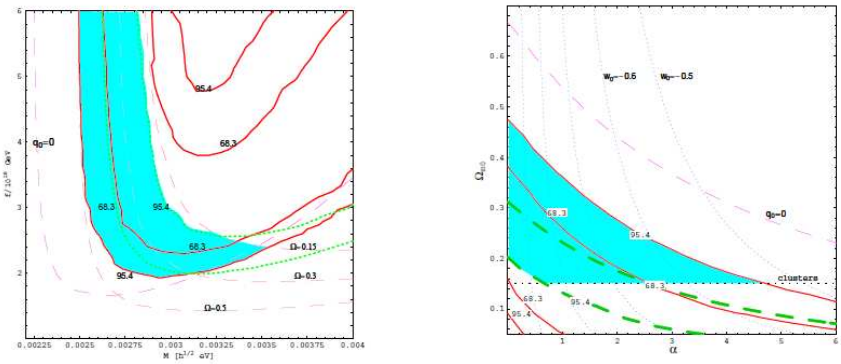

Figure 80. 1σ, 2σ confidence level contours arising from lensing statistics and SNe Ia apparent magnitude versus redshift data (solid curves). (**Left** panel) The ϕCDM model with the pNGb potential. Solid curves correspond to constraints from SNe Ia apparent magnitude data. Contours of the constant matter energy parameter at present epoch Ω_{m0} and the limit for the acceleration parameter at present epoch $q_0 = 0$ are depicted. (**Right** panel) The ϕCDM model with the RP potential. The lower bound of $\Omega_{m0} = 0.15$ from clusters and curves for the constant value of the EoS parameter at present epoch w_0 are shown. The figure is adapted from [337].

Statistics of the strong gravitational lensing based on Cosmic Lens All-Sky Survey data of Myers et al. [355], Browne et al. [356] was applied by Chae et al. [340] to constrain parameters of the **ϕCDM-RP model**. The results are presented in Figure 81. The maximum of the likelihood accords to the values of the matter density parameter at present epoch $\Omega_{m0} = 0.34$ and the model parameter $\alpha = 0$, *i.e.*, to the standard **spatially flat ΛCDM model**. For the 68% confidence level, $0.18 < \Omega_{m0} < 0.62$ and $\alpha < 2.7$, while for 95% confidence level, $\Omega_{m0} = 1$ and $\alpha = 8$. Strong gravitational lensing constraints are favorable for the standard spatially flat ΛCDM model, and consistent with Chen & Ratra [338] constraints from the SNe Ia apparent magnitude data, but are weaker.

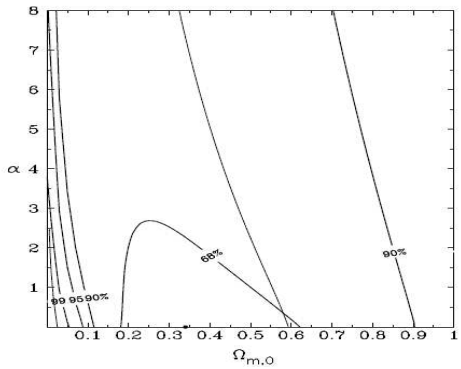

Figure 81. 68%, 90%, 95%, and 99% confidence level contours constraints on the parameters of the ϕCDM model with the RP potential from the strong gravitational lensing data. The thin line represents the 68% confidence level derived from the SNe Ia apparent magnitude versus redshift data by Chen & Ratra [338]. The horizontal axis for which $\alpha = 0$ corresponds to the spatially flat ΛCDM model. The figure is adapted from [340].

3.12. Compact Radio Sources Data

The compact radio source angular size versus redshift data of Gurvits et al. [357] were used by Chen & Ratra [338] to derive constraints on the parameters of the **ϕCDM-RP model**. These constraints are consistent with the results obtained from the SNe Ia apparent magnitude data of [2,162], but they are less restrictive, Figure 82.

Preprints (www.preprints.org) | NOT PEER-REVIEWED | Posted: 27 October 2023 doi:10.20944/preprints202310.1818.v1

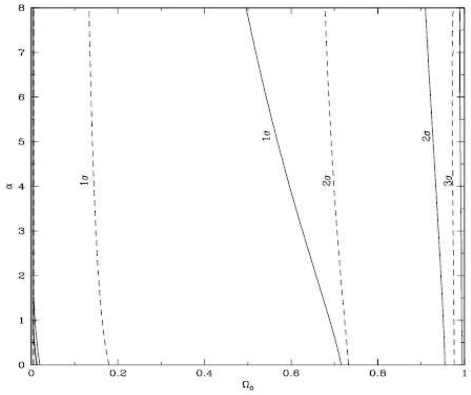

Figure 82. 1σ, 2σ and 3σ confidence level contours constraints on the parameters of the spatially flat ϕCDM model with the RP potential. Solid lines are contours computed for the uniform prior $p(\Omega_0) = 1$. Short dashed lines are obtained for the logarithmic prior $p(\Omega_0) = 1/\Omega_0$. The figure is adapted from [338].

Podariu et al. [339] used double radio galaxies called FRIIb sources, redshift-angular size data to constrain the parameters of the **ϕCDM-RP model** in the **spatially flat** universe. These constraints are consistent both with the results obtained from the SNe Ia apparent magnitude data of [2,162] as well as with the results obtained from the compact radio source redshift-angular size data of Chen & Ratra in [338], but they are less restrictive, Figure 83.

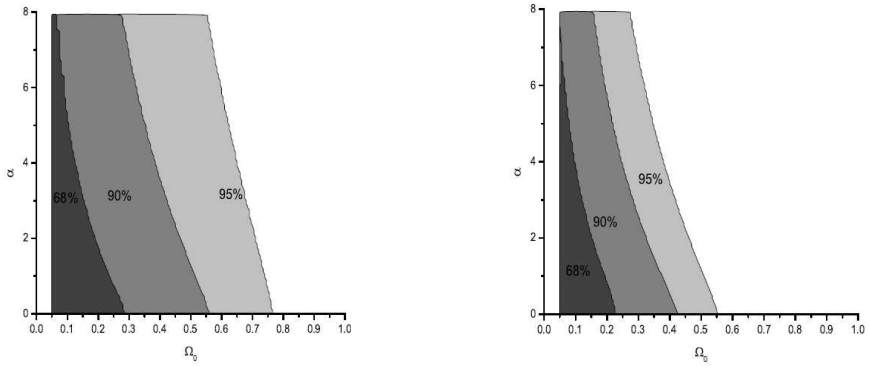

Figure 83. 1σ, 2σ and 3σ confidence level contours constraints on the parameters of the spatially flat ϕCDM model with the RP potential. (**Left** panel) Constraints were obtained using all twenty radio galaxies (including 3C 427.1). (**Right** panel) Constraints were obtained using only nineteen radio galaxies (excluding 3C 427.1). The figure is adapted from [339].

4. Discussion and Conclusions

In this review, we presented papers devoted to observational constraints on cosmological parameters in dynamical dark energy models through cosmological observations. Our review does not claim to be a complete presentation of all research conducted by scientists in this area. We considered the most significant papers among numerous ones, where the authors applied different types of methods and observational constraints with various observational datasets to investigate dynamical dark energy models. Most of papers presented here are devoted to the study of the quintessence scalar field ϕCDM model with the inverse power-law RP potential. This model is a simplest and a typical representative of a family of tracker quintessence scalar models, and in general, describes properties and features of tracker quintessence scalar field models. Due to the simplicity of the potential form, this model has attracted and will continue to attract many scientists to study it. This review is a kind of historical cross-section of the study of dynamical dark energy models, in which it is clearly seen that the complication, refinement, and increase in the diversity of cosmological data and methods for

 doi:10.20944/preprints202310.1818.v1

studying dynamical dark energy models lead to more precise constraints on values of cosmological parameters. At the same time, despite the refinement of observational data and complications of methods for studying dark energy in the universe, current observational data favor the standard spatially flat ΛCDM model, while not excluding dynamical dark energy models and spatially closed hyperspaces.

We look forward to a larger and better compilation of various cosmological data, which should provide much tighter constraints on cosmological parameters in dynamical dark energy models than those obtained to date. To study GRB and X-ray for investigating the early universe, it is scheduled to launch: the Space-based multiband astronomical Variable Objects Monitor (SVOM) mission [358] (expected in 2023), the Transient High-Energy Sky and Early Universe Surveyor (THESEUS) mission [359] (expected in 2037), the Hydrogen Intensity and Real-time Analysis Experiment(HIRAX) (https://hirax.ukzn.ac.za) (planned). To investigate the weak lensing surveys BAOs peak length scale and RSD, it is planned to launch: the 4-metre Multi-Object Spectroscopic Telescope (4MOST) (https://www.eso.org/sci/facilities/develop/instruments/4MOST.html)(expected in 2023), and the BAO from Integrated Neutral Gas Observations (BINGO) project (https://bingotelescope.org) (planned). To investigate the acceleration expansion of the universe, the nature of the dark universe, the dynamics and evolution of the universe, and the growth of LSS in the universe, it is scheduled to launch: the Euclidean Space Telescope (EUCLID) (https://www.euclid-ec.org/) (expected in 2023), the Spectro-Photometer for the History of the universe (SPHEREx) (https://spherex) (expected in 2025), the Wide-Field Infrared Telescope (WFIRST) (https://web.archive.org/web/20150214063216/https://wfirst.gsfc.nasa.gov/observatory/) (expected in 2027), the ArmazoNes high Dispersion Echelle Spectrograph (ANDES) (https://elt.eso.org/instrument/ANDES/) (planned), the Extremely Large Telescope (ELT) (https://elt.eso.org) (expected in 2027), the Rubin Observatory Legacy Survey of Space and Time (Rubin/LSST) (https://lsst.org) (expected in 2024-2034), the Simons Observatory (SO) (https://simonsobservatory.org) (expected in 2024-2029). To explore the CMB radiation, it is planned to launch: the Cosmic Microwave Background-Stage IV (CMB-S4) experiment (https://cmb-s4.org) (expected in 2029-2036), and the Lite Satellite for the studies of B-mode polarization and Inflation from Cosmic Background Radiation Detection (LiteBIRD) (https://litebird.html) (planned), to study the fingerprint of primordial gravitational waves in CMB, it is also planned the SPIDER experiment (https://spider.princeton.edu).

After completing these missions, very precise measurements of GRB, X-ray temperature of massive galaxy clusters, the expansion rate of the universe $H(z)$, BAO peak length scale, CMB radiation, the angular diameter distance, and LSS growth rate of matter density fluctuations in the universe will be obtained. These precise measurements will constrain parameters in many dark energy models, and some of them may be precluded.

Acknowledgments: We appreciate useful comments and discussions with Bharat Ratra. OA, TK and LS acknowledge partial support from the Shota Rustaveli Georgian NSF grant FR-19-8306. TK acknowledges partial support from the NASA ATP award 80NSSC22K0825.

References

1. A. G. Riess, A. V. Filippenko, P. Challis, A. Clocchiatti, A. Diercks, P. M. Garnavich, R. L. Gilliland, C. J. Hogan, S. Jha, R. P. Kirshner, et al., Astron. J. **116**, 1009 (1998).
2. S. Perlmutter, G. Aldering, G. Goldhaber, R. A. Knop, P. Nugent, P. G. Castro, S. Deustua, S. Fabbro, A. Goobar, D. E. Groom, et al., Astrophys. J **517**, 565 (1999).
3. A. G. Riess, L.-G. Strolger, S. Casertano, H. C. Ferguson, B. Mobasher, B. Gold, P. J. Challis, A. V. Filippenko, S. Jha, W. Li, et al., Astrophys. J **659**, 98 (2007).
4. G. F. Smoot, C. L. Bennett, A. Kogut, E. Wright, J. Aymon, N. Boggess, E. Cheng, G. De Amici, S. Gulkis, M. Hauser, et al., Astrophys. J **396**, L1 (1992).
5. C. L. Bennett, A. Banday, K. M. Gorski, G. Hinshaw, P. Jackson, P. Keegstra, A. Kogut, G. F. Smoot, D. T. Wilkinson, and E. L. Wright, Astrophys. J. Lett. **464**, L1 (1996).

6. D. N. Spergel, L. Verde, H. V. Peiris, E. Komatsu, M. R. Nolta, C. L. Bennett, M. Halpern, G. Hinshaw, N. Jarosik, A. Kogut, et al., The Astrophysical Journal Supplement Series **148**, 175 (2003).
7. D. N. Spergel, R. Bean, O. Doré, M. R. Nolta, C. L. Bennett, J. Dunkley, G. Hinshaw, N. Jarosik, E. Komatsu, L. Page, et al., Astrophys. J. Suppl. **170**, 377 (2007).
8. G. Hinshaw, J. L. Weiland, R. S. Hill, N. Odegard, D. Larson, C. L. Bennett, J. Dunkley, B. Gold, M. R. Greason, N. Jarosik, et al., Astrophys. J. Suppl. **180**, 225 (2009).
9. M. R. Nolta, J. Dunkley, R. S. Hill, G. Hinshaw, E. Komatsu, D. Larson, L. Page, D. N. Spergel, C. L. Bennett, B. Gold, et al., Astrophys. J. Suppl. **1**, 296 (2009).
10. E. Komatsu, K. M. Smith, J. Dunkley, C. L. Bennett, B. Gold, G. Hinshaw, N. Jarosik, D. Larson, M. R. Nolta, L. Page, et al., Astrophys. J. Suppl. **192**, 18 (2011).
11. Planck Collaboration, P. A. R. Ade, N. Aghanim, C. Armitage-Caplan, M. Arnaud, M. Ashdown, F. Atrio-Barandela, J. Aumont, C. Baccigalupi, A. J. Banday, et al., Astron. Astrophys. **571**, A16 (2014).
12. Planck Collaboration, P. A. R. Ade, N. Aghanim, M. Arnaud, M. Ashdown, J. Aumont, C. Baccigalupi, A. J. Banday, R. B. Barreiro, J. G. Bartlett, et al., Astron. Astrophys. **594**, A13 (2016).
13. Planck Collaboration, N. Aghanim, Y. Akrami, M. Ashdown, J. Aumont, C. Baccigalupi, M. Ballardini, A. J. Banday, R. B. Barreiro, N. Bartolo, et al., Astron. Astrophys. **641**, A6 (2020).
14. SDSS, http://www.sdss.org/ (2000).
15. S. Dodelson, V. K. Narayanan, M. Tegmark, R. Scranton, T. Budavári, A. Connolly, I. Csabai, D. Eisenstein, J. A. Frieman, J. E. Gunn, et al., Astrophys. J **572**, 140 (2002).
16. 2dFGRS, http://www.mso.anu.edu.au/2dFGRS/ (2002).
17. W. J. Percival, S. Cole, D. J. Eisenstein, R. C. Nichol, J. A. Peacock, A. C. Pope, and A. S. Szalay, Mon. Not. Roy. Astron. Soc. **381**, 1053 (2007).
18. DES, https://www.darkenergysurvey.org/ (2013).
19. J. Kwan, C. Sánchez, J. Clampitt, J. Blazek, M. Crocce, B. Jain, J. Zuntz, A. Amara, M. R. Becker, G. M. Bernstein, et al., Mon. Not. Roy. Astron. Soc. **464**, 4045 (2017).
20. D. J. Eisenstein, I. Zehavi, D. W. Hogg, R. Scoccimarro, M. R. Blanton, R. C. Nichol, R. Scranton, H.-J. Seo, M. Tegmark, Z. Zheng, et al., Astrophys. J **633**, 560 (2005).
21. C. Blake, E. A. Kazin, F. Beutler, T. M. Davis, D. Parkinson, S. Brough, M. Colless, C. Contreras, W. Couch, S. Croom, et al., Mon. Not. Roy. Astron. Soc. **418**, 1707 (2011).
22. F. Beutler, C. Blake, M. Colless, D. H. Jones, L. Staveley-Smith, L. Campbell, Q. Parker, W. Saunders, and F. Watson, Mon. Not. Roy. Astron. Soc. **416**, 3017 (2011).
23. L. Anderson, É. Aubourg, S. Bailey, F. Beutler, V. Bhardwaj, M. Blanton, A. S. Bolton, J. Brinkmann, J. R. Brownstein, A. Burden, et al., Mon. Not. Roy. Astron. Soc. **441**, 24 (2014).
24. A. J. Ross, L. Samushia, C. Howlett, W. J. Percival, A. Burden, and M. Manera, Mon. Not. Roy. Astron. Soc. **449**, 835 (2015).
25. S. Alam, M. Ata, S. Bailey, F. Beutler, D. Bizyaev, J. A. Blazek, A. S. Bolton, J. R. Brownstein, A. Burden, C.-H. Chuang, et al., Mon. Not. Roy. Astron. Soc. **470**, 2617 (2017).
26. M. Ata, F. Baumgarten, J. Bautista, F. Beutler, D. Bizyaev, M. R. Blanton, J. A. Blazek, A. S. Bolton, J. Brinkmann, J. R. Brownstein, et al., Mon. Not. Roy. Astron. Soc. **473**, 4773 (2018).
27. HST, https://www.stsci.edu/hst (1990).
28. D. Stern, R. Jimenez, L. Verde, M. Kamionkowski, and S. A. Stanford, JCAP **02**, 008 (2010).
29. A. G. Riess, L. Macri, S. Casertano, H. Lampeitl, H. C. Ferguson, A. V. Filippenko, S. W. Jha, W. Li, and R. Chornock, Astrophys. J **730**, 119 (2011).
30. M. Moresco, L. Verde, L. Pozzetti, R. Jimenez, and A. Cimatti, JCAP **07**, 053 (2012).
31. C. Zhang, H. Zhang, S. Yuan, S. Liu, T.-J. Zhang, and Y.-C. Sun, Research in Astronomy and Astrophysics **14** (2014).
32. T. Delubac, J. E. Bautista, N. G. Busca, J. Rich, D. Kirkby, S. Bailey, A. Font-Ribera, A. Slosar, K.-G. Lee, M. M. Pieri, et al., Astron. Astrophys. **574**, A59 (2015).
33. M. Moresco, Mon. Not. Roy. Astron. Soc. **450**, L16 (2015).
34. M. Moresco, L. Pozzetti, A. Cimatti, R. Jimenez, C. Maraston, L. Verde, D. Thomas, A. Citro, R. Tojeiro, and D. Wilkinson, JCAP **05**, 014 (2016).
35. A. L. Ratsimbazafy, S. I. Loubser, S. M. Crawford, C. M. Cress, B. A. Bassett, R. C. Nichol, and P. Väisänen, Mon. Not. Roy. Astron. Soc. **467**, 3239 (2017).

36. P. J. E. Peebles and B. Ratra, Rev. Mod. Phys. **75**, 559 (2003).
37. E. J. Copeland, M. Sami, and S. Tsujikawa, Int. J. Mod. Phys. **D15**, 1753 (2006).
38. J. Frieman, M. Turner, and D. Huterer, Ann. Rev. Astron. Astrophys. **46**, 385 (2008).
39. R. R. Caldwell and M. Kamionkowski, Ann. Rev. Nucl. Part. Sci. **59**, 397 (2009).
40. S. Tsujikawa, Lect. Notes Phys. **800**, 99 (2010).
41. S. Tsujikawa, arXiv:1004.1493 (2010).
42. D. H. Weinberg, M. J. Mortonson, D. J. Eisenstein, C. Hirata, A. G. Riess, and E. Rozo, Phys. Rept. **530**, 87 (2013).
43. J. Yoo and Y. Watanabe, Int. J. Mod. Phys. **D21**, 1230002 (2012).
44. V. C. Rubin, N. Thonnard, and W. K. Ford, Jr., Astrophys. J. **238**, 471 (1980).
45. V. A. Rubakov, Proceedings, 2011 European School of High-Energy Physics ESHEP 2011): Cheile Gradistei, Romania, September 7-20, 2011 pp. 151–195 (2014).
46. M. Tristram, A. J. Banday, M. Douspis, X. Garrido, K. M. Górski, S. Henrot-Versillé, S. Ilić, R. Keskitalo, G. Lagache, C. R. Lawrence, et al., arXiv:2309.10034 (2023).
47. A. Silvestri and M. Trodden, Rept. Prog. Phys. **72**, 096901 (2009).
48. M. Lopez-Corredoira, arXiv:2307.10606 (2023).
49. P. J. E. Peebles, *Principles of physical cosmology* (Univ. Pr., Princeton, USA, 1994).
50. S. Weinberg, *Cosmology* (Oxford Univ. Pr., Oxford, UK, 2008).
51. S. Dodelson and F. Schmidt, *Modern cosmology* (Academic Press is an imprint of Elsevier, London, UK, 2021).
52. D. Baumann, *Cosmology* (Cambridge University Press, 2022).
53. D. Huterer, *A Course in Cosmology* (Cambridge University Press, 2023).
54. S. M. Carroll, W. H. Press, and E. L. Turner, Annu. Rev. Astro. Astrophys. **30**, 499 (1992).
55. S. M. Carroll, Living Rev. Rel. **4**, 1 (2001).
56. E. J. Copeland, M. Sami, and S. Tsujikawa, Int. J. Mod. Phys. **D15**, 1753 (2006).
57. J. Martin, Comptes Rendus Physique **13**, 566 (2012).
58. A. Padilla, arXiv:1502.05296 (2015).
59. N. Deruelle and J.-P. Uzan, *Relativity in Modern Physics*, Oxford Graduate Texts (Oxford University Press, 2018).
60. S. Weinberg, Rev. Mod. Phys. **61**, 1 (1989).
61. S. Weinberg, Sources and detection of dark matter and dark energy in the universe. Proceedings, 4th International Symposium, DM 2000, Marina del Rey, USA, February 23-25, 2000 pp. 18–26 (2000).
62. T. Padmanabhan, Phys. Rept. **380**, 235 (2003).
63. E. Di Valentino, Universe **8**, 399 (2022).
64. E. Abdalla, G. F. Abellán, A. Aboubrahim, A. Agnello, Ö. Akarsu, Y. Akrami, G. Alestas, D. Aloni, L. Amendola, L. A. Anchordoqui, et al., Journal of High Energy Astrophysics **34**, 49 (2022).
65. P. J. E. Peebles, Annals Phys. **447**, 169159 (2022).
66. E. Di Valentino, O. Mena, S. Pan, L. Visinelli, W. Yang, A. Melchiorri, D. F. Mota, A. G. Riess, and J. Silk, Class. Quant. Grav. **38**, 153001 (2021).
67. A. Bernui, E. Di Valentino, W. Giarè, S. Kumar, and R. C. Nunes, Phys. Rev. D **107**, 103531 (2023).
68. F. Niedermann and M. S. Sloth, arXiv:2307.03481 (2023).
69. H. B. Benaoum, L. Á. García, and L. Castañeda, arXiv:2307.05917 (2023).
70. G. A. Hoerning, R. G. Landim, L. O. Ponte, R. P. Rolim, F. B. Abdalla, and E. Abdalla, arXiv:2308.05807 (2023).
71. J.-J. Wei and F. Melia, Astrophys. J **955**, 101 (2023).
72. T. L. Smith and V. Poulin, arXiv:2309.03265 (2023).
73. E. M. Teixeira, R. Daniel, N. Frusciante, and C. van de Bruck, arXiv:2309.06544 (2023).
74. M. Raveri, arXiv:2309.06795 (2023).
75. T. Kodama, T. Shinohara, and T. Takahashi, arXiv:2309.11272 (2023).
76. S. Aiola, E. Calabrese, L. Maurin, S. Naess, B. L. Schmitt, M. H. Abitbol, G. E. Addison, P. A. R. Ade, D. Alonso, M. Amiri, et al., JCAP **2020**, 047 (2020).
77. A. G. Riess, L. M. Macri, S. L. Hoffmann, D. Scolnic, S. Casertano, A. V. Filippenko, B. E. Tucker, M. J. Reid, D. O. Jones, J. M. Silverman, et al., Astrophys. J **826**, 56 (2016).
78. V. Bonvin, F. Courbin, S. H. Suyu, P. J. Marshall, C. E. Rusu, D. Sluse, M. Tewes, K. C. Wong, T. Collett, C. D. Fassnacht, et al., Mon. Not. Roy. Astron. Soc. **465**, 4914 (2017).

79. A. G. Riess, S. A. Rodney, D. M. Scolnic, D. L. Shafer, L.-G. Strolger, H. C. Ferguson, M. Postman, O. Graur, D. Maoz, S. W. Jha, et al., Astrophys. J **853**, 126 (2018).
80. S. Birrer, T. Treu, C. E. Rusu, V. Bonvin, C. D. Fassnacht, J. H. H. Chan, A. Agnello, A. J. Shajib, G. C. F. Chen, M. Auger, et al., Mon. Not. Roy. Astron. Soc. **484**, 4726 (2019).
81. A. G. Riess, S. Casertano, W. Yuan, L. M. Macri, and D. Scolnic, Astrophys. J. **876**, 85 (2019).
82. A. G. Riess, S. Casertano, W. Yuan, J. B. Bowers, L. Macri, J. C. Zinn, and D. Scolnic, Astrophys. J. Lett. **908**, L6 (2021).
83. S. Joudaki, C. Blake, C. Heymans, A. Choi, J. Harnois-Deraps, H. Hildebrandt, B. Joachimi, A. Johnson, A. Mead, D. Parkinson, et al., Mon. Not. Roy. Astron. Soc. **465**, 2033 (2017).
84. T. M. C. Abbott, M. Aguena, A. Alarcon, S. Allam, O. Alves, A. Amon, F. Andrade-Oliveira, J. Annis, S. Avila, D. Bacon, et al., Phys. Rev. D **105**, 023520 (2022).
85. O. H. E. Philcox and M. M. Ivanov, Phys. Rev. D **105**, 043517 (2022).
86. Planck Collaboration, N. Aghanim, Y. Akrami, M. Ashdown, J. Aumont, C. Baccigalupi, M. Ballardini, A. J. Banday, R. B. Barreiro, N. Bartolo, et al., Astron. Astrophys. **641**, A5 (2020).
87. E. Di Valentino, A. Melchiorri, and J. Silk, Nature Astron. **4**, 196 (2019).
88. E. Di Valentino, A. Melchiorri, O. Mena, S. Pan, and W. Yang, Mon. Not. Roy. Astron. Soc. **502**, L23 (2021).
89. E. Di Valentino, Universe **8**, 399 (2022).
90. B. Ratra and P. J. E. Peebles, Phys. Rev. **D37**, 3406 (1988).
91. B. Ratra and P. J. E. Peebles, Astrophys. J. **325**, L17 (1988).
92. C. Wetterich, Nucl. Phys. **B302**, 645 (1988).
93. P. Brax and J. Martin, arXiv:astro-ph/0210533 (2002).
94. E. V. Linder, Gen. Rel. Grav. **40**, 329 (2008).
95. Y.-F. Cai, E. N. Saridakis, M. R. Setare, and J.-Q. Xia, Phys. Rept. **493**, 1 (2010).
96. L. Amendola and S. Tsujikawa, *Dark Energy* (Cambridge University Press, 2015).
97. S. Bahamonde, C. G. Böhmer, S. Carloni, E. J. Copeland, W. Fang, and N. Tamanini, Phys. Rept. **775-777**, 1 (2018).
98. D. Piras and L. Lombriser, arXiv:2310.10717 (2023).
99. P. H. Frampton, K. J. Ludwick, and R. J. Scherrer, Phys. Rev. **D84**, 063003 (2011).
100. R. R. Caldwell and E. V. Linder, Phys. Rev. Lett. **95**, 141301 (2005).
101. C. Schimd, I. Tereno, J.-P. Uzan, Y. Mellier, L. van Waerbeke, E. Semboloni, H. Hoekstra, L. Fu, and A. Riazuelo, Astron. Astrophys. **463**, 405 (2007).
102. R. R. Caldwell, Phys. Lett. **B545**, 23 (2002).
103. E. Elizalde, S. Nojiri, and S. D. Odintsov, Phys. Rev. **D70**, 043539 (2004).
104. R. J. Scherrer and A. A. Sen, Phys. Rev. **D78**, 067303 (2008).
105. S. Dutta and R. J. Scherrer, Phys. Lett. **B676**, 12 (2009).
106. P. H. Frampton, K. J. Ludwick, and R. J. Scherrer, Phys. Rev. **D85**, 083001 (2012).
107. K. J. Ludwick, Mod. Phys. Lett. **A32**, 1730025 (2017).
108. L. A. Escamilla, W. Giarè, E. Di Valentino, R. C. Nunes, and S. Vagnozzi, arXiv:2307.14802 (2023).
109. P. J. Steinhardt, L.-M. Wang, and I. Zlatev, Phys. Rev. **D59**, 123504 (1999).
110. T. Chiba, A. De Felice, and S. Tsujikawa, Phys. Rev. **D87**, 083505 (2013).
111. N. A. Lima, A. R. Liddle, M. Sahlén, and D. Parkinson, Phys. Rev. D **93**, 063506 (2016).
112. I. Zlatev, L.-M. Wang, and P. J. Steinhardt, Phys. Rev. Lett. **82**, 896 (1999).
113. E. V. Linder, Phys. Rev. **D91**, 063006 (2015).
114. S. Bag, S. S. Mishra, and V. Sahni, JCAP **08**, 009 (2018).
115. A. A. Starobinsky, Phys. Lett. B **91**, 99 (1980).
116. A. H. Guth, Phys. Rev. D **23**, 347 (1981).
117. V. F. Mukhanov and G. V. Chibisov, JETP Lett. **33**, 532 (1981).
118. A. A. Starobinsky, Phys. Lett. B **117**, 175 (1982).
119. A. D. Linde, Phys. Lett. B **108**, 389 (1982).
120. A. D. Linde, Phys. Lett. B **129**, 177 (1983).
121. F. Lucchin, S. Matarrese, and M. D. Pollock, Phys. Lett. B **167**, 163 (1986).
122. F. Lucchin and S. Matarrese, Phys. Rev. **D32**, 1316 (1985).
123. F. Lucchin and S. Matarrese, Phys. Lett. B **164**, 282 (1985).

124. S. Dodelson, *Modern cosmology* (Academic Press. ISBN, Amsterdam, 2003).
125. D. S. Gorbunov and V. A. Rubakov, *Introduction to the theory of the early universe: Cosmological perturbations and inflationary theory* (World Scientific, Hackensack, USA, 2011).
126. V. Mukhanov, *Physical foundations of cosmology* (Cambridge University Press, 2005).
127. L. Senatore, in *Theoretical Advanced Study Institute in Elementary Particle Physics: New Frontiers in Fields and Strings* (2017).
128. P. J. E. Peebles and A. Vilenkin, Phys. Rev. D **59**, 063505 (1999).
129. J. Rubio and C. Wetterich, Phys. Rev. D **96**, 063509 (2017).
130. B. Ratra, Phys. Rev. **D96**, 103534 (2017).
131. C.-Q. Geng, C.-C. Lee, M. Sami, E. N. Saridakis, and A. A. Starobinsky, JCAP **06**, 011 (2017).
132. Y. Akrami, R. Kallosh, A. Linde, and V. Vardanyan, JCAP **06**, 041 (2018).
133. K. Dimopoulos and C. Owen, JCAP **06**, 027 (2017).
134. C. Wetterich, Astron. Astrophys. **301**, 321 (1995).
135. L. Amendola, Mon. Not. Roy. Astron. Soc. **312**, 521 (2000).
136. L. Amendola, Phys. Rev. **D62**, 043511 (2000).
137. W. Zimdahl and D. Pavon, Phys. Lett. **B521**, 133 (2001).
138. X. Liu, S. Tsujikawa, and K. Ichiki, arXiv:2309.13946 (2023).
139. R. C. Nunes and E. Di Valentino, **104**, 063529 (2021).
140. Y. Zhai, W. Giarè, C. van de Bruck, E. Di Valentino, O. Mena, and R. C. Nunes, JCAP **07**, 032 (2023).
141. S. Pan and W. Yang, arXiv:2310.07260 (2023).
142. O. Farooq, F. R. Madiyar, S. Crandall, and B. Ratra, Astrophys. J. **835**, 26 (2017).
143. J. Ryan, Y. Chen, and B. Ratra, Mon. Not. Roy. Astron. Soc. **488**, 3844 (2019).
144. S. Mitra, C.-G. Park, T. R. Choudhury, and B. Ratra, Mon. Not. Roy. Astron. Soc. **487**, 5118 (2019).
145. N. Khadka and B. Ratra, Mon. Not. Roy. Astron. Soc. **497**, 263 (2020).
146. N. Khadka and B. Ratra, Mon. Not. Roy. Astron. Soc. **492**, 4456 (2020).
147. N. Khadka and B. Ratra, Mon. Not. Roy. Astron. Soc. **502**, 6140 (2021).
148. N. Khadka, Z. Yu, M. Zajaček, M. L. Martinez-Aldama, B. Czerny, and B. Ratra, Mon. Not. Roy. Astron. Soc. **508**, 4722 (2021).
149. N. Khadka and B. Ratra, Mon. Not. Roy. Astron. Soc. **510**, 2753 (2022).
150. N. Khadka, M. L. Martínez-Aldama, M. Zajaček, B. Czerny, and B. Ratra, Mon. Not. Roy. Astron. Soc. **513**, 1985 (2022).
151. S. Cao, J. Ryan, and B. Ratra, Mon. Not. Roy. Astron. Soc. **504**, 300 (2021).
152. S. Cao, N. Khadka, and B. Ratra, Mon. Not. Roy. Astron. Soc. **510**, 2928 (2022).
153. S. Cao, M. Zajaček, S. Panda, M. L. Martínez-Aldama, B. Czerny, and B. Ratra, Mon. Not. Roy. Astron. Soc. **516**, 1721 (2022).
154. S. Cao, M. Dainotti, and B. Ratra, Mon. Not. Roy. Astron. Soc. **512**, 439 (2022).
155. S. Cao, M. Dainotti, and B. Ratra, Mon. Not. Roy. Astron. Soc. **516**, 1386 (2022).
156. S. Cao and B. Ratra, Mon. Not. Roy. Astron. Soc. **513**, 5686 (2022).
157. S. Gariazzo, E. Di Valentino, O. Mena, and R. C. Nunes, Phys. Rev. D **106**, 023530 (2022).
158. W. Yang, S. Pan, O. Mena, and E. Di Valentino (2022), 2209.14816.
159. D. N. Spergel, Science **347**, 1100 (2015).
160. M. S. Madhavacheril, F. J. Qu, B. D. Sherwin, N. MacCrann, Y. Li, I. Abril-Cabezas, P. A. R. Ade, S. Aiola, T. Alford, M. Amiri, et al., arXiv:2304.05203 (2023).
161. D. Brout, D. Scolnic, B. Popovic, A. G. Riess, A. Carr, J. Zuntz, R. Kessler, T. M. Davis, S. Hinton, D. Jones, et al., Astrophys. J **938**, 110 (2022).
162. A. G. Riess, L.-G. Strolger, J. Tonry, S. Casertano, H. C. Ferguson, B. Mobasher, P. Challis, A. V. Filippenko, S. Jha, W. Li, et al., Astrophys. J **607**, 665 (2004).
163. D. M. Scolnic, D. O. Jones, A. Rest, Y. C. Pan, R. Chornock, R. J. Foley, M. E. Huber, R. Kessler, G. Narayan, A. G. Riess, et al., Astrophys. J **859**, 101 (2018).
164. M. Fierz and W. Pauli, Proc. Roy. Soc. Lond. **A173**, 211 (1939).
165. J. Polchinski, *String theory. Vol. 1: An introduction to the bosonic string*, Cambridge Monographs on Mathematical Physics (Cambridge University Press, 2007).
166. N. Arkani-Hamed, S. Dimopoulos, and G. R. Dvali, Phys. Lett. **B429**, 263 (1998).

167. G. R. Dvali, G. Gabadadze, and M. Porrati, Phys. Lett. **B485**, 208 (2000).
168. A. Yu. Kamenshchik, U. Moschella, and V. Pasquier, Phys. Lett. **B511**, 265 (2001).
169. S. Capozziello, S. Carloni, and A. Troisi, Recent Res. Dev. Astron. Astrophys. **1** (2003).
170. R. J. Scherrer, Phys. Rev. Lett. **93**, 011301 (2004).
171. A. Nicolis, R. Rattazzi, and E. Trincherini, Phys. Rev. **D79**, 064036 (2009).
172. M. Shifman, Int. J. Mod. Phys. **A25**, 199 (2010).
173. J. Khoury and M. Wyman, Phys. Rev. **D80**, 064023 (2009).
174. S. Wang, Y. Wang, and M. Li, Phys. Rept. **696**, 1 (2017).
175. R. R. Caldwell, M. Kamionkowski, and N. N. Weinberg, Phys. Rev. Lett. **91**, 071301 (2003).
176. P. G. Ferreira and M. Joyce, Phys. Rev. **D58**, 023503 (1998).
177. P. Brax and J. Martin, Phys. Lett. B **468**, 40 (1999).
178. V. Sahni and L.-M. Wang, Phys. Rev. **D62**, 103517 (2000).
179. T. Barreiro, E. J. Copeland, and N. J. Nunes, Phys. Rev. **D61**, 127301 (2000).
180. A. Albrecht and C. Skordis, Phys. Rev. Lett. **84**, 2076 (2000).
181. L. A. Urena-Lopez and T. Matos, Phys. Rev. **D62**, 081302 (2000).
182. H.-Y. Chang and R. J. Scherrer, arXiv:1608.03291 (2016).
183. J. A. Frieman, C. T. Hill, A. Stebbins, and I. Waga, Phys. Rev. Lett. **75**, 2077 (1995).
184. V. Barger, Y. Gao, and D. Marfatia, Phys. Lett. **B648**, 127 (2007).
185. M. Chevallier and D. Polarski, Int. J. Mod. Phys. **D10**, 213 (2001).
186. E. V. Linder, Phys. Rev. Lett. **90**, 091301 (2003).
187. B. Ratra, Phys. Rev. D **40**, 3939 (1989).
188. B. Ratra, Phys. Rev. D **31**, 1931 (1985).
189. D. Bettoni and J. Rubio, Galaxies **10**, 22 (2022).
190. B. Ratra and P. J. E. Peebles, Phys. Rev. **D52**, 1837 (1995).
191. G. Y. Chitov, T. August, A. Natarajan, and T. Kahniashvili, Phys. Rev. D **83**, 045033 (2011).
192. S. Mandal, G. Y. Chitov, O. Avsajanishvili, B. Singha, and T. Kahniashvili, JCAP **05**, 018 (2021).
193. S. Podariu and B. Ratra, Astrophys. J. **532**, 109 (2000).
194. P. Caresia, S. Matarrese, and L. Moscardini, Astrophys. J. **605**, 21 (2004).
195. P. Binetruy, Phys. Rev. D **60**, 063502 (1999).
196. F. Perrotta, C. Baccigalupi, and S. Matarrese, Phys. Rev. D **61**, 023507 (1999).
197. C. Baccigalupi, S. Matarrese, and F. Perrotta, Phys. Rev. D **62**, 123510 (2000).
198. J. L. Tonry, B. P. Schmidt, B. Barris, P. Candia, P. Challis, A. Clocchiatti, A. L. Coil, A. V. Filippenko, P. Garnavich, C. Hogan, et al., Astrophys. J **594**, 1 (2003).
199. G. Aldering, C. W. Akerlof, R. Amanullah, P. Astier, E. Barrelet, C. Bebek, L. Bergstrom, J. Bercovitz, G. M. Bernstein, M. Bester, et al., in *Future Research Direction and Visions for Astronomy*, edited by A. M. Dressler (2002), vol. 4835 of *Society of Photo-Optical Instrumentation Engineers (SPIE) Conference Series*, pp. 146–157.
200. M. Doran, K. Karwan, and C. Wetterich, JCAP **11**, 007 (2005).
201. D. N. Spergel, L. Verde, H. V. Peiris, E. Komatsu, M. R. Nolta, C. L. Bennett, M. Halpern, G. Hinshaw, N. Jarosik, A. Kogut, et al., Astrophys. J. Suppl. **148**, 175 (2003).
202. A. C. S. Readhead, B. S. Mason, C. R. Contaldi, T. J. Pearson, J. R. Bond, S. T. Myers, S. Padin, J. L. Sievers, J. K. Cartwright, M. C. Shepherd, et al., Astrophys. J **609**, 498 (2004).
203. R. Rebolo, R. A. Battye, P. Carreira, K. Cleary, R. D. Davies, R. J. Davis, C. Dickinson, R. Genova-Santos, K. Grainge, C. M. Gutiérrez, et al., Mon. Not. Roy. Astron. Soc. **353**, 747 (2004).
204. M. Tegmark, M. A. Strauss, M. R. Blanton, K. Abazajian, S. Dodelson, H. Sandvik, X. Wang, D. H. Weinberg, I. Zehavi, N. A. Bahcall, et al., Phys. Rev. D **69**, 103501 (2004).
205. W. L. Freedman, B. F. Madore, B. K. Gibson, L. Ferrarese, D. D. Kelson, S. Sakai, J. R. Mould, J. Kennicutt, Robert C., H. C. Ford, J. A. Graham, et al., Astrophys. J **553**, 47 (2001).
206. A. Fuzfa and J. M. Alimi, AIP Conf. Proc. **861**, 858 (2006).
207. P. Astier, J. Guy, N. Regnault, R. Pain, E. Aubourg, D. Balam, S. Basa, R. G. Carlberg, S. Fabbro, D. Fouchez, et al., Astron. Astrophys. **447**, 31 (2006).
208. A. Pavlov, S. Westmoreland, K. Saaidi, and B. Ratra, **88**, 123513 (2013).
209. O. Farooq, D. Mania, and B. Ratra, Astrophys. Space Sci. **357**, 11 (2015).

210. N. Suzuki, D. Rubin, C. Lidman, G. Aldering, R. Amanullah, K. Barbary, L. F. Barrientos, J. Botyanszki, M. Brodwin, N. Connolly, et al., Astrophys. J **746**, 85 (2012).
211. J. Simon, L. Verde, and R. Jimenez, **71**, 123001 (2005).
212. E. Gaztanaga, A. Cabre, and L. Hui, Mon. Not. Roy. Astron. Soc. **399**, 1663 (2009).
213. W. J. Percival, B. A. Reid, D. J. Eisenstein, N. A. Bahcall, T. Budavari, J. A. Frieman, M. Fukugita, J. E. Gunn, Ž. Ivezić, G. R. Knapp, et al., Mon. Not. Roy. Astron. Soc. **401**, 2148 (2010).
214. O. Farooq, S. Crandall, and B. Ratra, Phys. Lett. B **726**, 72 (2013).
215. M. Blomqvist, H. du Mas des Bourboux, N. G. Busca, V. de Sainte Agathe, J. Rich, C. Balland, J. E. Bautista, K. Dawson, A. Font-Ribera, J. Guy, et al., Astron. Astrophys **629**, A86 (2019).
216. A. Halder and M. Pandey, Mon. Not. Roy. Astron. Soc. **508**, 3446 (2021).
217. R. J. Cooke, M. Pettini, and C. C. Steidel, The Astrophysical Journal **855**, 102 (2018).
218. D. Camarena and V. Marra, Monthly Notices of the Royal Astronomical Society **504**, 5164 (2021).
219. M. Doran, M. J. Lilley, J. Schwindt, and C. Wetterich, Astrophys. J. **559**, 501 (2001).
220. P. de Bernardis, P. A. R. Ade, J. J. Bock, J. R. Bond, J. Borrill, A. Boscaleri, K. Coble, B. P. Crill, G. de Gasperis, G. de Troia, et al. (Boomerang), in *Cosmology and Particle Physics* (2001), vol. 555 of *American Institute of Physics Conference Series*, pp. 85–94.
221. S. Hanany, P. Ade, A. Balbi, J. Bock, J. Borrill, A. Boscaleri, P. de Bernardis, P. G. Ferreira, V. V. Hristov, A. H. Jaffe, et al., Astrophys. J. Lett **545**, L5 (2000).
222. A. Hebecker and C. Wetterich, Phys. Lett. B **497**, 281 (2001).
223. R. R. Caldwell, M. Doran, C. M. Mueller, G. Schafer, and C. Wetterich, Astrophys. J. Lett. **591**, L75 (2003).
224. G. Hinshaw, D. N. Spergel, L. Verde, R. S. Hill, S. S. Meyer, C. Barnes, C. L. Bennett, M. Halpern, N. Jarosik, A. Kogut, et al., Astrophys. J. Suppl. **148**, 135 (2003).
225. A. Kogut, D. N. Spergel, C. Barnes, C. L. Bennett, M. Halpern, G. Hinshaw, N. Jarosik, M. Limon, S. S. Meyer, L. Page, et al., Astrophys. J. Suppl. **148**, 161 (2003).
226. T. J. Pearson, B. S. Mason, A. C. S. Readhead, M. C. Shepherd, J. L. Sievers, P. S. Udomprasert, J. K. Cartwright, A. J. Farmer, S. Padin, S. T. Myers, et al., Astrophys. J **591**, 556 (2003).
227. B. S. Mason, T. J. Pearson, A. C. S. Readhead, M. C. Shepherd, J. Sievers, P. S. Udomprasert, J. K. Cartwright, A. J. Farmer, S. Padin, S. T. Myers, et al., Astrophys. J **591**, 540 (2003).
228. C. L. Kuo, P. A. R. Ade, J. J. Bock, C. Cantalupo, M. D. Daub, J. Goldstein, W. L. Holzapfel, A. E. Lange, M. Lueker, M. Newcomb, et al., Astrophys. J **600**, 32 (2004).
229. W. J. Percival, C. M. Baugh, J. Bland-Hawthorn, T. Bridges, R. Cannon, S. Cole, M. Colless, C. Collins, W. Couch, G. Dalton, et al., Mon. Not. Roy. Astron. Soc. **327**, 1297 (2001).
230. J. A. Peacock, S. Cole, P. Norberg, C. M. Baugh, J. Bland-Hawthorn, T. Bridges, R. D. Cannon, M. Colless, C. Collins, W. Couch, et al., Nature **410**, 169 (2001).
231. L. Verde, A. F. Heavens, W. J. Percival, S. Matarrese, C. M. Baugh, J. Bland-Hawthorn, T. Bridges, R. Cannon, S. Cole, M. Colless, et al., Mon. Not. Roy. Astron. Soc. **335**, 432 (2002).
232. N. Y. Gnedin and A. J. S. Hamilton, Mon. Not. Roy. Astron. Soc. **334**, 107 (2002).
233. R. A. C. Croft, D. H. Weinberg, M. Bolte, S. Burles, L. Hernquist, N. Katz, D. Kirkman, and D. Tytler, Astrophys. J. **581**, 20 (2002).
234. V. Pettorino, C. Baccigalupi, and G. Mangano, JCAP **01**, 014 (2005).
235. P. Mukherjee, A. J. Banday, A. Riazuelo, K. M. Gorski, and B. Ratra, Astrophys. J. **598**, 767 (2003).
236. P. Brax, J. Martin, and A. Riazuelo, 6th Workshop on Non-Perturbative Quantum Chromodynamics pp. 315–325 (2002).
237. K. M. Gorski, B. Ratra, R. Stompor, N. Sugiyama, and A. J. Banday, Astrophys. J. Suppl. **114**, 1 (1998).
238. L. Samushia and B. Ratra, Astrophys. J. Lett. **680**, L1 (2008).
239. S. W. Allen, D. A. Rapetti, R. W. Schmidt, H. Ebeling, G. Morris, and A. C. Fabian, Mon. Not. Roy. Astron. Soc. **383**, 879 (2008).
240. J. R. Gott, III, M. S. Vogeley, S. Podariu, and B. Ratra, Astrophys. J. **549**, 1 (2001).
241. G. Chen, J. R. Gott, III, and B. Ratra, Publ. Astron. Soc. Pac. **115**, 1269 (2003).
242. B. Fields and S. Sarkar, J. Phys. G. **33**, 220 (2006).
243. Y. Chen, B. Ratra, M. Biesiada, S. Li, and Z.-H. Zhu, Astrophys. J. **829**, 61 (2016).
244. Planck Collaboration, R. Adam, P. A. R. Ade, N. Aghanim, M. I. R. Alves, M. Arnaud, M. Ashdown, J. Aumont, C. Baccigalupi, A. J. Banday, et al., Astron. Astrophys. **594**, A10 (2016).

245. M. Betoule, R. Kessler, J. Guy, J. Mosher, D. Hardin, R. Biswas, P. Astier, P. El-Hage, M. Konig, S. Kuhlmann, et al., Astron.Astrophys. **568**, A22 (2014).
246. C.-G. Park and B. Ratra, Astrophys. J. **868**, 83 (2018).
247. Planck Collaboration, N. Aghanim, Y. Akrami, M. Ashdown, J. Aumont, C. Baccigalupi, M. Ballardini, A. J. Banday, R. B. Barreiro, N. Bartolo, et al., Astron. Astrophys. **607**, A95 (2017).
248. A. Font-Ribera, P. McDonald, N. Mostek, B. A. Reid, H.-J. Seo, and A. Slosar, JCAP **1405**, 023 (2014).
249. J. Ooba, B. Ratra, and N. Sugiyama, Astrophys. Space Sci. **364**, 176 (2019).
250. D. Blas, J. Lesgourgues, and T. Tram, JCAP **2011**, 034 (2011).
251. B. Audren, J. Lesgourgues, K. Benabed, and S. Prunet, JCAP **2013**, 001 (2013).
252. C.-G. Park and B. Ratra, Astrophys. Space Sci. **364**, 134 (2019).
253. J. W. Henning, J. T. Sayre, C. L. Reichardt, P. A. R. Ade, A. J. Anderson, J. E. Austermann, J. A. Beall, A. N. Bender, B. A. Benson, L. E. Bleem, et al., Astrophys. J **852**, 97 (2018).
254. C.-G. Park and B. Ratra, Phys. Rev. D **101**, 083508 (2020).
255. A. Pavlov, L. Samushia, and B. Ratra, Astrophys. J. **760**, 19 (2012).
256. A. Orsi, C. Baugh, C. Lacey, A. Cimatti, Y. Wang, and G. Zamorani, Mon. Not. Roy. Astron. Soc. **405**, 1006 (2010).
257. J. E. Geach, A. Cimatti, W. Percival, Y. Wang, L. Guzzo, G. Zamorani, P. Rosati, L. Pozzetti, A. Orsi, C. M. Baugh, et al., Mon. Not. Roy. Astron. Soc. **402**, 1330 (2010).
258. W. J. Percival and B. M. Schaefer, Mon. Not. Roy. Astron. Soc. **385**, 78 (2008).
259. L. Guzzo, M. Pierleoni, B. Meneux, E. Branchini, O. Le Fèvre, C. Marinoni, B. Garilli, J. Blaizot, G. De Lucia, A. Pollo, et al., Nature **451**, 541 (2008).
260. C. Blake, T. Davis, G. B. Poole, D. Parkinson, S. Brough, M. Colless, C. Contreras, W. Couch, S. Croom, M. J. Drinkwater, et al., Mon. Not. Roy. Astron. Soc. **415**, 2892 (2011).
261. C. Blake, S. Brough, M. Colless, C. Contreras, W. Couch, S. Croom, T. Davis, M. J. Drinkwater, K. Forster, D. Gilbank, et al., Mon. Not. Roy. Astron. Soc **415**, 2876 (2011).
262. B. A. Reid, L. Samushia, M. White, W. J. Percival, M. Manera, N. Padmanabhan, A. J. Ross, A. G. Sánchez, S. Bailey, D. Bizyaev, et al., Mon. Not. Roy. Astron. Soc. **426**, 2719 (2012).
263. L. Anderson, E. Aubourg, S. Bailey, D. Bizyaev, M. Blanton, A. S. Bolton, J. Brinkmann, J. R. Brownstein, A. Burden, A. J. Cuesta, et al., Mon. Not. Roy. Astron. Soc. **427**, 3435 (2012).
264. A. Pavlov, O. Farooq, and B. Ratra, Phys. Rev. D **90**, 023006 (2014).
265. L. Samushia, W. J. Percival, and A. Raccanelli, Mon. Not. Roy. Astron. Soc. **420**, 2102 (2012).
266. O. Avsajanishvili, N. A. Arkhipova, L. Samushia, and T. Kahniashvili, Eur. Phys. J. **C74**, 3127 (2014).
267. G. Gupta, S. Sen, and A. A. Sen, JCAP **1204**, 028 (2012).
268. R. Giostri, M. Vargas dos Santos, I. Waga, R. R. R. Reis, M. O. Calvão, and B. L. Lago, JCAP **3**, 027 (2012).
269. O. Avsajanishvili, Y. Huang, L. Samushia, and T. Kahniashvili, Eur. Phys. J. **C78**, 773 (2018).
270. J. Sola Peracaula, A. Gomez-Valent, and J. de Cruz Pérez, Phys. Dark Univ. **25**, 100311 (2019).
271. H. Gil-Marín, W. J. Percival, L. Verde, J. R. Brownstein, C.-H. Chuang, F.-S. Kitaura, S. A. Rodríguez-Torres, and M. D. Olmstead, Mon. Not. Roy. Astron. Soc. **465**, 1757 (2017).
272. H. Gil-Marín, J. Guy, P. Zarrouk, E. Burtin, C.-H. Chuang, W. J. Percival, A. J. Ross, R. Ruggeri, R. Tojerio, G.-B. Zhao, et al., Mon. Not. Roy. Astron. Soc. **477**, 1604 (2018).
273. F. G. Mohammad, D. Bianchi, W. J. Percival, S. de la Torre, L. Guzzo, B. R. Granett, E. Branchini, M. Bolzonella, B. Garilli, M. Scodeggio, et al., Astron. Astrophys. **619**, A17 (2018).
274. H. Hildebrandt, M. Viola, C. Heymans, S. Joudaki, K. Kuijken, C. Blake, T. Erben, B. Joachimi, D. Klaes, L. Miller, et al., Mon. Not. Roy. Astron. Soc. **465**, 1454 (2017).
275. C.-G. Park and B. Ratra, Astrophys. Space Sci. **364**, 82 (2019).
276. L. Samushia and B. Ratra, Astrophys. J. **703**, 1904 (2009).
277. L. Samushia, A. Dev, D. Jain, and B. Ratra, Phys. Lett. B **693**, 509 (2010).
278. S. Capozziello, V. F. Cardone, M. Funaro, and S. Andreon, Phys. Rev. D **70**, 123501 (2004).
279. J. Ooba, B. Ratra, and N. Sugiyama, Astrophys. J. **866**, 68 (2018).
280. J. Ryan, S. Doshi, and B. Ratra, Mon. Not. Roy. Astron. Soc. **480**, 759 (2018).
281. A. Chudaykin, M. M. Ivanov, and M. Simonović, Phys. Rev. D **103**, 043525 (2021).
282. R. C. Nunes, S. K. Yadav, J. F. Jesus, and A. Bernui, Monthly Notices of the Royal Astronomical Society **497**, 2133 (2020).

283. E. de Carvalho, A. Bernui, F. Avila, C. P. Novaes, and J. P. Nogueira-Cavalcante, Astron. Astrophys. **649**, A20 (2021).
284. L. Samushia and B. Ratra, Astrophys. J. Lett. **650**, L5 (2006).
285. G. Chen and B. Ratra, Astrophys. J. Lett. **612**, L1 (2004).
286. K. M. Wilson, G. Chen, and B. Ratra, Mod. Phys. Lett. A **21**, 2197 (2006).
287. G. Chen and B. Ratra, Publ. Astron. Soc. Pac. **123**, 1127 (2011).
288. O. Farooq, D. Mania, and B. Ratra, Astrophys. J. **764**, 138 (2013).
289. O. Farooq and B. Ratra, Phys. Lett. B **723**, 1 (2013).
290. N. G. Busca, T. Delubac, J. Rich, S. Bailey, A. Font-Ribera, D. Kirkby, J. M. Le Goff, M. M. Pieri, A. Slosar, É. Aubourg, et al., Astronomy & Astrophysics **552**, A96 (2013).
291. O. Farooq and B. Ratra, Astrophys. J. Lett. **766**, L7 (2013).
292. Y. Chen, S. Kumar, and B. Ratra, Astrophys. J. **835**, 86 (2017).
293. C.-H. Chuang and Y. Wang, Mon. Not. Roy. Astron. Soc. **435**, 255 (2013).
294. S. Cao, M. Biesiada, J. Jackson, X. Zheng, Y. Zhao, and Z.-H. Zhu, JCAP **02**, 012 (2017).
295. S. Cao, X. Zheng, M. Biesiada, J. Qi, Y. Chen, and Z.-H. Zhu, Astron. Astrophys. **606**, A15 (2017).
296. S. Cao, J. Ryan, and B. Ratra, Mon. Not. Roy. Astron. Soc. **497**, 3191 (2020).
297. R. Chávez, R. Terlevich, E. Terlevich, F. Bresolin, J. Melnick, M. Plionis, and S. Basilakos, Mon. Not. Roy. Astron. Soc. **442**, 3565 (2014).
298. R. Chávez, M. Plionis, S. Basilakos, R. Terlevich, E. Terlevich, J. Melnick, F. Bresolin, and A. L. González-Morán, Mon. Not. Roy. Astron. Soc. **462**, 2431 (2016).
299. G. Risaliti and E. Lusso, Astrophys. J. **815**, 33 (2015).
300. G. Risaliti and E. Lusso, Nature Astron. **3**, 272 (2019).
301. S. Cao, J. Ryan, N. Khadka, and B. Ratra, Mon. Not. Roy. Astron. Soc. **501**, 1520 (2021).
302. J. S. Wang, F. Y. Wang, K. S. Cheng, and Z. G. Dai, Astron. Astrophys. **585**, A68 (2016).
303. F. F. Dirirsa, S. Razzaque, F. Piron, M. Arimoto, M. Axelsson, D. Kocevski, F. Longo, M. Ohno, and S. Zhu, Astrophys. J. **887**, 13 (2019).
304. A. L. González-Morán, R. Chávez, R. Terlevich, E. Terlevich, F. Bresolin, D. Fernández-Arenas, M. Plionis, S. Basilakos, J. Melnick, and E. Telles, Mon. Not. Roy. Astron. Soc. **487**, 4669 (2019).
305. E. Lusso, G. Risaliti, E. Nardini, G. Bargiacchi, M. Benetti, S. Bisogni, S. Capozziello, F. Civano, L. Eggleston, M. Elvis, et al., Astron. Astrophys. **642**, A150 (2020).
306. T. M. C. Abbott, S. Allam, P. Andersen, C. Angus, J. Asorey, A. Avelino, S. Avila, B. A. Bassett, K. Bechtol, G. M. Bernstein, et al., Astrophys. J. **872**, L30 (2019).
307. D. Brout, D. Scolnic, R. Kessler, C. B. D'Andrea, T. M. Davis, R. R. Gupta, S. R. Hinton, A. G. Kim, J. Lasker, C. Lidman, et al., Astrophys. J **874**, 150 (2019).
308. Y. Homayouni, J. R. Trump, C. J. Grier, K. Horne, Y. Shen, W. N. Brandt, K. S. Dawson, G. F. Alvarez, P. J. Green, P. B. Hall, et al., Astrophys. J **901**, 55 (2020).
309. Z. Yu, P. Martini, A. Penton, T. M. Davis, U. Malik, C. Lidman, B. E. Tucker, R. Sharp, C. S. Kochanek, B. M. Peterson, et al., Mon. Not. Roy. Astron. Soc. **507**, 3771 (2021).
310. M. L. Martínez-Aldama, B. Czerny, D. Kawka, V. Karas, S. Panda, M. Zajaček, and P. T. Życki, Astrophys. J **883**, 170 (2019).
311. N. Khadka, M. Zajaček, S. Panda, M. L. Martínez-Aldama, and B. Ratra, Mon. Not. Roy. Astron. Soc. **515**, 3729 (2022).
312. M. L. Martínez-Aldama, M. Zajaček, B. Czerny, and S. Panda, Astrophys. J **903**, 86 (2020).
313. M. Zajaček, B. Czerny, M. L. Martinez-Aldama, M. Rałowski, A. Olejak, R. Przyłuski, S. Panda, K. Hryniewicz, M. Śniegowska, M.-H. Naddaf, et al., Astrophys. J **912**, 10 (2021).
314. L. Samushia and B. Ratra, Astrophys. J. **714**, 1347 (2010).
315. M. Kowalski, D. Rubin, G. Aldering, R. J. Agostinho, A. Amadon, R. Amanullah, C. Balland, K. Barbary, G. Blanc, P. J. Challis, et al., Astrophys. J **686**, 749 (2008).
316. B. E. Schaefer, Astrophys. J. **660**, 16 (2007).
317. Y. Wang, Phys. Rev. D **78**, 123532 (2008).
318. N. Khadka and B. Ratra, Mon. Not. Roy. Astron. Soc. **499**, 391 (2020).
319. L. Amati, F. Frontera, M. Tavani, J. J. M. in't Zand, A. Antonelli, E. Costa, M. Feroci, C. Guidorzi, J. Heise, N. Masetti, et al., Astron. Astrophys. **390**, 81 (2002).

320. N. Khadka, O. Luongo, M. Muccino, and B. Ratra, JCAP **09**, 042 (2021).
321. E. E. Fenimore and E. Ramirez-Ruiz, arXiv:astro-ph/0004176 (2017).
322. J. P. Hu, F. Y. Wang, and Z. G. Dai, Mon. Not. Roy. Astron. Soc. **507**, 730 (2021).
323. F. Y. Wang, J. P. Hu, G. Q. Zhang, and Z. G. Dai, Astrophys. J. **924**, 97 (2022).
324. M. G. Dainotti, V. F. Cardone, and S. Capozziello, Mon. Not. Roy. Astron. Soc. **391**, 79 (2008).
325. M. G. Dainotti, R. Willingale, S. Capozziello, V. Fabrizio Cardone, and M. Ostrowski, Astrophys. J. **722**, L215 (2010).
326. M. G. Dainotti, V. F. Cardone, S. Capozziello, M. Ostrowski, and R. Willingale, Astrophys. J. **730**, 135 (2011).
327. M. G. Dainotti, A. Lenart, G. Sarracino, S. Nagataki, S. Capozziello, and N. Fraija, Astrophys. J. **904**, 97 (2020).
328. M. G. Dainotti, S. Nagataki, K. Maeda, S. Postnikov, and E. Pian, Astron. Astrophys. **600**, A98 (2017).
329. M. G. Dainotti, A. L. Lenart, N. Fraija, S. Nagataki, D. C. Warren, B. De Simone, G. Srinivasaragavan, and A. Mata, Publ. Astron. Soc. Jap. **73**, 970 (2021).
330. M. G. Dainotti, N. Omodei, G. P. Srinivasaragavan, G. Vianello, R. Willingale, P. O'Brien, S. Nagataki, V. Petrosian, Z. Nuygen, X. Hernandez, et al., Astrophys. J. Suppl. **255**, 13 (2021).
331. D. Mania and B. Ratra, Phys. Lett. B **715**, 9 (2012).
332. E. R. Siegel, R. Guzman, J. P. Gallego, M. Orduna Lopez, and P. Rodriguez Hidalgo, Mon. Not. Roy. Astron. Soc. **356**, 1117 (2005).
333. S. Cao, J. Ryan, and B. Ratra, Mon. Not. Roy. Astron. Soc. **509**, 4745 (2022).
334. A. L. González-Morán, R. Chávez, E. Terlevich, R. Terlevich, D. Fernández-Arenas, F. Bresolin, M. Plionis, J. Melnick, S. Basilakos, and E. Telles, Mon. Not. Roy. Astron. Soc. **505**, 1441 (2021).
335. A. G. Riess, S. Casertano, W. Yuan, J. B. Bowers, L. Macri, J. C. Zinn, and D. Scolnic, Astrophys. J. **908**, L6 (2021).
336. S. W. Allen, R. W. Schmidt, H. Ebeling, A. C. Fabian, and L. van Speybroeck, Mon. Not. Roy. Astron. Soc. **353**, 457 (2004).
337. I. Waga and J. A. Frieman, Phys. Rev. D **62**, 043521 (2000).
338. G. Chen and B. Ratra, Astrophys. J. **582**, 586 (2003).
339. S. Podariu, R. A. Daly, M. P. Mory, and B. Ratra, Astrophys. J. **584**, 577 (2003).
340. K.-H. Chae, G. Chen, B. Ratra, and D.-W. Lee, Astrophys. J. Lett. **607**, L71 (2004).
341. L. Campanelli, G. L. Fogli, T. Kahniashvili, A. Marrone, and B. Ratra, Eur. Phys. J. C **72**, 2218 (2012).
342. Y. Chen and B. Ratra, Astron. Astrophys. **543**, A104 (2012).
343. M. Bonamente, M. K. Joy, S. J. La Roque, J. E. Carlstrom, E. D. Reese, and K. S. Dawson, Astrophys. J. **647**, 25 (2006).
344. J. S. B. Wyithe and J. S. Bolton, Mon. Not. Roy. Astron. Soc. **412**, 1926 (2011).
345. G. D. Becker and J. S. Bolton, Mon. Not. Roy. Astron. Soc. **436**, 1023 (2013).
346. A. Songaila and L. L. Cowie, Astrophys. J. **721**, 1448 (2010).
347. J. X. Prochaska, J. M. O'Meara, and G. Worseck, Astrophys. J **718**, 392 (2010).
348. D. Maoz, J. N. Bahcall, D. P. Schneider, N. A. Bahcall, S. Djorgovski, R. Doxsey, A. Gould, S. Kirhakos, G. Meylan, and B. Yanny, Astrophys. J. **409**, 28 (1993).
349. E. E. Falco, in *31st Liege International Astrophysical Colloquium: Gravitational Lenses in the Universe* (1993).
350. D. Crampton, C. L. Morbey, O. Le Fevre, F. Hammer, L. Tresse, S. J. Lilly, and D. J. Schade, astro-ph/9410041 (1994).
351. C. S. Kochanek, E. E. Falco, and R. Schild, Astrophys. J. **452**, 109 (1995).
352. A. O. Jaunsen, M. Jablonski, B. R. Pettersen, and R. Stabell, Astron. Astrophys. **300**, 323 (1995).
353. A. G. Riess, W. H. Press, and R. P. Kirshner, Astrophys. J. **473**, 88 (1996).
354. P. M. Garnavich, S. Jha, P. Challis, A. Clocchiatti, A. Diercks, A. V. Filippenko, R. L. Gilliland, C. J. Hogan, R. P. Kirshner, B. Leibundgut, et al., Astrophys. J **509**, 74 (1998).
355. S. T. Myers, N. J. Jackson, I. W. A. Browne, A. G. de Bruyn, T. J. Pearson, A. C. S. Readhead, P. N. Wilkinson, A. D. Biggs, R. D. Blandford, C. D. Fassnacht, et al., Mon. Not. Roy. Astron. Soc. **341**, 1 (2003).
356. I. W. A. Browne, P. N. Wilkinson, N. J. F. Jackson, S. T. Myers, C. D. Fassnacht, L. V. E. Koopmans, D. R. Marlow, M. Norbury, D. Rusin, C. M. Sykes, et al., Mon. Not. Roy. Astron. Soc. **341**, 13 (2003).
357. L. I. Gurvits, K. I. Kellermann, and S. Frey, Astron. Astrophys. **342**, 378 (1999).
358. J. L. Atteia, B. Cordier, and J. Wei, International Journal of Modern Physics D **31**, 2230008 (2022).

 doi:10.20944/preprints202310.1818.v1

359. L. Amati, P. T. O'Brien, D. Götz, E. Bozzo, A. Santangelo, N. Tanvir, F. Frontera, S. Mereghetti, J. P. Osborne, A. Blain, et al., Experimental Astronomy **52**, 183 (2021).